Lightweight Cement-Based Materials and Structures

Lead Guest Editor: Kim Hung Mo
Guest Editors: Tung-Chai Ling and Moosa Mazloom

Lightweight Cement-Based Materials and Structures

Lightweight Cement-Based Materials and Structures

Lead Guest Editor: Kim Hung Mo
Guest Editors: Tung-Chai Ling and Moosa Mazloom

Chief Editor

Cumaraswamy Vipulanandan, USA

Zhaofei Chu (iD), China
Wonseok Chung (iD), Republic of Korea
Donato Ciampa (iD), Italy
Gian Paolo Cimellaro, Italy
Francesco Colangelo, Italy
Romulus Costache (iD), Romania
Liviu-Adrian Cotfas (iD), Romania
Antonio Maria D'Altri, Italy
Bruno Dal Lago (iD), Italy
Amos Darko (iD), Hong Kong
Arka Jyoti Das (iD), India
Dario De Domenico (iD), Italy
Gianmarco De Felice (iD), Italy
Stefano De Miranda (iD), Italy
Maria T. De Risi (iD), Italy
Tayfun Dede, Turkey
Sadik O. Degertekin (iD), Turkey
Camelia Delcea (iD), Romania
Cristoforo Demartino, China
Giuseppe Di Filippo (iD), Italy
Luigi Di Sarno, Italy
Fabio Di Trapani (iD), Italy
Aboelkasim Diab (iD), Egypt
Thi My Dung Do, Vietnam
Giulio Dondi (iD), Italy
Jiangfeng Dong (iD), China
Chao Dou (iD), China
Mario D'Aniello (iD), Italy
Jingtao Du (iD), China
Ahmed Elghazouli, United Kingdom
Francesco Fabbrocino (iD), Italy
Flora Faleschini (iD), Italy
Dingqiang Fan, Hong Kong
Xueping Fan, China
Qian Fang (iD), China
Salar Farahmand-Tabar (iD), Iran
Ilenia Farina, Italy
Roberto Fedele, Italy
Guang-Liang Feng (iD), China
Luigi Fenu (iD), Italy
Tiago Ferreira (iD), Portugal
Marco Filippo Ferrotto, Italy
Antonio Formisano (iD), Italy
Guoyang Fu, Australia
Stefano Galassi (iD), Italy

Junfeng Gao (iD), China
Meng Gao (iD), China
Giovanni Garcea (iD), Italy
Enrique García-Macías, Spain
Emilio García-Taengua (iD), United Kingdom
DongDong Ge (iD), USA
Khaled Ghaedi, Malaysia
Khaled Ghaedi (iD), Malaysia
Gian Felice Giaccu, Italy
Agathoklis Giaralis (iD), United Kingdom
Ravindran Gobinath, India
Rodrigo Gonçalves, Portugal
Peilin Gong (iD), China
Belén González-Fonteboa (iD), Spain
Salvatore Grasso (iD), Italy
Fan Gu, USA
Erhan Güneyisi (iD), Turkey
Esra Mete Güneyisi, Turkey
Pingye Guo (iD), China
Ankit Gupta (iD), India
Federico Gusella (iD), Italy
Kemal Hacıefendioğlu, Turkey
Jianyong Han (iD), China
Song Han (iD), China
Asad Hanif (iD), Macau
Hadi Hasanzadehshooiili (iD), Canada
Mostafa Fahmi Hassanein, Egypt
Amir Ahmad Hedayat (iD), Iran
Khandaker Hossain (iD), Canada
Zahid Hossain (iD), USA
Chao Hou, China
Biao Hu, China
Jiang Hu (iD), China
Xiaodong Hu, China
Lei Huang (iD), China
Cun Hui (iD), China
Bon-Gang Hwang, Singapore
Jijo James (iD), India
Abbas Fadhil Jasim (iD), Iraq
Ahad Javanmardi (iD), China
Krishnan Prabhakan Jaya, India
Dong-Sheng Jeng (iD), Australia
Han-Yong Jeon, Republic of Korea
Pengjiao Jia, China
Shaohua Jiang (iD), China

Chayut Ngamkhanong, Thailand
Trung Ngo, Australia
Tengfei Nian, China
Mehdi Nikoo, Canada
Youjun Ning, China
Olugbenga Timo Oladinrin, United Kingdom
Oladimeji Benedict Olalusi, South Africa
Timothy O. Olawumi, Hong Kong
Alejandro Orfila, Spain
Maurizio Orlando, Italy
Siti Aminah Osman, Malaysia
Walid Oueslati, Tunisia
SUVASH PAUL, Bangladesh
John-Paris Pantouvakis, Greece
Fabrizio Paolacci, Italy
Giuseppina Pappalardo, Italy
Fulvio Parisi, Italy
Dimitrios G. Pavlou, Norway
Daniele Pellegrini, Italy
Gatheeshgar Perampalam, United Kingdom
Daniele Perrone, Italy
Giuseppe Piccardo, Italy
Vagelis Plevris, Qatar
Andrea Pranno, Italy
Adolfo Preciado, Mexico
Chongchong Qi, China
Yu Qian, USA
Ying Qin, China
Giuseppe Quaranta, Italy
Krishanu ROY, New Zealand
Vlastimir Radonjanin, Serbia
Carlo Rainieri, Italy
Rahul V. Ralegaonkar, India
Raizal Saifulnaz Muhammad Rashid, Malaysia
Alessandro Rasulo, Italy
Chonghong Ren, China
Qing-Xin Ren, China
Dimitris Rizos, USA
Geoffrey W. Rodgers, New Zealand
Pier Paolo Rossi, Italy
Nicola Ruggieri, Italy
JUNLONG SHANG, Singapore

Nikhil Saboo, India
Anna Saetta, Italy
Juan Sagaseta, United Kingdom
Timo Saksala, Finland
Mostafa Salari, Canada
Ginevra Salerno, Italy
Evangelos J. Sapountzakis, Greece
Vassilis Sarhosis, United Kingdom
Navaratnarajah Sathiparan, Sri Lanka
Fabrizio Scozzese, Italy
Halil Sezen, USA
Payam Shafigh, Malaysia
M. Shahria Alam, Canada
Yi Shan, China
Hussein Sharaf, Iraq
Mostafa Sharifzadeh, Australia
Sanjay Kumar Shukla, Australia
Amir Si Larbi, France
Okan Sirin, Qatar
Piotr Smarzewski, Poland
Francesca Sollecito, Italy
Rui Song, China
Tian-Yi Song, Australia
Flavio Stochino, Italy
Mayank Sukhija, USA
Piti Sukontasukkul, Thailand
Jianping Sun, Singapore
Xiao Sun, China
T. Tafsirojjaman, Australia
Fujiao Tang, China
Patrick W.C. Tang, Australia
Zhi Cheng Tang, China
Weerachart Tangchirapat, Thailand
Xiaxin Tao, China
Piergiorgio Tataranni, Italy
Elisabete Teixeira, Portugal
Jorge Iván Tobón, Colombia
Jing-Zhong Tong, China
Francesco Trentadue, Italy
Antonello Troncone, Italy
Majbah Uddin, USA
Tariq Umar, United Kingdom
Muahmmad Usman, United Kingdom
Muhammad Usman, Pakistan
Mucteba Uysal, Turkey

Ilaria Venanzi, Italy
Castorina S. Vieira, Portugal
Valeria Vignali, Italy
Claudia Vitone, Italy
Liwei WEN, China
Chunfeng Wan, China
Hua-Ping Wan, China
Roman Wan-Wendner, Austria
Chaohui Wang, China
Hao Wang, USA
Shiming Wang, China
Wayne Yu Wang, United Kingdom
Wen-Da Wang, China
Xing Wang, China
Xiuling Wang, China
Zhenjun Wang, China
Xin-Jiang Wei, China
Tao Wen, China
Weiping Wen, China
Lei Weng, China
Chao Wu, United Kingdom
Jiangyu Wu, China
Wangjie Wu, China
Wenbing Wu, China
Zhixing Xiao, China
Gang Xu, China
Jian Xu, China
Panpan, China
Rongchao Xu, China
HE YONGLIANG, China
Michael Yam, Hong Kong
Hailu Yang, China
Xu-Xu Yang, China
Hui Yao, China
Xinyu Ye, China
Zhoujing Ye, China
Gürol Yildirim, Turkey
Dawei Yin, China
Doo-Yeol Yoo, Republic of Korea
Zhanping You, USA
Afshar A. Yousefi, Iran
Xinbao Yu, USA
Dongdong Yuan, China
Geun Y. Yun, Republic of Korea

Hyun-Do Yun, Republic of Korea
Cemal YİĞİT, Turkey
Paolo Zampieri, Italy
Giulio Zani, Italy
Mariano Angelo Zanini, Italy
Zhixiong Zeng, Hong Kong
Mustafa Zeybek, Turkey
Henglong Zhang, China
Jiupeng Zhang, China
Tingting Zhang, China
Zengping Zhang, China
Zetian Zhang, China
Zhigang Zhang, China
Zhipeng Zhao, Japan
Jun Zhao, China
Annan Zhou, Australia
Jia-wen Zhou, China
Hai-Tao Zhu, China
Peng Zhu, China
QuanJie Zhu, China
Wenjun Zhu, China
Marco Zucca, Italy
Haoran Zuo, Australia
Junqing Zuo, China
Robert Černý, Czech Republic
Süleyman İpek, Turkey

Contents

Research Article

A Comparative Study on the Thermal Conductivity of Concrete with Coal Bottom Ash under Different Drying Conditions

In-Hwan Yang [1], **Jihun Park,**[1] **Kyoung-Chul Kim,**[2] **and Sung-Won Yoo**[3]

[1]*Kunsan National University, Department of Civil Engineering, Daehak-Ro 558, Kunsan, Jeonbuk 54150, Republic of Korea*
[2]*Korea Institute of Civil Engineering and Building Technology, Structural Engineering Research Institute, Goyang, Gyeonggi 10223, Republic of Korea*
[3]*Gachon University, Department of Civil and Environmental Engineering, Seongnamdaero 1342, Seongnam, Gyeonggi 13120, Republic of Korea*

Correspondence should be addressed to In-Hwan Yang; ihyang@kunsan.ac.kr

The utilization of coal bottom ash (CBA) and fly ash in concrete has become more common. For CBA concrete, curing conditions would influence the thermal properties of the concrete due to the high water absorption capacity of the CBA aggregate. In addition, CBA and fly ash contents in concrete affect the thermal properties of the concrete. Therefore, the effects of the drying conditions and the CBA and fly ash contents on the thermal conductivity of CBA concrete were investigated in this study. The thermal conductivity of concrete was measured under two different curing and drying conditions: oven-dried conditions and saturated surface-dry (SSD) conditions, with curing times of 28 and 91 days. The concrete mixtures also contained different levels of CBA and fly ash. Crushed sand in the concrete mixtures was replaced by CBA with replacement ratios of 25%, 50%, 75%, and 100% by volume. In addition, cement in the concrete mixture was substituted by fly ash with replacement ratios of 20 and 40% by volume. The thermal conductivity of concrete under the oven-dried conditions was much lower than that under the SSD conditions. Moreover, the thermal conductivity of the concrete decreased as the CBA content increased under both the oven-dried and SSD conditions. The material properties of the concrete, including unit weight, compressive strength, and ultrasonic velocity, were also measured in the study. Compared with the SSD conditions, the compressive strength, unit weight, and ultrasonic velocity of CBA concrete were considerably lower under the oven-dried conditions. Moreover, the relationships between the thermal conductivity and unit weight, compressive strength, and ultrasonic velocity were suggested.

1. Introduction

Recently, global climate change has led to an increase in energy consumption for cooling in hot weather and for heating in cold weather. Applying lightweight concrete to construction materials for buildings is favorable because it reduces the use of energy in buildings and promotes efficient energy consumption [1–5]. The thermal properties of construction materials used for concrete buildings are strongly dependent on the porous aggregates and density of the material because a material with porous aggregates exhibits a low thermal conductivity [3].

Coal bottom ash (CBA) is considered to be favorable for the fabrication of concrete with low thermal conductivity because of its porous structure [6]. The thermal conductivity of mortar using CBA aggregates decreased by 64% when CBA was applied to the mortar mixture [7]. Ngohpok et al. [8] investigated the material properties of pervious concrete containing recycled and bottom ash aggregates. This study suggested that the use of CBA in pervious concrete significantly reduced the thermal conductivity of the concrete. Park et al. [9] also investigated the selected strength properties of CBA concrete under different curing and drying conditions. In addition, Gooi et al. [10] concluded that the

application of CBA concrete is a promising method for improving the energy efficiency of buildings.

Moreover, fly ash also influences the thermal conductivity of concrete. The heat flow resistance of fly ash is 15~40% greater than that of quartz sand [11]. However, the heat flow resistance of fly ash is affected by the moisture content, so it could decrease dramatically under higher moisture conditions. The effect of fly ash content on the thermal and mechanical properties of lightweight concrete was analyzed in the study by Zhou and Brooks [12]. Their test results revealed that lightweight concrete containing fly ash exhibited a low thermal conductivity but maintained its mechanical strength. Brooks et al. [4] compared the thermal and mechanical properties of concrete containing four different types of lightweight fillers, which included fly ash. According to their study, the thermal conductivity of concrete decreased as the fly ash content increased, and the density of the concrete containing fly ash was higher than that of the other concrete used in the study.

However, although CBA and fly ash affect the thermal conductivity of concrete, most studies exclusively evaluate the influence of only CBA or fly ash on the thermal conductivity of the resulting concrete. Studies on the effect of CBA and fly ash contents on the thermal conductivity of concrete in which they are used simultaneously are still limited. Ghosh et al. [13] investigated the thermal properties of mortar containing fly ash and CBA as a sand replacement. Additionally, there are very few studies investigating the effect of moisture contents or drying conditions on the thermal conductivity of lightweight concrete containing both CBA and fly ash. Khan [14] investigated the thermal conductivity of conventional concrete at various moisture contents and showed that the thermal conductivity of concrete was influenced by the moisture content. According to the study of Zhang et al. [15], the thermal conductivity of conventional concrete containing limestone and granite as coarse aggregates increased as the saturation degree in the concrete increased.

Moreover, the utilization of CBA and fly ash is expected to reduce the thermal conductivity of concrete. The thermal conductivity of concrete containing CBA and fly ash could be also affected by the drying conditions or moisture content inside the concrete because of the high water absorption capacity of CBA [3–5].

CBA concrete may be favorable to reduce the thermal conductivity in the walls of buildings but unfavorable to increase the strength of concrete structures due to lightweight of the concrete. The moisture content of concrete depends on curing and drying conditions. Eventually, curing and drying conditions influence the strength properties and thermal properties of the concrete. Therefore, the effect of curing and drying conditions on both the strength properties and thermal properties of CBA concrete is important. The study on the effect of curing and drying conditions on strength properties including the compressive strength, splitting tensile strength, and flexural tensile strength was performed in the earlier study [9]. However, the study on the effect of curing and drying conditions on the thermal conductivity of concrete containing CBA and fly ash is very

limited and accordingly the study on the effect of curing and drying conditions on thermal conductivity of concrete should be analyzed.

Therefore, this study aimed to highlight the effect of curing and drying conditions on the thermal conductivity of concrete containing CBA as the replacement of fine aggregate and fly ash as the replacement of cement, respectively. In particular, the thermal conductivity of concrete under saturated surface-dry (SSD) conditions and oven-dried conditions was investigated. Additionally, the material properties of the concrete used were analyzed at various CBA and fly ash contents.

2. Materials

The crushed natural coarse aggregate used in the mixture had a maximum size of 20 mm and a density of 2.60 g/cm^3. The sand used as fine aggregate had a maximum size of 5 mm and a density of 2.61 g/cm^3. The material properties of the coarse and fine aggregates, including density and water absorption, were measured as shown in Table 1. Figure 1 also provides the particle size distributions of the natural fine and coarse aggregates.

CBA was obtained from a thermal power plant and used as a fine aggregate substitution. CBA used in this study was collected from a commercial thermal power plant (Korea South-East Power Co., Ltd., Yeongheung Power Division, Yeongheung, Korea). The thermal power plant operates a rigorous waste treatment program, and thus, CBA was collected from this power plant. In addition, to secure the consistency of the CBA, it was chosen from the same batch of the production process. CBA is a by-product resulting from burning coal fuel at thermal power plants. Coal fuel supplied from different sources or burnt under different production process causes some variation in the properties of CBA. Therefore, to avoid such variations and secure the consistency of the CBA as much as possible, the supplier confirmed that the CBA used in this study had been supplied from the same source and produced in the same batch. Moreover, to examine the components of the CBA, some CBA samples were randomly selected and analyzed by using X-ray fluorescence spectrometry (XRF). The results of the analysis of the components for the CBA, as shown in Table 2, showed that the compositions of the samples were similar, which ensured the consistency of the CBA.

The properties of concrete containing CBA are dependent on those of the CBA. To secure the reproducibility of the results of tests performed to investigate the characteristics of CBA concrete, it is important to obtain CBA that is produced in the same batch and obtained from same source because test results can differ due to the different production processes used to make CBA.

Before CBA was mixed in the concrete mixture, it was ground until reaching a size distribution similar to that of the fine aggregate. To substitute the crushed fine aggregates in the mixture, CBA particles with sizes in the range between 0.15 and 5.0 mm were retained. Figure 2 provides the size distribution when the natural fine aggregate was replaced by CBA at various replacement ratios. It was assumed that the

TABLE 1: Physical properties of the used aggregates.

Aggregate	Water absorption (%)	Density (g/cm^3)
CBA	3.88	1.84
Coarse aggregate	1.02	2.60
Fine aggregate	0.64	2.61

(a)

(b)
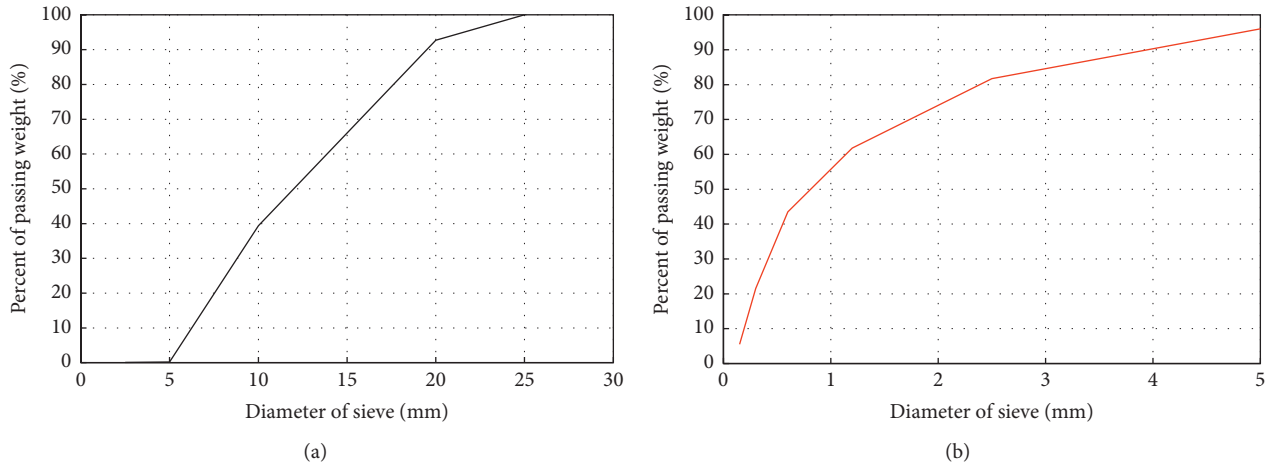
FIGURE 1: Sieve analysis of the coarse and fine aggregates. (a) Coarse aggregate. (b) Fine aggregate.

TABLE 2: Chemical composition of coal bottom ash, fly ash, and OPC.

Component	CBA (%)	Fly ash (%)	OPC (%)
Al_2O_3	26.20	22.10	4.59
CaO	3.93	6.42	65.00
SiO_2	55.70	55.80	17.60
Fe_2O_3	7.53	9.26	3.43
K_2O	1.17	1.30	1.13
Na_2O	0.76	1.33	0.19
MgO	1.09	1.69	3.53
SO_3	0.76	—	3.76

FIGURE 2: Sieve analysis of the combinations of CBA and fine aggregate at different replacement ratios.

variation in the size distribution when incorporating both fine aggregate and CBA would affect the density of the CBA concrete, which is related to the thermal conductivity of concrete. Table 1 shows the physical properties of CBA and natural coarse and fine aggregate. Compared to the fine aggregate, CBA had a lower density with a value of 1.84 g/cm^3, but its water absorption was 6 times greater than that of fine aggregate. The specific surface area of the CBA used in this study was not measured. Thus, CBA particles were dried under SSD conditions before being added to the mixture. Table 2 lists the chemical compositions of CBA and fine aggregate. The table shows that CBA contained a high silicon dioxide (SiO_2) content, exceeding 50% of the total components.

Ordinary Portland cement (OPC) has a specific gravity of 3.15 g/cm^3 and a specific surface area of 2,800 cm^2/g. OPC was combined with fly ash as the binder in the mixtures. The specific gravity and specific surface area of fly ash were 2.61 g/cm^3 and 3,650 cm^2/g, respectively. Table 2 shows that both CBA and fly ash contain large amounts of Al_2O_3 and SiO_2, improving the pozzolanic reaction in the concrete.

3. Experimental Program

3.1. Mixing Proportions. Two series of mixtures in terms of fly ash contents were fabricated, as shown in Table 3 in this study, which were applied in the earlier study [9]. For the first mixture series, OPC was substituted with fly ash at a volume ratio of 20%. Additionally, fine aggregate was substituted with CBA at volume ratios of 25%, 50%, 75%, and 100%. In addition, the influence of curing time was also considered. For the second mixture series, OPC was substituted with fly ash at a volume ratio of 40%. CBA was

Mixture	w/b	CBA content by volume (%)	Unit weight (kg/m^3)					
			Water	Binder		Fine aggregate		Coarse aggregate
				OPC	FA	Natural	CBA	
F4-B000	0.34	0	178.5	357.0	168.5	650.0	0.0	878.5
F4-B050	0.34	50	178.5	357.0	168.5	325.0	230.7	878.5
F4-B100	0.34	100	178.5	357.0	168.5	0.0	461.4	878.5
F2-B000	0.32	0	178.5	476.0	84.2	650.0	0.0	878.5
F2-B025	0.32	25	178.5	476.0	84.2	487.5	115.4	878.5
F2-B050	0.32	50	178.5	476.0	84.2	325.0	230.7	878.5
F2-B075	0.32	75	178.5	476.0	84.2	162.5	346.1	878.5
F2-B100	0.32	100	178.5	476.0	84.2	0.0	461.4	878.5

Notes: OPC: ordinary Portland cement; FA: fly ash; CBA: coal bottom ash; w/b: water-to-binder ratio.

also used to replace fine aggregate at two different ratios of 50% and 100% by volume in this mixing series. According to the ACI 211 committee [16], replacing cement with fly ash should be in the range of 10% to 35% to obtain the benefits from fly ash usage. The recommended maximum value from the ACI 211 corresponds approximately to the replacement ratio of 40%. Therefore, OPC was replaced with fly ash at a volume ratio of 40%. Additionally, compared to concrete with fly ash at a replacement ratio of 20%, concrete with fly ash with a replacement ratio of 40% could be differentiated more clearly due to its higher replacement ratio.

Water-to-binder ratios of 0.32 and 0.34 were applied in the first and second mixing series, respectively. In particular, due to the high water absorption of CBA, CBA and natural aggregates were dried under SSD conditions before being mixed. To improve the workability of the fresh concrete, an air-entraining admixture of 6.72 and 6.31 kg/m^3 and the HWRAs of 1.88 and 1.77 kg/m^3 were added to F2 and F4 series mixtures, respectively.

3.2. Curing and Drying of Concrete. According to the KS F 2405 standard [17], to evaluate the unit weight and compressive strength of CBA concrete, cylindrical concrete specimens with dimensions of 100 mm × 200 mm were cast. Two different curing and drying conditions were incorporated in this study.

For the water curing and SSD conditions, the cylindrical concrete specimens were demolded after 24 hours of pouring concrete into molds and then cured in a water storage at 23 ± 2°C until one day before testing [18]. Thereafter, the moisture on the surface of cylindrical concrete specimen was removed by towels, and finally, they were kept at room temperature in the laboratory before the measurement. In contrast, for the air curing and oven-dried conditions, the cylindrical concrete specimens were demolded after 24 hours of pouring concrete into molds and then cured in a water storage at 23 ± 2°C for 7 days. After that, they were cured at room temperature in the laboratory until one day before testing. Finally, the cylindrical concrete specimens were oven-dried in a chamber at 105 ± 5°C for 24 hours before the testing.

In brief, hereafter, the water curing and SSD conditions are designated the SSD conditions, and the air curing and oven-dried conditions are designated the oven-dried conditions.

3.3. Measurement of Thermal Properties. To measure the thermal conductivity of solid materials, there are several methods such as ASTM D 5334-05 [19], the two linear parallel (TLPP) method [20], and the transient plane source (TPS) method [21, 22]. Among these techniques, the TPS method has been widely used to measure the thermal conductivity of concrete. The measurement technique for the thermal conductivity used in this study was based on the TPS method. The thermal conductivity of CBA concrete specimens was measured using a TPS1500 testing device supplied by Hot Disk Ltd. (Gothenburg, Sweden), as shown in Figure 3. The hot disk sensor was inserted between two half-cylinders for measuring the thermal conductivity. The cut surfaces of the concrete specimen were polished to ensure an even surface before inserting the sensor. Electric voltage was introduced into the thermal sensor, and the sensor elements were heated when the TPS1500 device was operated. At this point, the sensor probed the thermal conductivity of the concrete specimens. This procedure was implemented three times for at least 90 minutes to ensure measurement accuracy, considering the thermal equilibrium of the concrete specimens. The measurement of the thermal conductivity of the CBA concrete was performed under the SSD and oven-dried conditions with curing ages of 28 and 91 days.

3.4. Measurement of Material Properties. The unit weight (bulk density) of the CBA concrete was evaluated under SSD and oven-dried conditions with curing ages of 28 and 91 days. A curing age of 28 days is typically used for the design of structural concrete. Additionally, the application of CBA and fly ash is expected to improve the strength properties of concrete prepared with long-term curing because of the pozzolanic properties of these two additives. Therefore, this study was focused on investigating the material properties of CBA concrete after curing for 28 and 91 days.

The dimensions and weights of three different cylindrical concrete specimens were measured. Then, the unit weight of CBA concrete was carefully measured three times and finally, the mean value of the unit weights of the CBA concrete was calculated. This measurement procedure implied that the possibility of human errors in the measurements was very low. Therefore, it was assumed that the test results were attributed to only the test variables.

Additionally, three cylindrical specimens of each series were tested by using a universal testing machine with a capacity of 2000 kN to evaluate the compressive strength of the CBA concrete in accordance with KS F 2405 [17]. The mean compressive strengths of the CBA concrete under SSD and oven-dried conditions were determined.

Finally, three cylindrical specimens were used to examine the ultrasonic velocity of the CBA concrete in accordance with ASTM C597-09 [23]. The instrument for measuring ultrasonic velocity included two transducers: a pulse generator and a receiver. It is recommended that an ultrasonic pulse with a frequency of 50~55 kHz is suitable for measuring the ultrasonic velocity of concrete [23–25]. Therefore, an instrument with a pulse frequency of 54 kHz was used in this study. The mean ultrasonic velocities of the CBA concrete under the SSD and oven-dried conditions were presented.

4. Test Results and Discussions

4.1. Thermal Conductivity of CBA Concrete. Figure 4(a) presents the thermal conductivity of CBA concrete with different fly ash contents (F2 and F4 series) and under different drying conditions at a curing age of 28 days. The S and D characteristics in the legend of the figure represent the SSD and oven-dried conditions, respectively.

The thermal conductivity of CBA concrete decreased when the drying condition was changed from SSD conditions to oven-dried conditions. Specifically, for the F2 series concrete specimens with CBA contents of 0%, 25%, 50%, 75%, and 100%, the thermal conductivities of the concrete under the oven-dried conditions decreased by 15.9%, 18.1%, 18.4%, 18.0%, and 19.0%, respectively, compared to the concrete under SSD conditions. Regarding the F4 series of concrete with CBA contents of 0%, 50%, and 100%, the thermal conductivities of the concrete under oven-dried conditions decreased by 17.2%, 20.6%, and 15.6%, respectively, compared to the concrete under SSD conditions. Finally, the test results implied that the thermal conductivity of the CBA concrete prepared under oven-dried conditions decreased significantly. Concrete with high thermal conductivity increases heat loss through walls in building structures. Therefore, the application of concrete with low thermal conductivity, such as the CBA concrete analyzed in this study, can reduce heat transfer, thus energy consumption in building structures.

The decrease in the thermal conductivity of CBA concrete prepared under oven-dried conditions was attributed to its low moisture content and hydration degree due to the different curing procedures of the concrete specimens. Concrete specimens cured under SSD conditions retained moisture because the specimens were kept for only one day at room temperature after they were taken out of the water tank, and then the moisture on the concrete surface was removed. Therefore, compared to concrete cured under oven-dried conditions, the thermal conductivity of concrete cured under SSD conditions is expected to be higher due to higher moisture content inside the porous concrete. SSD conditions are ideal because the concrete specimen is fully saturated with moisture at the measurement time. Oven-dried conditions are also ideal because concrete specimens are assumed to be dried completely at the measurement time. The SSD conditions and oven-dried conditions investigated in this study are two extreme conditions. The moisture content of actual concrete specimens depends on the environmental conditions and humidity to which they are subjected.

Water evaporation due to oven-drying methods increased the number of pores without moisture in the CBA concrete; thus, the thermal conductivity of the CBA concrete decreased under oven-dried conditions. Moreover, this tendency was similar to the results from some previous studies on conventional concrete [20, 26, 27]. Kim et al. [20] showed that the moisture content in concrete specimens was the main factor affecting the thermal conductivity of conventional concrete. Nguyen et al. [28] investigated the influence of moisture content on the thermal conductivity of concrete, including various types of lightweight aggregates. They found that the thermal conductivity of lightweight concrete increased almost linearly with the moisture content. Additionally, the specific surface area of the CBA can affect the thermal conductivity and strength properties of concrete because the specific surface area of the CBA affects the acceleration of the pozzolanic reaction [29].

The effect of CBA content on the thermal conductivity of CBA concrete is also shown in Figure 4(a). The thermal conductivity of the F2 series under SSD conditions decreased gradually as the CBA content increased. The thermal conductivity of the F2 series specimens under SSD conditions decreased gradually by 3.9%, 9.1%, 11.7%, and 15.0% as the natural fine aggregate was replaced with 25%, 50%, 75%, and 100% CBA, respectively. A decreasing tendency in the thermal conductivity of the F4 series under SSD conditions with the CBA content was also observed. The thermal conductivity of the F4 series decreased from 1.77 W/m•K to 1.46 W/m•K when the substitution of fine aggregate with CBA increased from 0% to 100%. In addition, the thermal conductivities of the F2 and F4 series under oven-dried conditions decreased gradually. The thermal conductivity of the F2 series decreased from 1.54 W/m•K to 1.27 W/m•K, while that of the F4 series decreased from 1.47 W/m•K to 1.23 W/m•K. Due to the pore structure of CBA, the concrete mixture containing CBA caused the porosity of the concrete to increase. Therefore, the thermal conductivity of CBA concrete decreased.

The influence of the fly ash content on the thermal conductivity of CBA concrete is shown in Figure 4(a). Strictly speaking, the thermal conductivity of the F4 series was lower than that of the F2 series, but the difference was not significant. Brooks et al. [4] investigated the effect of fly ash on the thermal properties of concrete under SSD conditions. Their test results provided that the thermal conductivity of the concrete significantly decreased as fly ash content in the mixture increased. Therefore, the comparison of the thermal conductivity results from this study and the previous study implied that the characteristics of fly ash, which depended on its source, could affect the thermal conductivity of CBA concrete containing fly ash.

(a)

(b)

(c)
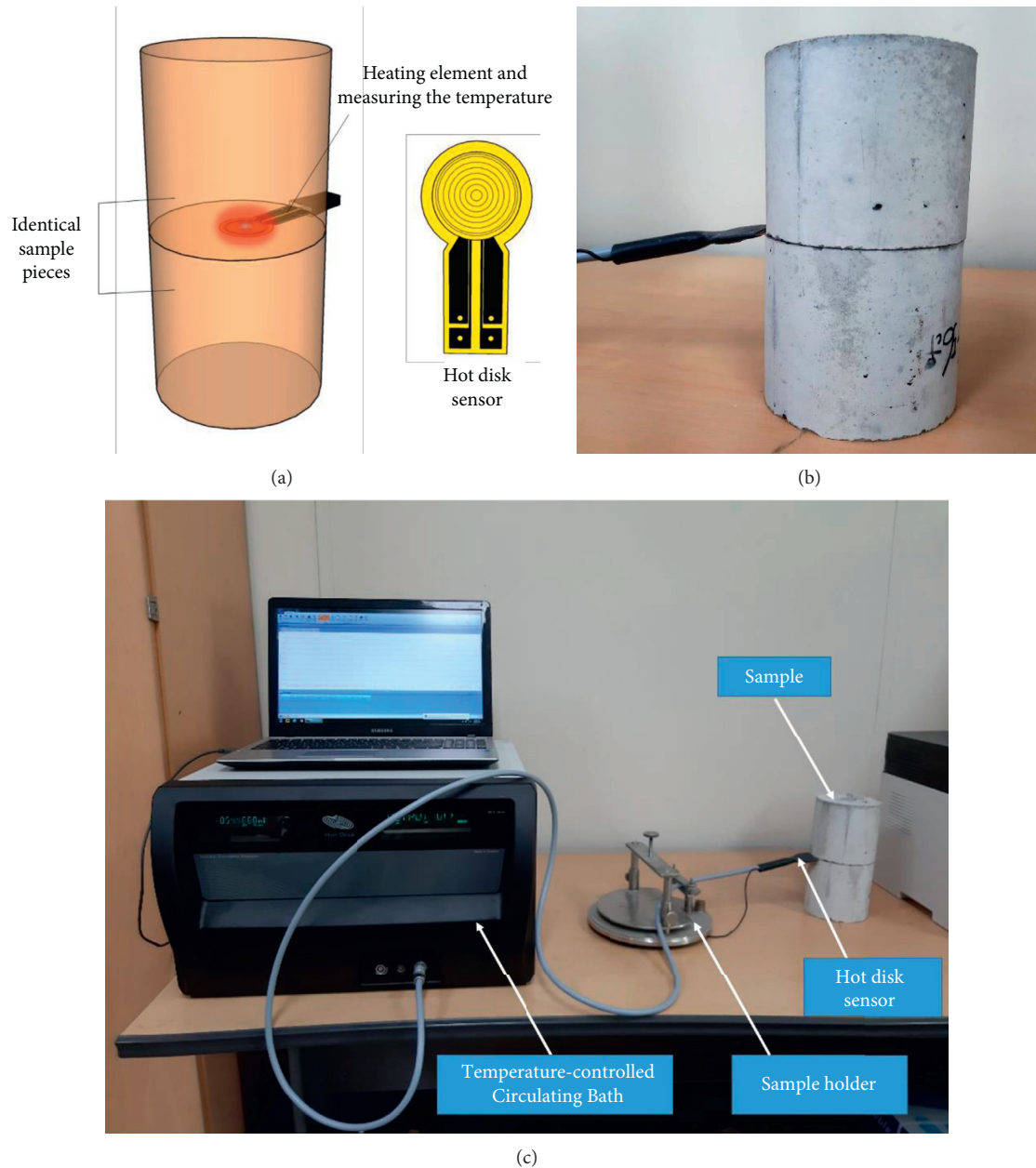
Figure 3: Instrument for measuring thermal conductivity. (a) Illustration of the TPS test. (b) Tested cylinder. (c) Test setup.

Figure 4(b) presents the effect of curing age on the thermal conductivity of the F2 series. The figure shows that the thermal conductivity of CBA concrete increased with curing age. Specifically, regarding CBA concrete under SSD conditions, the thermal conductivities of the F2-BA00, F2-BA025, F2-BA050, and F2-BA100 specimens increased by 5.8%, 5.4%, 7.8%, 5.1%, and 5.8%, respectively, when the curing age was extended from 28 to 91 days. Regarding CBA concrete under oven-dried conditions, the thermal conductivity of the concrete at 91 days was 8.0~14.4% greater than that of the concrete at 28 days.

4.2. Unit Weight of CBA Concrete. The unit weight of CBA concrete under different curing and drying conditions with a curing age of 28 days is shown in Figure 5(a). The unit weight

of CBA concrete decreased as the drying condition shifted from SSD conditions to oven-dried conditions. Regarding the F2 series specimens with various CBA contents, the unit weight under SSD conditions was 3.3~4.1% greater than that under oven-dried conditions. Regarding the F4 series with various CBA contents, the unit weight under SSD conditions was also 3.4~4.8% greater than that under oven-dried conditions. Therefore, the test results implied that the drying condition of the specimens had an effect on the unit weight of CBA concrete. This phenomenon might be caused by the water evaporation of specimens containing CBA due to oven-drying.

The influence of CBA content on the unit weight of CBA concrete is also found in Figure 5(a). The unit weights of CBA concrete decreased as the CBA content increased. The

Figure 4: Thermal conductivity of CBA concrete. (a) Comparison under different drying conditions. (b) Comparison at different curing ages.
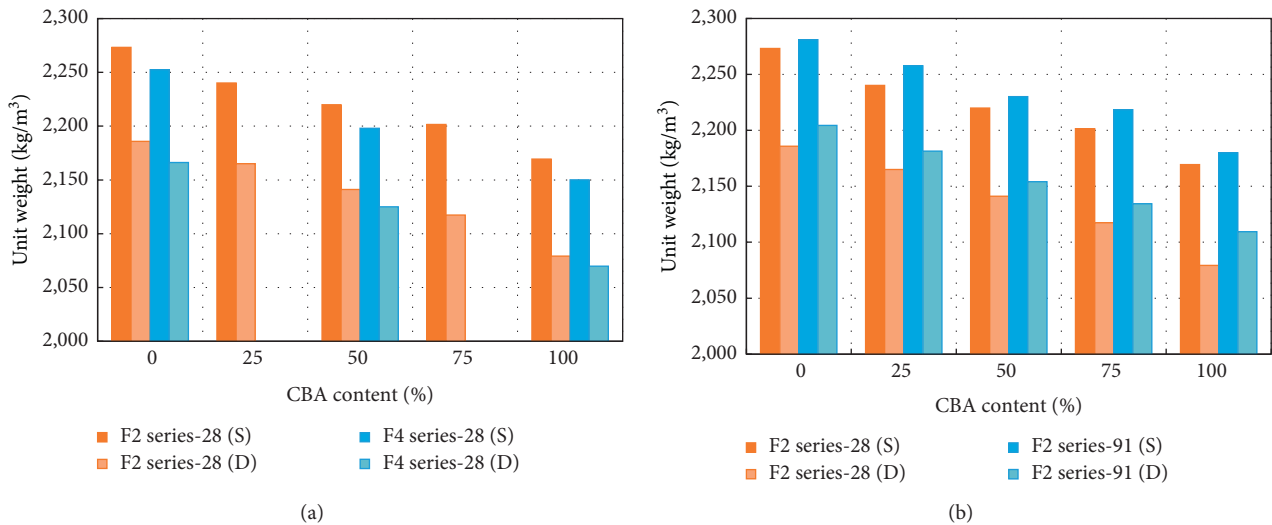
Figure 5: Unit weight of CBA concrete. (a) Comparison under different drying conditions. (b) Comparison at different curing ages.

unit weight of the F2 series concrete specimens under SSD conditions decreased from 2,273 kg/m³ to 2,169 kg/m³ as the CBA content increased from 0% to 100%. The unit weight of the F2 series concrete specimens under oven-dried conditions decreased from 2,185 kg/m³ to 2,079 kg/m³ as the CBA content increased from 0% to 100%, as similarly analyzed in the study of Park et al. [9]. A decrease in the unit weight was also observed in the F4 series specimens. The unit weight of the F4 series decreased by 4.4% under SSD conditions and by 4.5% under oven-dried conditions when the CBA content increased up to 100%. The decrease in the unit weight with the CBA content was due to the high porosity of CBA. A large decrease in unit weight due to CBA content under SSD conditions was reported in the study by Singh and Siddique [30]. In their study, the decrease in the unit weight reached approximately 10% as the CBA content increased from 20 to 100%, which was due to the low density of the CBA

aggregate. However, the addition of the fly ash to the concrete mixture might make the microstructure of the concrete denser; the decrease in unit weight in this study was lower than that in the previous study.

Moreover, the unit weights of the F2 and F4 series were compared to investigate the effect of fly ash content on unit weight. Overall, the unit weight of the F4 series was lower than that of the F2 series under both SSD and oven-dried conditions; however, this result was not significant. Specifically, under SSD conditions, the unit weights of the F4 series specimens containing 50% and 100% CBA were approximately 0.9% lower than those of the F2 series specimens containing 50% and 100% CBA. Under oven-dried conditions, the unit weights of the F4 series specimens containing 50% and 100% CBA were approximately 0.5~0.8% lower than those of the F2 series specimens containing 50% and 100% CBA.

The comparison of the unit weight of the F2 series specimens at the two different curing ages is presented in Figure 5(b). The unit weight of the F2 series specimens under the SSD and oven-dried conditions was improved as the curing age was increased; however, the improvement was not great.

4.3. Compressive Strength of CBA Concrete. The compressive strength of CBA concrete under oven-dried conditions was significantly lower than that of CBA concrete under SSD conditions, as shown in Figure 6(a). The compressive strength of the F2 and F4 series specimens decreased considerably under oven-dried conditions. The comparison of the compressive strengths of concrete with different CBA contents is also shown in Figure 6(a). The compressive strength of concrete decreased as the CBA content increased under both the oven-dried and SSD conditions. The compressive strength of the F2 series under SSD conditions decreased gradually by 4.1%, 5.9%, 7.0%, and 10.7% as the fine aggregate was replaced with 25%, 50%, 75%, and 100% CBA, respectively. In addition, the compressive strength of the F2 series under oven-dried conditions decreased from 56.3 MPa to 51.3 MPa when the CBA content increased from 0% to 100%. Moreover, a decrease in the compressive strength with increasing CBA content was also observed in the F4 series specimens. Specifically, the compressive strengths of the F4 series specimens under SSD conditions were 3.4~5.9% greater than those under oven-dried conditions.

The compressive strength of the concrete at a curing age of 28 days under SSD conditions in this study decreased by 4.2~15.1% as the CBA content increased. Meanwhile, the other study [31] showed that the compressive strength of CBA concrete at a curing age of 28 days under SSD conditions decreased by 18.2~27.3% as the fine aggregate was replaced with CBA aggregate of 25~100% by volume. Therefore, the decrease in compressive strength in this study was less than the decrease in the compressive strength in the previous study. This result could be due to the combined effect of the CBA and fly ash that made the concrete microstructure denser, as discussed by Majhi and Nayak [32], compared to when either CBA or fly ash was used in the concrete mixture.

A comparison of the compressive strengths of the F2 series concrete specimens with different curing ages is shown in Figure 6(b). The compressive strength of CBA concrete with a curing age of 91 days was greater than that with a curing age of 28 days. The improvement in compressive strength with the extended curing age was due to the pozzolanic reaction by the CBA and fly ash. The pozzolanic reaction of CBA and fly ash developed further with increasing curing time. The comparisons also showed that the effect of curing age on the compressive strength under oven-dried conditions was greater than the effect of curing age on the compressive strength under SSD conditions. This result implied that the development of the pozzolanic reaction with increasing curing age was affected by the curing conditions.

4.4. Ultrasonic Velocity of CBA Concrete. Figure 7(a) shows the comparison of the ultrasonic velocity of CBA concrete under the SSD and oven-dried conditions with a curing age of 28 days. Regarding the F2 series specimens, the ultrasonic velocity of the specimens under oven-dried conditions was 5.8~6.2% lower than that of the specimens under SSD conditions. Moreover, regarding the F4 series specimens, the ultrasonic velocity of the specimens under oven-dried conditions was 5.7~6.6% lower than that of the specimens under SSD conditions. Therefore, the test results showed that the ultrasonic velocity of CBA concrete was affected by the drying conditions.

The effect of CBA content on the ultrasonic velocity of CBA concrete under the two different drying conditions can be found in Figure 7(a). Regarding the F2 series specimens, the ultrasonic velocity under SSD conditions decreased by 0.9~3.3% and the ultrasonic velocity under oven-dried conditions decreased by 3.4% as the CBA content increased from 0 to 100%.

Figure 7(a) also shows the comparison of the ultrasonic velocity of CBA concrete with different fly ash contents. The specimens containing a high fly ash content showed a low ultrasonic velocity. As an example, the ultrasonic velocities of the F4-BA050 and F4-BA100 specimens were 0.8% and 1.1% lower than those of the F2-BA050 and F2-BA100 specimens, respectively, under SSD conditions. The ultrasonic velocities of the F4-BA050 and F4-BA100 specimens were 4,033 m/s and 3,965 m/s, while those of the F2-BA050 and F2-BA100 specimens were 4,066 m/s and 3,992 m/s, respectively, under oven-dried conditions. Therefore, the test results indicated that the fly ash content had a slight effect on the ultrasonic velocity of CBA concrete under both the SSD and oven-dried conditions.

Figure 7(b) shows that the ultrasonic velocity of the CBA concrete increased with increasing curing age under both the SSD and oven-dried conditions. Specifically, regarding the concrete specimens containing 25%, 50%, 75%, and 100% CBA under SSD conditions, the ultrasonic velocity increased by 2.6%, 2.7%, 3.3%, and 2.4%, respectively, as the curing age was extended from 28 to 91 days.

5. Relationships between the Thermal Conductivity and Material Properties

The relationship between the thermal conductivity and the unit weight of CBA concrete under both the SSD and oven-dried conditions is shown in Figure 8. The figure shows that the thermal conductivity of CBA concrete had a close relationship with the unit weight.

The replacement of natural aggregate with CBA increased the porosity of the concrete, and concrete with high porosity has a low thermal conductivity. Therefore, the thermal conductivity of CBA concrete decreased due to its high porosity.

Based on the regression analysis, the relation between the thermal conductivity and unit weight was expressed by the following equation:

(a)

(b)
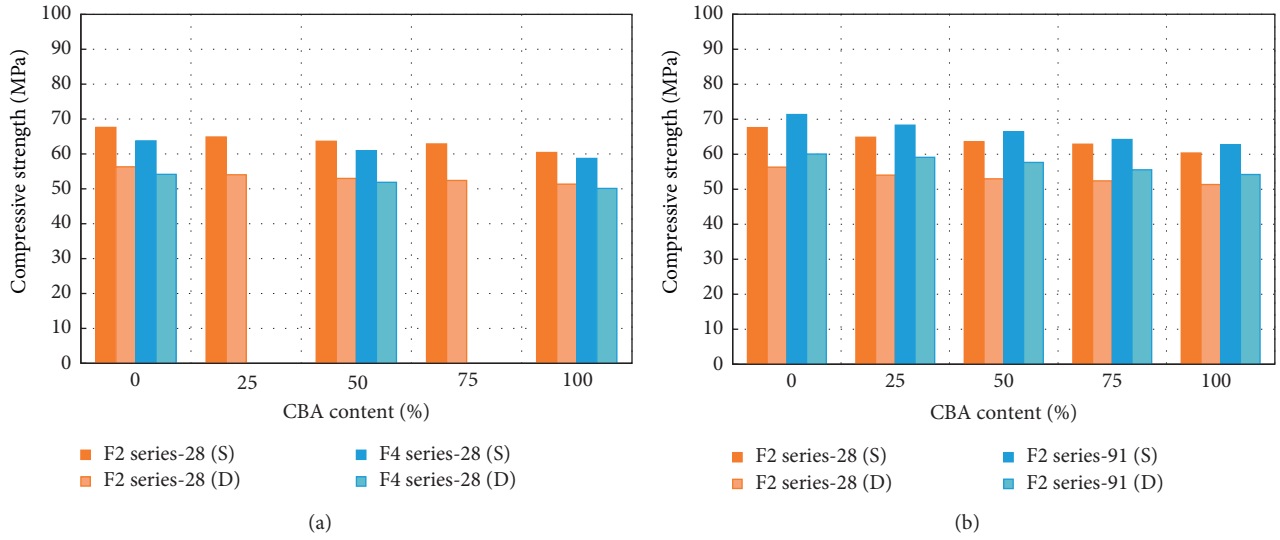
FIGURE 6: Compressive strength of CBA concrete. (a) Comparison under different drying conditions. (b) Comparison at different curing ages.
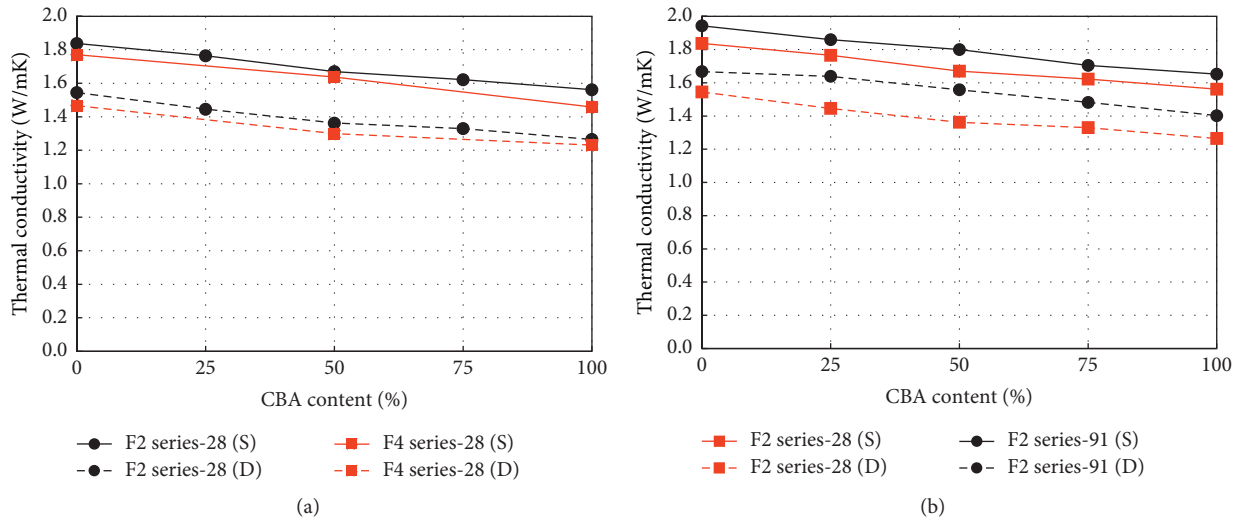

(a)

(b)
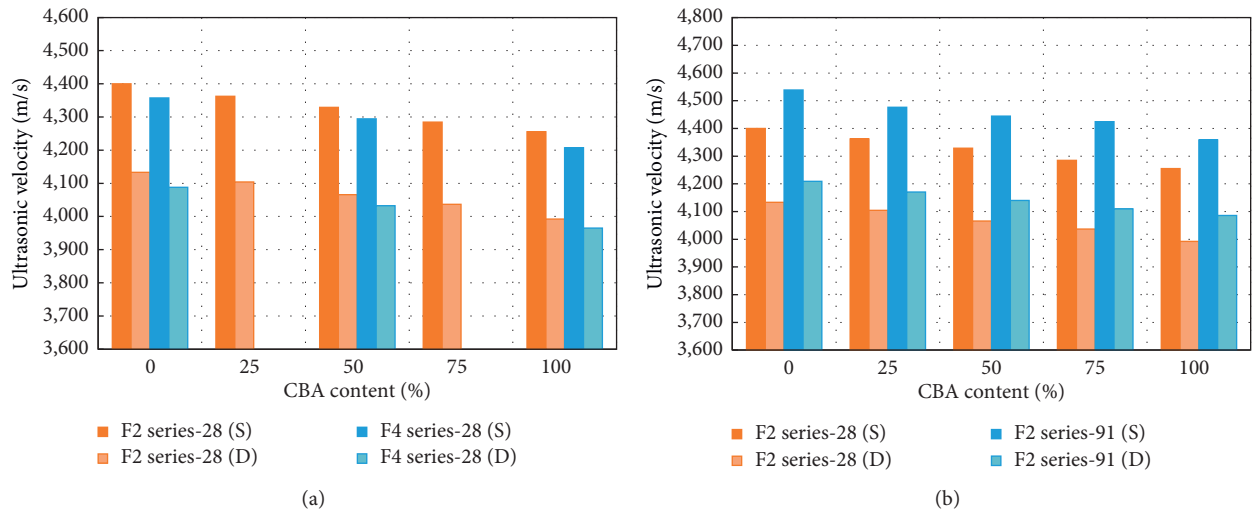
FIGURE 7: Ultrasonic velocity of CBA concrete. (a) Comparison under different drying conditions. (b) Comparison at different curing ages.

$$k = 0.0155e^{0.0021\nu},$$
$$R^2 = 0.9273,$$
(1)

where k is the thermal conductivity (W/mK) and ν is the unit weight (kg/m^3). The coefficient of determination (R^2) of this equation was close to 1, which implied that the equation could be used to precisely predict the thermal conductivity.

The relationship between the thermal conductivity and compressive strength of CBA concrete under both the SSD and oven-dried conditions is also shown in Figure 9. The thermal conductivity of CBA concrete increased linearly with the compressive strength. An exponential equation for predicting the thermal conductivity of CBA concrete by using the compressive strength is suggested as follows:

$$k = 0.4626e^{0.0205f_c},$$
$$R^2 = 0.9325,$$
(2)

where k is the thermal conductivity (W/m•K) and f_c is the compressive strength (MPa). This equation could be used to accurately predict the thermal conductivity because the coefficient of determination of this equation was close to 1.

Finally, the relationship between the thermal conductivity and ultrasonic velocity is shown in Figure 10. The relationship between the thermal conductivity and ultrasonic velocity of CBA concrete was close, as was the relationship between the thermal conductivity and unit weight and compressive strength of CBA concrete. The prediction for the thermal conductivity by measuring the ultrasonic velocity was suggested as follows:
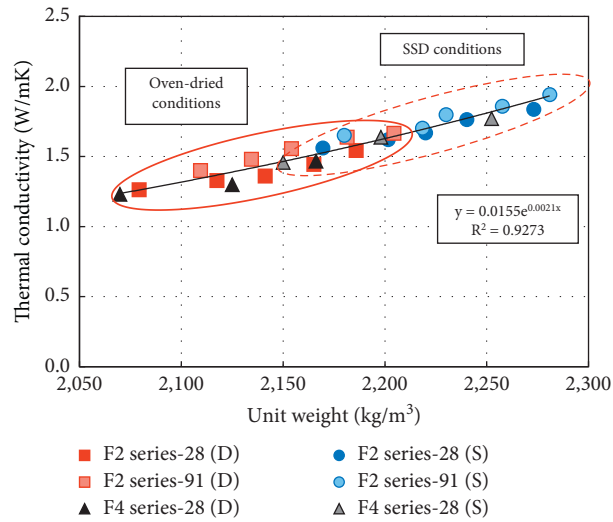
FIGURE 8: Relationship between the thermal conductivity and unit weight.
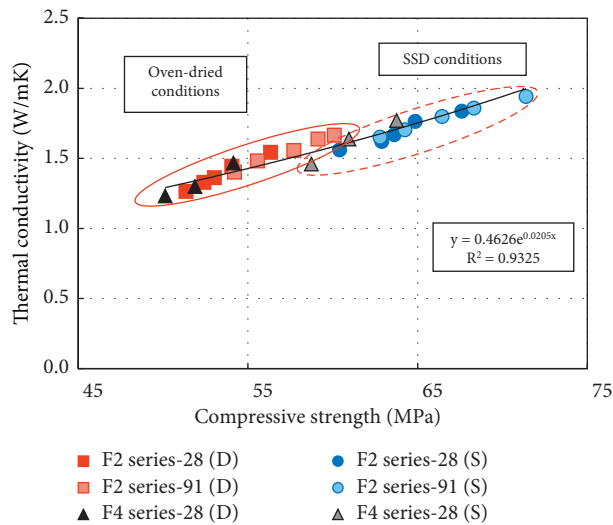
FIGURE 9: Relationship between the thermal conductivity and compressive strength.
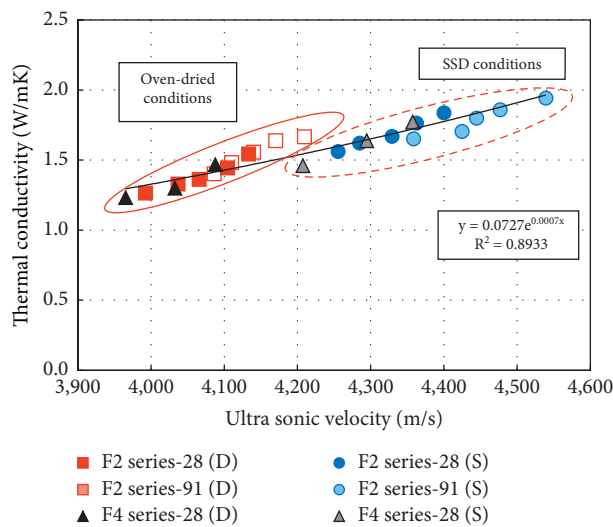
FIGURE 10: Relationship between the thermal conductivity and ultrasonic velocity.

$$k = 0.0727e^{0.0007V},$$
$$R^2 = 0.8933, \tag{3}$$

where k is the thermal conductivity (W/m•K) and V is the ultrasonic velocity (m/s). The proposed equation predicted the thermal conductivity well because the coefficient of determination R^2 of this equation was close to 1.

6. Conclusions

This research was carried out to evaluate the effects of the curing and drying conditions on the thermal conductivity and material properties of CBA concrete. In addition, the effects of the CBA and fly ash levels on the thermal conductivity of CBA concrete were investigated. Based on the extensive test results, the conclusions of this study can be drawn as follows:

(1) The test results revealed that curing and drying conditions had an effect on the unit weight of CBA concrete. Compared with that under SSD conditions, the unit weight of CBA concrete under the oven-dried conditions decreased by approximately 3~4%. This decrease in unit weight might be due to water evaporation from the CBA aggregate and hydration degree of concrete under different curing conditions.

(2) The drying conditions considerably affected the thermal conductivity of CBA concrete. The thermal conductivity of CBA concrete decreased significantly when the specimens had low moisture contents. The thermal conductivity of CBA concrete decreased by 15~20% under the oven-dried conditions. In addition, the thermal conductivity of CBA concrete also decreased significantly with increasing CBA content. Moreover, the influence of the fly ash content on the thermal conductivity of CBA concrete was not significant.

(3) The curing and drying conditions influenced the compressive strength of CBA concrete. The compressive strength of CBA concrete decreased by 14~16% under the oven-dried conditions. Additionally, the replacement of fine aggregate with CBA decreased the compressive strength of the resulting concrete.

(4) The ultrasonic velocity in CBA concrete was considerably affected by the drying conditions. Specifically, the ultrasonic velocity was approximately 6% lower when the drying conditions were changed from SSD conditions to oven-dried conditions. In addition, the ultrasonic velocity in CBA concrete decreased by approximately 3.3% when CBA level was increased.

(5) The relationships between the thermal conductivity and unit weight, compressive strength, and ultrasonic velocity were proposed, which included the test results under both the SSD and oven-dried conditions. These relationships could be applied to predict the thermal conductivity of CBA concrete by measuring the three material properties mentioned above.

Data Availability

The data used to support the findings in this study are available from the corresponding author upon request.

Conflicts of Interest

The authors declare that they have no conflicts of interest regarding the publication of this manuscript.

Acknowledgments

References

[1] F. Koksal, O. Gencel, and M. Kaya, "Combined effect of silica fume and expanded vermiculite on properties of lightweight mortars at ambient and elevated temperatures," *Construction and Building Materials*, vol. 88, pp. 175–187, 2015.

[2] C. Tasdemir, O. Sengul, and M. A. Tasdemir, "A comparative study on the thermal conductivities and mechanical properties of lightweight concretes," *Energy and Buildings*, vol. 151, pp. 469–475, 2017.

[3] I. Asadi, P. Shafigh, Z. F. B. Abu Hassan, and N. B. Mahyuddin, "Thermal conductivity of concrete-a review," *Journal of Building Engineering*, vol. 20, pp. 81–93, 2018.

[4] A. L. Brooks, H. Zhou, and D. Hanna, "Comparative study of the mechanical and thermal properties of lightweight cementitious composites," *Construction and Building Materials*, vol. 159, pp. 316–328, 2018.

[5] I. H. Yang and J. Park, "A study on the thermal properties of high-strength concrete containing CBA fine aggregates," *Materials*, vol. 13, no. 7, 2020.

[6] M. Singh, "1-coal bottom ash," in *Woodhead Publishing Series In Civil And Structural Engineering*, R. Siddique and P. B. T.-W. and S. C. M. in C. Cachim, Ed., Woodhead Publishing, Sawston, UK, pp. 3–50, 2018.

[7] E. Baite, A. Messan, K. Hannawi, F. Tsobnang, and W. Prince, "Physical and transfer properties of mortar containing coal bottom ash aggregates from Tefereyre (Niger)," *Construction and Building Materials*, vol. 125, pp. 919–926, 2016.

[8] C. Ngohpok, V. Sata, T. Satiennam, P. Klungboonkrong, and P. Chindaprasirt, "Mechanical properties, thermal conductivity, and sound absorption of pervious concrete containing recycled concrete and bottom ash aggregates," *KSCE Journal of Civil Engineering*, vol. 22, no. 4, pp. 1369–1376, 2018.

[9] J.-H. Park, Q.-T. Bui, S.-H. Jung, and I.-H. Yang, "Selected strength properties of coal bottom ash (CBA) concrete containing fly ash under different curing and drying conditions," *Materials*, vol. 14, no. 18, p. 5381, 2021.

[10] S. Gooi, A. A. Mousa, and D. Kong, "A critical review and gap analysis on the use of coal bottom ash as a substitute constituent in concrete," *Journal of Cleaner Production*, vol. 268, Article ID 121752, 2020.

[11] RILEM, *Fly Ash in Concrete: Properties and Performance*, RILEM, London, UK, 1991.

[12] H. Zhou and A. L. Brooks, "Thermal and mechanical properties of structural lightweight concrete containing lightweight aggregates and fly-ash cenospheres," *Construction and Building Materials*, vol. 198, pp. 512–526, 2019.

[13] A. Ghosh, A. Ghosh, and S. Neogi, "Reuse of fly ash and bottom ash in mortars with improved thermal conductivity performance for buildings," *Heliyon*, vol. 4, no. 11, Article ID e00934, 2018.

[14] M. I. Khan, "Factors affecting the thermal properties of concrete and applicability of its prediction models," *Building and Environment*, vol. 37, no. 6, pp. 607–614, 2002.

[15] W. Zhang, H. Min, X. Gu, Y. Xi, and Y. Xing, "Mesoscale model for thermal conductivity of concrete," *Construction and Building Materials*, vol. 98, pp. 8–16, 2015.

[16] American Concrete Institute, "Standard Practice for Selecting Proportions for Normal Heavyweight, and Mass Concrete (ACI 211.1-91) Reapproved 1997," Reported by ACI Committee 211, American Concrete Institute, Michigan, MI, USA, 1997.

[17] Korea Industrial Standard, *Standard Test Method for Compressive Strength of concrete; Ks F. 2405*, Korea Industrial Standards, Seoul, Republic of Korea, 2010.

[18] ASTM, *Standard Practice for Making and Curing Concrete Test Specimens in the Laboratory; ASTM C192/C192M–02*, ASTM, West Conshohocken, PA, USA, 2002.

[19] ASTM, *Standard Test Method for Determination of Thermal Conductivity of Soil and Soft Rock by Thermal Needle Probe Procedure; ASTM D5334–05*, ASTM, West Conshohocken, PA, USA, 2005.

[20] K.-H. Kim, S.-E. Jeon, J.-K. Kim, and S. Yang, "An experimental study on thermal conductivity of concrete," *Cement and Concrete Research*, vol. 33, no. 3, pp. 363–371, 2003.

[21] S. E. Gustafsson, "Transient plane source techniques for thermal conductivity and thermal diffusivity measurements of solid materials," *Review of Scientific Instruments*, vol. 62, no. 3, pp. 797–804, 1991.

[22] T. Log and S. E. Gustafsson, "Transient plane source (TPS) technique for measuring thermal transport properties of building materials," *Fire and Materials*, vol. 19, no. 1, pp. 43–49, 1995.

[23] ASTM, *Standard Test Method for Pulse Velocity through Concrete; ASTM C597-02*, ASTM, West Conshohocken, PA, USA, 2002.

[24] A. Ashrafian, M. J. Taheri Amiri, M. Rezaie-Balf, T. Ozbakkaloglu, and O. Lotfi-Omran, "Prediction of compressive strength and ultrasonic pulse velocity of fiber reinforced concrete incorporating nano silica using heuristic regression methods," *Construction and Building Materials*, vol. 190, pp. 479–494, 2018.

[25] A. S. Nikand and O. L. Omran, "Estimation of compressive strength of self-compacted concrete with fibers consisting nano-SiO2 using ultrasonic pulse velocity," *Construction and Building Materials*, vol. 44, pp. 654–662, 2013.

[26] Y. Liu, C. Ma, D. Wang, Y. Wang, and J. Liu, "Nonlinear effect of moisture content on effective thermal conductivity of building materials with different pore size distributions," *International Journal of Thermophysics*, vol. 37, no. 6, p. 56, 2016.

[27] D. J. Gawin, J. Kosny, and K. Wilkes, "Thermal conductivity of moist cellular concrete–experimental and numerical study," in *Proceedings of Performance of Exterior Envelopes of Whole Buildings IX, American Society of Heating, Refrigerating and Air-Conditioning Engineers–ASHRAE*, Tallahassee, FL, USA, December 2004.

[28] L. H. Nguyen, A.-L. Beaucour, S. Ortola, and A. Noumowé, "Experimental study on the thermal properties of lightweight aggregate concretes at different moisture contents and ambient temperatures," *Construction and Building Materials*, vol. 151, pp. 720–731, 2017.

[29] N. F. Basirun, M. H. W. Ibrahim, N. J. Jamaludin, and R. P. Jaya, "A review: the effect of grinded coal bottom ash on concrete," *In MATEC Web of Conferences ISCEE*, vol. 103, Article ID 01007, 2017.

[30] M. Singh and R. Siddique, "Effect of coal bottom ash as partial replacement of sand on workability and strength properties of concrete," *Journal of Cleaner Production*, vol. 112, pp. 620–630, 2016.

[31] M. Rafieizonooz, J. Mirza, M. R. Salim, M. W. Hussin, and E. Khankhaje, "Investigation of coal bottom ash and fly ash in concrete as replacement for sand and cement," *Construction and Building Materials*, vol. 116, pp. 15–24, 2016.

[32] R. K. Majhi and A. N. Nayak, "Properties of concrete incorporating coal fly ash and coal bottom ash," *Journal of the Institution of Engineers*, vol. 100, no. 3, pp. 459–469, 2019.

Research Article

Comparative Study of Lightweight Cementitious Composite Reinforced with Different Fibre Types and the Effect of Silane-Based Admixture

Geok Wen Leong [ID], **Hui Loo Chua, Kim Hung Mo** [ID], **Zainah Ibrahim, and Zhi Pin Loh**

Department of Civil Engineering, Faculty of Engineering, Universiti Malaya, Kuala Lumpur 50603, Malaysia

Correspondence should be addressed to Geok Wen Leong; geokwen@um.edu.my

This study aims to develop a type of fine-grained lightweight concrete, also known as lightweight cementitious composite (LCC), containing perlite microsphere (PM) and fibres with enhanced impermeability. The effect of polypropylene (PP), polyvinyl alcohol (PVA), and basalt fibres on the fresh and hardened properties of LCC was investigated. Besides, silane-based water repellent admixture was incorporated to reduce the water absorption and enhance the hydrophobicity of LCC. The dry densities of LCC developed were in the range of 912–985 kg/m^3. PP fibres have lesser influence on the strengths of LCC. However, PVA fibres enhanced the strength of LCC by up to 35.2% and 28% in the compressive strength and flexural strength, respectively, while the basalt fibres increased both strengths up to 30.1% and 43.5%, respectively. By considering the overall performance, LCC with 0.5% PVA fibres has achieved a good balance in workability and strength. Additionally, silane-based water repellent admixture had an excellent effect in reducing the water absorption and improving the hydrophobicity of LCC. By incorporating 1% of silane-based water repellent admixture, the LCC with 0.5% PVA fibres obtained water-resistant properties with the softening coefficient of 0.85 and water contact angle of 128.2°. In conclusion, a combination of PVA-LCC with 1% waterproofing admixture showed the best performance in terms of mechanical strength as well as hydrophobic properties and had the potential to be used in the fabrication of concrete façade.

1. Introduction

Concrete and cement-based materials are commonly used to fabricate façade panels because of their durability and versatility. With the use of lightweight concrete, the lifting efficiency of the panels can be improved, which shortens the installation process. According to BS EN 206, the oven-dry density of lightweight concrete is in the range of 800 kg/m^3 to 2000 kg/m^3. The low density of lightweight concrete can be achieved by incorporating lightweight aggregates. Conventional lightweight aggregates such as expanded perlite also possess low thermal conductivity, thus providing thermal insulation to the building [1]. However, the incorporation of expanded perlite reduces the compressive strength and increases the water absorption of concrete due to its porous nature [2]. Although façade panels are

nonstructural elements that are only subjected to self-weight and wind load, the increase in water absorption of lightweight concrete will increase the self-weight of the panels during the wet season. This drawback can be minimised by utilising microsized expanded perlite, namely, perlite microsphere (PM).

PM has a closed pore structure which allows it to achieve lower water absorption than conventional expanded perlite. The typical water absorption of expanded perlite is between 30 and 71% [1, 3, 4]. On the other hand, the water repellence of PM is 10% higher than the conventional expanded perlite [5]. In addition, the reduction in particle size of expanded perlite can increase the strength of PM [6, 7]. So, PM is less vulnerable to shearing force. Previously, the authors have developed a lightweight cementitious composite (LCC) using PM. LCC is a type of fine-grained lightweight

aggregate concrete with a high specific strength. The developed LCC achieved a 28-day compressive strength of 23.7 MPa with the dry density of 979 kg/m³ [8]. Considering the lower strength requirement for facade panel, the LCC mix could be altered to suit this application.

Lightweight cement-based material is usually more brittle than normal-weight concrete [2, 9]. The addition of fibres to the lightweight cementitious composite can be a promising solution to overcome the drawback of brittleness. The existence of fibres in cementitious composite delays and mitigates the propagation of microcracks and macrocracks [10]. Many researchers have manifested the effectiveness of using fibrous material to improve the hardened properties of the concrete [11–13]. The distribution, orientation, geometry, and volumetric proportion of fibres in the matrix are essential parameters in affecting the mechanical properties of composites. Therefore, it is crucial to determine the suitable type and optimal dosage of fibres for LCC made of PM while maintaining the low density of LCC.

Furthermore, enhancing the hydrophobic properties of LCC can be an added value since one of the main challenges encountered in façade wall application is surface staining due to weathering [14]. Hydrophobic properties can be achieved by using a hydrophobic agent during the mixing stage [15, 16] or water repellent coating [17]. However, the surface coating method can become more vulnerable under UV radiation [18]. Therefore, from the practical point of view, mixing the hydrophobic agent directly in LCC is preferable because if the surface of LCC is destroyed, the newly exposed part of the LCC can still exhibit hydrophobicity. Therefore, in this research, a silane-based water repellent admixture was added in LCC during mixing.

In short, this study aims to develop LCC containing PM and fibres with enhanced impermeability. The effect of polypropylene (PP), polyvinyl alcohol (PVA), and basalt fibres on the workability and mechanical strength of LCC was evaluated. Besides that, silane-based water repellent admixture was incorporated to reduce the water absorption and enhance the hydrophobicity of LCC. This study would be useful for the application of LCC as a façade panel.

2. Materials and Methods

2.1. Materials. CEM I Ordinary Portland Cement (OPC) of class 42.5 N was used in this study. Silica fume (SF) and fly ash (FA), fulfilling EN 13263-1 and EN 450-1, were used as supplementary cementing materials to improve the properties of the composites. PM with a bulk density of 700 kg/m³ and an average particle size of 200 μm was used as lightweight aggregate to produce LCC (Figure 1). PP, PVA, and basalt fibres used in this study are shown in Figure 2. The properties of fibres provided by manufacturer are presented in Table 1. To produce LCC with adequate consistency and improved cohesiveness of the mixture, polycarboxylate ether-based superplasticiser (SP) and styrene butadiene rubber (SBR) were used in all mixes. Additionally, silane-based water repellent admixture was incorporated in the selected mix, and the hydrophobic properties of LCC were investigated.

2.2. Mix Proportioning and Sample Preparation. Ten mixtures with a varying volume of PP, PVA, and basalt fibres were prepared. Besides the control mix (PM-0), the LCCs were categorised into 3 groups (LCC-PP, LCC-PVA, and LCC-basalt) based on the respective fibre type. The volume fraction of each type of fibre varied between 0%, 0.125%, 0.25%, and 0.50%. Additionally, two mixes of LCC with 0.50% PVA fibres were added with 1% and 2% of silane-based admixture. The mixture proportion of LCCs is tabulated in Table 2. All other parameters such as binder content (600 kg/m³) and the water/binder ratio, dosage of SP, and SBR were kept constant in all mixtures.

The mixing process of LCC started with dry mixing of binders and PM for one minute. It was then followed by adding water and chemical admixtures while continuing mixing for another two minutes. Next, the fibres were gradually dispersed in the mix, and the mixing process continued until a homogeneous mixture was obtained. A portion of the fresh LCC was used to conduct the flow table test, while the rest was cast into prelubricated moulds. After compaction, the specimens were covered by plastic sheets to avoid loss of moisture. From each batch, six 50 mm cubes (for compressive strength) and three prisms with a dimension of 40 mm × 40 mm × 160 mm (for flexural strength test) were cast. For LCC with silane-based admixture, additional 50 mm cubes (water absorption test and water saturated compressive strength test) and LCC tiles with a dimension of 70 mm × 75 mm × 16 mm (contact angle test) were prepared. All the specimens were demoulded 24 hours after casting, and the hardened LCC specimens were air-cured in laboratory condition until the age of testing.

2.3. Test Methods. The flow table test was carried out following ASTM C1437. The compressive strength test was carried out at the age of 7 days and 28 days and in accordance with ASTM C109. The flexural strength test was conducted via 3-point bending. The machine used in the bending test is INSTRON displacement-controlled testing machine with a load capacity of 100 kN. Besides that, the water absorption of specimens with silane-based water repellent admixture after immersion for 30 mins and 48 hours was determined. The contact angle test was carried out to determine the surface hydrophobicity of LCC which was incorporated with silane-based admixture. The contact angle was measured using an optical contact angle measuring system, OCA 15EC, with Spinocerebellar Ataxia Type 20 (SCA20) software (Figure 3) after placing a distilled water droplet on the specimen surface.

3. Results and Discussion

3.1. Workability. Figure 4 shows the workability of fresh LCC with varying types and dosages of fibres. Based on the results, an increase in fibre dosage decreased the workability of LCC regardless the type of fibre. Similar findings were reported by Jiang et al. [19] and Loh et al. [20]. With the inclusion of 0.50% of PP, PVA, and basalt fibre, the workability of the control mix decreased by 24.6%, 32.5%, and 56.9%, respectively. Under the condition of fixed binder content and dosage of chemical admixture, the surface area

(a)

(b)
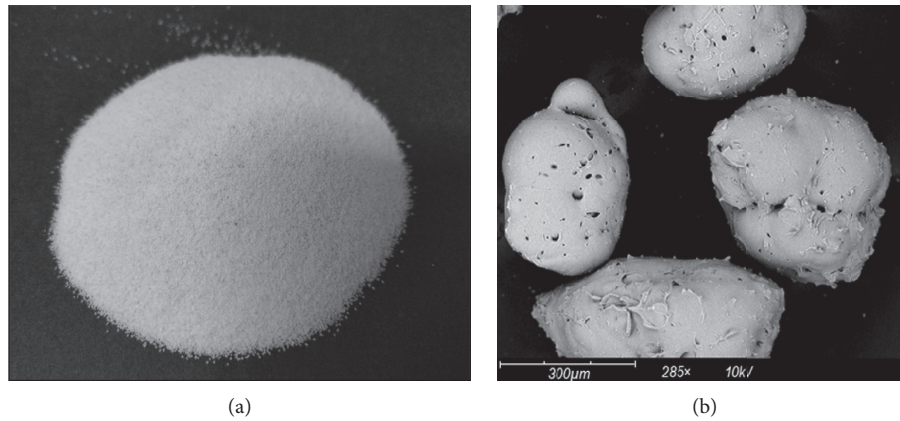
FIGURE 1: (a) Physical appearance of PM; (b) SEM image of PM.

(a)

(b)

(c)
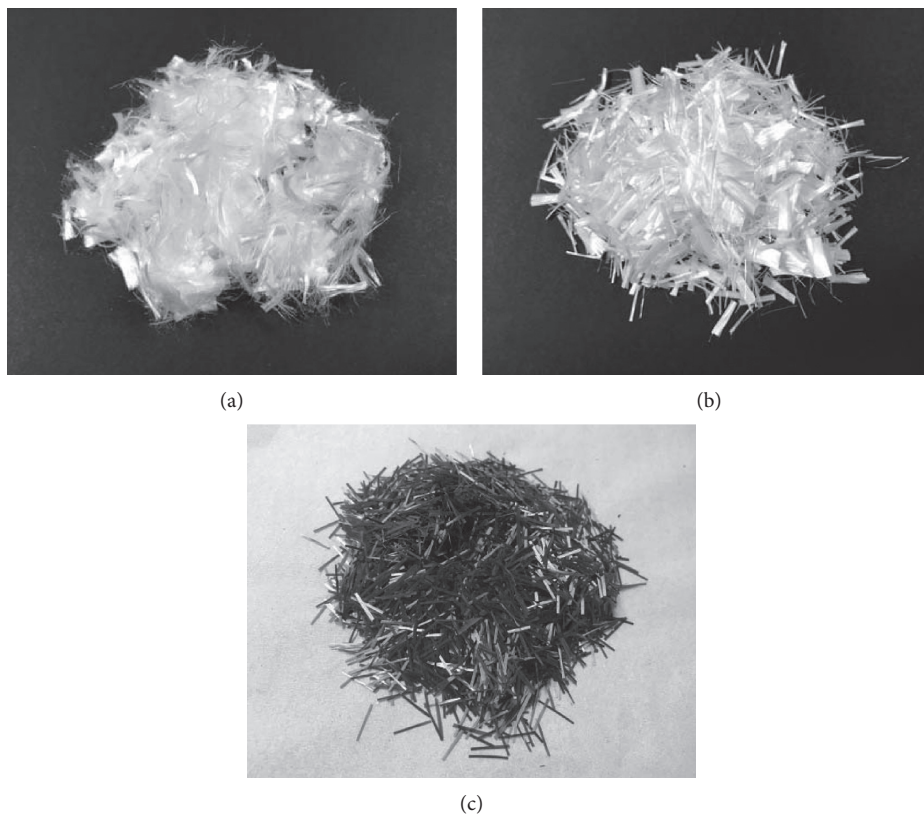
FIGURE 2: (a) PP fibres; (b) PVA fibres; (c) basalt fibres.

and stiffness of fibres are the factors affecting the workability of fibre-reinforced mortar. Since basalt fibre has the highest aspect ratio and modulus of elasticity among the fibres used, this led to the greatest reduction in workability of the LCC.

3.2. Density. The density of LCC developed in this study was in the range of 912 to 985 kg/m^3. The effect of fibres on LCC density was less significant in this study due to the low incorporation level of fibres, which was less than 1%. The highest percentage difference was observed with 0.50% PVA fibres, where the density of the control mix increased by 8%. A similar trend was observed in both LCC-PP and LCC-

PVA. The density increased with a higher dosage of fibres. However, in the case of basalt fibres, the density of LCC with 0.50% basalt fibres (PM + 0.50 B) was lower than that of LCC with 0.25% basalt fibres (PM + 0.25B). In fact, this correlates with the low workability of PM + 0.50 B, which resulted in poor compaction and low density.

3.3. Compressive Strength

3.3.1. Effects of Fibres on Compressive Strength. The compressive strength of LCCs is tabulated in Table 3. Early strength development of LCC was observed by

TABLE 1: Properties of fibres.

Properties	Types of fibre		
	PP	PVA	Basalt
Length (mm)	12	12	12
Diameter (μm)	50	40	12
Density (g/cm^3)	0.90	1.29	2.67
Tensile strength (MPa)	350–500	1600	4150–4800
Modulus of elasticity (GPa)	3.5–3.9	41	100–110
Aspect ratio (length/diameter)	240	300	1083

TABLE 2: Mixture proportions of LCC (by weight of binder).

Mix ID	Binder			Water/binder ratio	PM	*Fibre (%)			**Chemical admixture (%)		
	OPC	FA	SF			PP	PVA	Basalt	SBR	SP	Water repellent
PM-0 (control mix)						—	—	—			—
PM + 0.125PP						0.125	—	—			—
PM + 0.25PP						0.250	—	—			—
PM + 0.50PP						0.500	—	—			—
PM + 0.125PVA						—	0.125	—			—
PM + 0.25PVA	0.78	0.17	0.05	0.35	0.42	—	0.250	—	10.0	1.2	—
PM + 0.50PVA						—	0.500	—			—
PM + 0.125B						—	—	0.125			—
PM + 0.25B						—	—	0.250			—
PM + 0.50B						—	—	0.500			—
W1PM + 0.50PVA						—	0.500	—			1.0
W2PM + 0.50PVA						—	0.500	—			2.0

Notes: *means by volume of aggregate; **means by weight of binder.
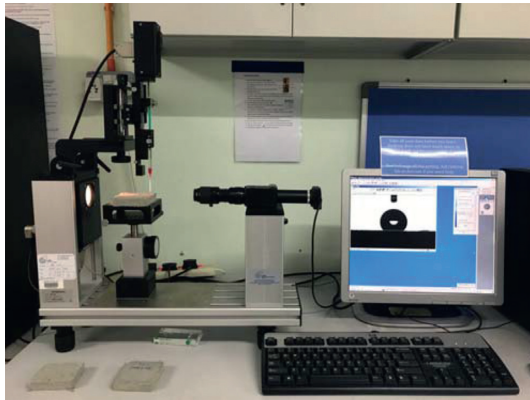
FIGURE 3: OCA 15EC with software SCA 20 module.
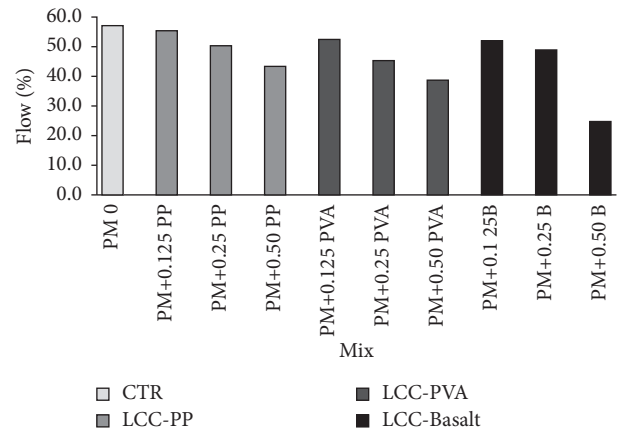
FIGURE 4: Flow value of LCC.

attaining 75.2% to 98.8% of its 28-day compressive strength at 7 days. This could be attributed to the use of SF [20] and SBR [21], which increased the cohesiveness of the matrix. Besides that, the inclusion of 0.125–0.25% of PP fibres and 0.125% of basalt fibres had a negligible effect on the compressive strength of LCC at the early age of 7 days. Nevertheless, the maximum compressive strength of these mixes at 28 days was 15.9% higher than that of the control mix. This finding is in line with results reported by Wu et al. [22], where the bonding strength between matrix and fibres increased with the curing age of concrete. Moreover, the ultimate compressive strength of LCC increased by adding fibres with high modulus of elasticity . At the same fibre dosage of 0.25%, LCC-basalt achieved the highest

compressive strength, 15.9 MPa, followed by LCC-PVA, 13.9 MPa, and LCC-PP, 13.5 MPa.

Furthermore, the failure mechanism of LCC was improved with the use of fibres. Figure 5 shows the typical failure of LCC specimens after the compression test. For the LCC with fibres, no obvious spalling was observed. This observation indicates the effectiveness of fibres in constraining lateral deformation and reducing the brittleness of the LCC. Both LCC-PP and LCC-PVA achieved the highest compressive strength among their groups with 0.50% fibre volume. On the other hand, the addition of basalt fibres increased the compressive strength of LCC until a fibre dosage of 0.25%. The compressive strength of PM + 0.50B

TABLE 3: Density and compressive strength of LCC.

Mix ID	Density (kg/m³)	Compressive strength (MPa)	
		7 days	28 days
PM-0 (control mix)	912	12.0	12.2
PM + 0.125PP	923	10.9	13.1
PM + 0.25PP	935	10.0	13.5
PM + 0.50PP	959	13.9	14.2
PM + 0.125PVA	931	13.5	14.3
PM + 0.25PVA	939	13.3	13.9
PM + 0.50PVA	985	15.3	16.5
PM + 0.125B	940	10.8	14.1
PM + 0.25B	957	14.0	15.9
PM + 0.50B	932	11.6	14.4

(a)

(b)
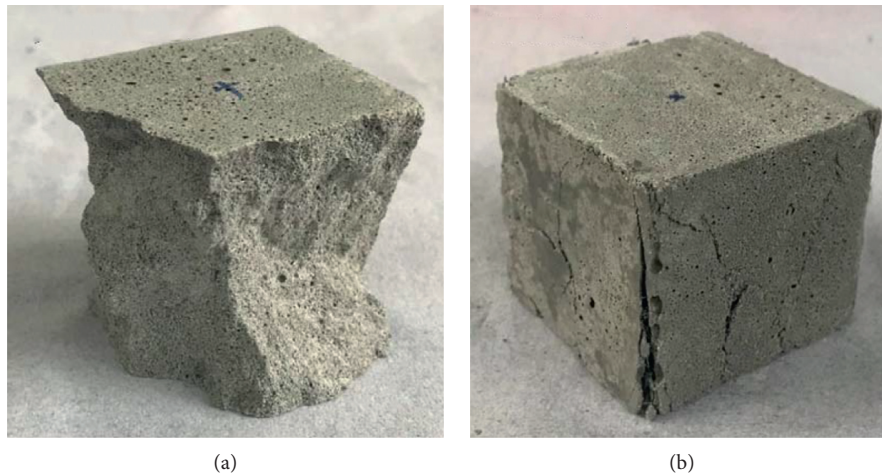
FIGURE 5: Failure pattern of LCC (a) without fibre; (b) with fibres.

was about 9.4% lower than PM + 0.25B. This could be related to the increased formation of pores and voids within the composite due to the poor workability of PM + 0.25B [23]. However, the composite containing 0.50% basalt fibres still had higher strength than the composite without fibres. Thus, for PM-0, the optimum incorporation level of each fibre type was 0.50% for both PP and PVA fibres, while it was 0.25% for basalt fibres. Beyond the optimum levels, a higher SP dosage is required to achieve adequate workability.

Among all the LCC developed, PM + 0.50PVA achieved the highest compressive strength of 16.9 MPa, and this mix also fulfilled the minimum compressive strength of structural lightweight concrete recommended by CEB/RILEM [24], which is more than 15 MPa. Moreover, based on the research done by Hanif et al. [25] and Blanco et al. [26], the 28-day compressive strength of LCC produced using fly ash cenospheres was between 5 and 18 MPa with a dry density of 885–1138 kg/m³. Therefore, PM + 0.50PVA was selected for further investigation on the effect of silane-based admixture since the 28-day compressive strength was within the reported range.

3.3.2. Effects of Silane-Based Admixture on Compressive Strength. The compressive strength and softening coefficient of PM + 0.50PVA mix with and without silane-based water repellent admixture are tabulated in Table 4. The use of 1% and 2% water repellent admixture reduced the compressive strength of LCC by 34.0% and 26.4%, respectively. This result is in line with the findings reported by Li et al. [27] and Tittarelli and Moriconi [28]. Li et al. [27] reported that the maximum reduction in compressive strength was 13.3%, with the inclusion of 0.3% powder silane-based water repellent addictive. Similarly, Tittarelli and Moriconi [28] found out that 2% of silane admixture used in the form of aqueous emulsion also caused a 10–20% reduction in compressive strength of concrete. The hydrophobic admixture may be associated with minor air-entraining effect, which increased the porosity in the hardened cement mortar [16].

Softening coefficient is the ratio between the water-saturated compressive strength and dry compressive strength of a material. The purpose of determining the ability of a material to maintain its original properties when exposed to water is because the moisture content of concrete has a significant effect on the compressive strength of concrete [29], especially for low strength material. The water-saturated specimens were prepared by immersing the oven-dried specimens in water for 48 hours. The softening coefficient of PM + 0.50PVA was 0.50. With 1% and 2% of water repellent admixture, the softening coefficients of PM + 0.50PVA were increased by 70% and 62%, respectively.

TABLE 4: Compressive strength, softening coefficient, and water absorption of LCC with water repellent admixture.

Mix ID	Compressive strength (MPa)		Softening coefficient	Water absorption (%)	
	Dry strength	Water-saturated strength		30 mins	48 hours
PM + 0.50 PVA	16.5	8.3	0.50	4.1	15.2
W1 PM + 0.50 PVA	10.9	9.2	0.85	0.7	3.6
W2 PM + 0.50 PVA	12.1	9.8	0.81	0.5	3.8

The PVA fibre-reinforced LCC with 1% admixture (W1PM + 0.50PVA) can be considered as a water-resistant material since the softening coefficient exceeds 0.85 [30]. The increment in softening coefficient is attributed to the lower water absorption of LCC specimens in the presence of the silane-based water repellent admixture. Compared with PM + 0.50PVA, the 48-hour water absorption of W1PM + 0.50PVA and W2PM + 0.50 PVA was reduced by 76.3% and 74.8%, respectively. Moreover, there is no significant difference between LCC performance with 1% and 2% water repellent admixture. Thus, the ideal dosage of silane-based water repellent admixture for the LCC in this research is 1%.

3.4. Flexural Strength.

The flexural strengths of LCCs are presented in Figure 6, while Figure 7 shows the fractured specimens after the 3-point bending test. Compared with the control specimen, all fibre-reinforced composites showed an appreciable increase in flexural strength. Theoretically, higher fibre dosage helps to sustain more load before failure, which can be observed in specimens with PVA fibres. When PVA fibres were added at 0.125%, 0.25%, and 0.50% dosage, the flexural strength was consistently enhanced by 14.3%, 25.7%, and 28.6%, respectively. Toutanji et al. [31] similarly reported that 0.6% PVA fibres increased the flexural strength of LCC by 25%. However, PP and basalt fibres showed otherwise.

For the specimen with PP fibres, fibre dosage at 0.125% minimally decreased the flexural strength (−3.9%). The possible reason is that 0.125% of PP fibre dosage was insufficient to have a significant fibre bridging effect, and the low modulus of elasticity of PP fibres makes the specimen less stiff. At 0.50% dosage of PP fibres, the flexural strength of PM-0 was improved by about 10%. A similar finding has been reported by Wu et al. [32], where incorporating 0.50% PP fibres in peach shell lightweight concrete increased the flexural strength by about 12%. On the other hand, for LCC-basalt, the flexural strength decreased from 5.0 MPa to 4.1 MPa at fibre dosage 0.25% and 0.50%. This was most likely due to the high aspect ratio and high modulus of basalt fibres having a detrimental effect on workability, hindering the basalt fibres from distributing homogeneously [23]. Hence, this can affect the compaction of the specimen.

Among the three types of fibre, namely, the PP, PVA, and basalt fibres, the basalt fibres gave the highest improvement in flexural strength (PM + 0.25B) followed by PVA fibres (PM + 0.50PVA) and PP fibres (PM + 0.50PP). This could be related to the stiffness of fibre. Basalt fibre has the highest modulus of elasticity, about 100–110 GPa; thus, it has better resistance to deformation of specimens [20]. However, the prismatic specimen of LCC-basalt broke into half after testing, as shown in Figure 7(b). This could be due to the rupture of basalt fibres since it possesses high stiffness [20]. Nevertheless, the fibres could still bridge the specimens from breaking into half in the case of LCC-PP and LCC-PVA (Figures 7(c) and 7(d)). Additionally, from Figures 8(c) and 8(d), fibres pull-out failure was observed. This shows that PP and PVA fibres could resist tensile stresses effectively. Besides that, LCC-PVA had wider crack width compared with LCC-PP. The reason is that the PVA fibres have higher tensile strength than PP fibres, thus allowing LCC-PVA to undergo greater deflection.

Furthermore, the effect of waterproofing admixture on the flexural strength of LCC was studied. The result shows that with 1% and 2% silane-based water repellent agent, the flexural strength of PM + 0.50PVA was decreased by 13.3% and 17.8%, correspondingly. This further justifies the finding in the earlier section where the porosity of LCC was increased after incorporating the hydrophobic agent.

3.5. Static Water Contact Angle.

The contact angles of water droplets on LCC tiles with different dosages of silane-based water repellent are presented in Figure 9. These results were used to determine the hydrophobicity of a material. When the water droplet remains on the surface in the form of a sphere, as shown in Figure 10 (hydrophobic surface), this indicates that there is no molecular attraction between water and the composite. In general, a solid surface with a water contact angle, $\theta \geq 90°$, is considered as hydrophobic, while a solid surface with $\theta \geq 120°$ and $\theta \leq 150°$ is considered as over hydrophobic. On the other hand, a solid surface with θ less than or equal to 90° is considered hydrophilic [33–35]. The hydrophobic properties of LCC were improved with the use of silane-based water repellent admixture. The water contact angle of W1PM + 0.50PVA and W2PM + 0.50PVA was 128.2° and 109.2°, respectively. It was 33% and 13% higher than the corresponding mix without water repellent admixture, PM + 0.50PVA. Therefore, the surface of W1PM + 0.50PVA is considered as over hydrophobic, while W2PM + 0.50PVA is considered as hydrophobic. The hydrophobic properties of LCC will be advantageous for industrial applications such as façade panels since surface staining can be avoided.

From the water contact angle results, 1% of silane-based water repellent is recommended, similar as described in the earlier section. It is interesting to note that even without the inclusion of silane-based water repellent admixture, the water contact angle of PM + 0.50PVA tile was still larger than 90°, which is considered hydrophobic. This result agrees well with the findings of Flores et al. [36] where the water contact angle of mortar tile was enhanced by about 26% using 1% PVA fibres. The incorporation of PVA fibres increased the
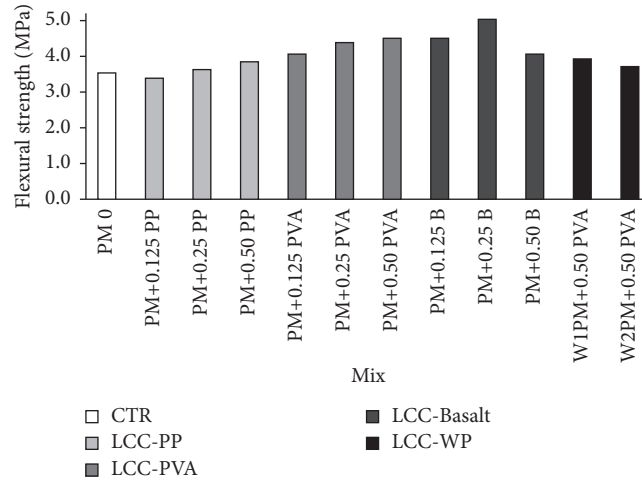
Figure 6: Flexural strength of LCC at 28 days.

(a)

(b)

(c)

(d)

Figure 7: Fractured LCC after 3-point bending test: (a) control mix; (b) LCC-basalt; (c) LCC-PVA; (d) LCC-PP.

(a)

(b)
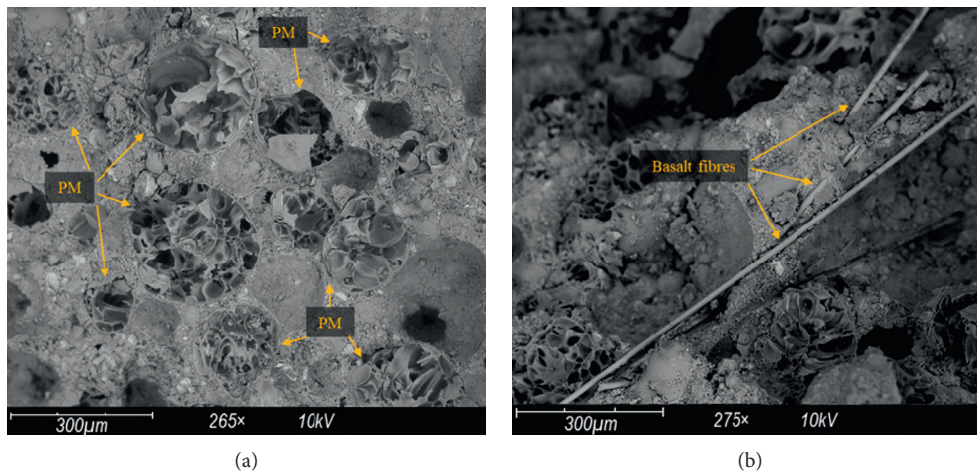
Figure 8: Continued.
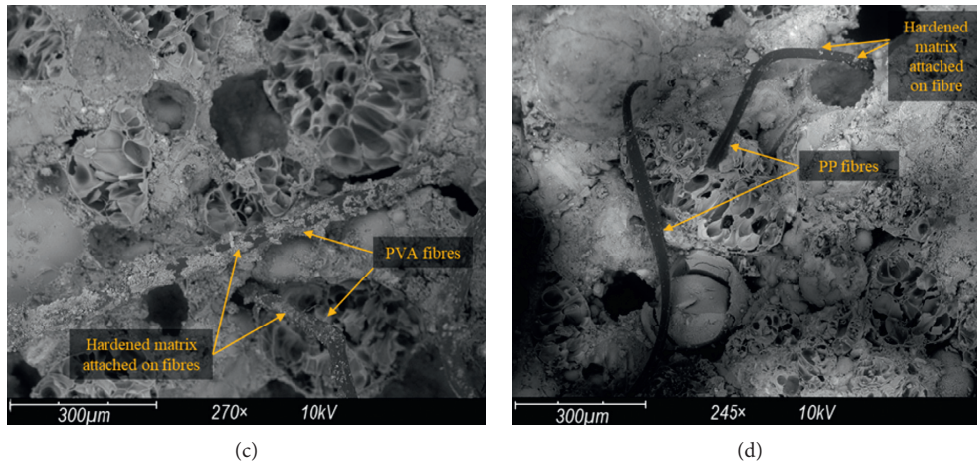
FIGURE 8: SEM images of (a) control mix; (b) LCC-basalt; (c) LCC-PVA; (d) LCC-PP.

(a)

(b)

(c)
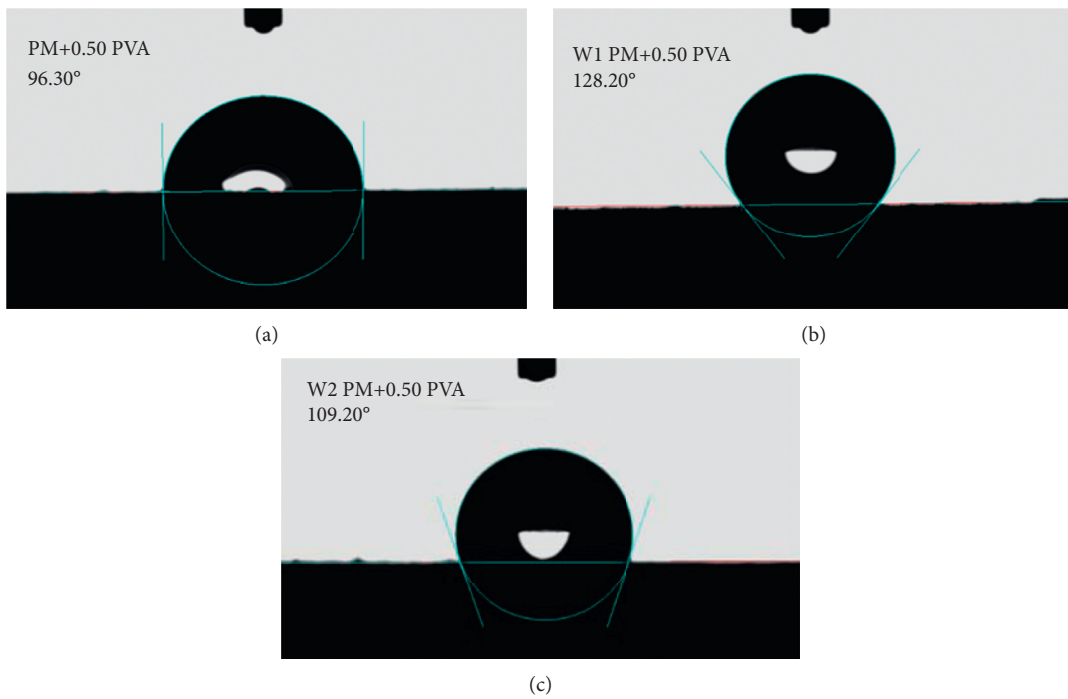
FIGURE 9: Water contact angle of LCC. (a) PM + 0.50PVA, (b) W1 PM + 0.50PVA, and (c) W2 PM + 0.50PVA.
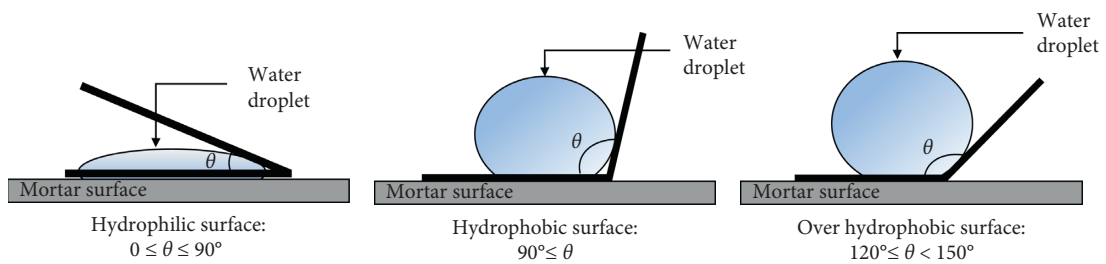
FIGURE 10: Range of water contact angle for hydrophilic, hydrophobic, and over hydrophobic surfaces [36].

surface roughness of the PM + 0.50 PVA tile and consequently lowered the surface energy and enhanced the hydrophobic properties of the material.

4. Conclusion

In this study, the effects of fibres and silane-based water repellent admixture on fresh and hardened properties of LCC were investigated. Based on the experimental results, the following conclusions can be drawn:

(i) The workability of LCC decreased with the increasing fibre dosage. LCC with 0.5% basalt fibre experienced the highest reduction in workability as basalt fibre has a higher modulus of elasticity and aspect ratio than the PP and PVA fibres.

(ii) The dry density of LCC developed was in the range of 912–985 kg/m^3.

(iii) The failure mechanism of LCC was improved with the use of fibres. The PP, PVA, and basalt fibres are effective in constraining lateral deformation and reducing the brittleness of LCC.

(iv) An optimised amount of fibre is crucial in improving the mechanical strength of LCC. The ideal PP, PVA, and basalt fibre dosage in this study is 0.5%, 0.5%, and 0.25%, respectively. Among all the mixes, LCC with 0.5% PVA fibre achieved the highest compressive strength of 16.5 MPa.

(v) The addition of fibre into LCC increased the flexural strength by 3.9% to 43.5%. The highest flexural strength achieved was 5.0 MPa when 0.25% basalt fibre was incorporated.

(vi) Although silane-based water repellent admixture reduced the compressive and flexural strengths of LCC, it has an excellent effect in reducing the water absorption of LCC. The ideal dosage of silane-based water repellent admixture for the LCC is 1%.

(vii) With 1% silane-based water repellent admixture and 0.5% PVA fibre, W1PM + 0.50PVA exhibited a softening coefficient of 0.85 and a water contact angle of 128.20°. Hence, W1PM + 0.50 PVA has the potential to be used in the fabrication of façade panels due to its adequate strength and hydrophobic properties.

Data Availability

The data used to support the findings of this study are available from the corresponding author upon request.

Conflicts of Interest

The authors declare that they have no conflicts of interest.

Acknowledgments

References

[1] M. Jedidi, O. Benjeddou, and c. soussi, "Effect of expanded perlite aggregate dosage on properties of lightweight concrete," *Jordan Journal of Civil Engineering*, vol. 9, pp. 278–291, 2015.

[2] O. Sengul, S. Azizi, F. Karaosmanoglu, and M. A. Tasdemir, "Effect of expanded perlite on the mechanical properties and thermal conductivity of lightweight concrete," *Energy and Buildings*, vol. 43, no. 2-3, pp. 671–676, 2011.

[3] M. Ibrahim, A. Ahmad, M. S. Barry, L. M. Alhems, and A. C. Mohamed Suhoothi, "Durability of structural lightweight concrete containing expanded perlite aggregate," *International Journal of Concrete Structures and Materials*, vol. 14, no. 1, p. 50, 2020.

[4] A. G. Celik, A. M. Kilic, and G. O. Cakal, "Expanded perlite aggregate characterization for use as a lightweight construction raw material," *Physicochemiacal Problems Mineral Proceesing*, vol. 49, no. 2, pp. 689–700, 2013.

[5] P. M. Angelopoulos, M. Taxiarchou, and I. Paspaliaris, "Production of durable expanded perlite microspheres in a Vertical Electrical Furnace," *IOP Conference Series: Materials Science and Engineering*, vol. 123, Article ID 012061, 2016.

[6] K. Sodeyama, Y. Sakka, Y. Kamino, and H. Seki, "Preparation of fine expanded perlite," *Journal of Materials Science*, vol. 34, no. 10, pp. 2461–2468, 1999.

[7] Q. Jing, L. Fang, H. Liu, and P. Liu, "Preparation of surface-vitrified micron sphere using perlite from Xinyang, China," *Applied Clay Science*, 2011.

[8] G. W. Leong, K. H. Mo, Z. P. Loh, and Z. Ibrahim, "Mechanical properties and drying shrinkage of lightweight cementitious composite incorporating perlite microspheres and polypropylene fibers," *Construction and Building Materials*, vol. 246, 2020.

[9] L. Kidalova, N. Stevulova, E. Terpakova, and A. Sicakova, "Utilization of alternative materials in lightweight composites," *Journal of Cleaner Production*, vol. 34, pp. 116–119, 2012.

[10] N. Banthia and R. Gupta, "Hybrid fiber reinforced concrete (HyFRC): fiber synergy in high strength matrices," *Materials and Structures*, vol. 37, no. 10, pp. 707–716, 2004.

[11] Z. Dong, M. Deng, C. Zhang, Y. Zhang, and H. Sun, "Tensile behavior of glass textile reinforced mortar (TRM) added with short PVA fibers," *Construction and Building Materials*, vol. 260, Article ID 119897, 2020.

[12] Y. Du, M. Zhang, F. Zhou, and D. Zhu, "Experimental study on basalt textile reinforced concrete under uniaxial tensile loading," *Construction and Building Materials*, vol. 138, pp. 88–100, 2017.

[13] Y. Qin, X. Zhang, J. Chai, Z. Xu, and S. Li, "Experimental study of compressive behavior of polypropylene-fiber-reinforced and polypropylene-fiber-fabric-reinforced concrete," *Construction and Building Materials*, vol. 194, pp. 216–225, 2019.

[14] M. Y. L. Chew and P. P. Tan, "Facade staining arising from design features," *Construction and Building Materials*, vol. 17, no. 3, pp. 181–187, 2003.

[15] Y. Xu and D. D. L. Chung, "Cement of high specific heat and high thermal conductivity, obtained by using silane and silica fume as admixtures," *Cement and Concrete Research*, vol. 30, no. 7, pp. 1175–1178, 2000.

[16] B. Yan, F. Ren, M. Cai, and C. Qiao, "Influence of new hydrophobic agent on the mechanical properties of modified cemented paste backfill," *Journal of Materials Research and Technology*, vol. 8, no. 6, pp. 5716–5727, 2019.

[17] K. Xu, S. Ren, J. Song et al., "Colorful superhydrophobic concrete coating," *Chemical Engineering Journal*, vol. 403, Article ID 126348, 2021.

[18] C. Chen, Y. Wang, G. Pan, and Q. Wang, "Gel-sol synthesis of surface-treated TiO2 nanoparticles and incorporation with waterborne acrylic resin systems for clear UV protective coatings," *Journal of Coatings Technology and Research*, vol. 11, no. 5, pp. 785–791, 2014.

[19] C. H. Jiang, S. S. Huang, Y. W. Zhu, Y. F. Lin, and D. Chen, "Effect of polypropylene and basalt fiber on the behavior of mortars for repair applications," *Annals of Materials Science & Engineering*, 2016.

[20] Z. P. Loh, K. H. Mo, C. G. Tan, and S. H. Yeo, "Mechanical characteristics and flexural behaviour of fibre-reinforced cementitious composite containing PVA and basalt fibres," *Sādhanā*, vol. 44, no. 4, p. 98, 2019.

[21] Y. Ohama, "Polymer-based admixtures," *Cement and Concrete Composites*, vol. 20, no. 2, pp. 189–212, 1998.

[22] T. Wu, X. Yang, H. Wei, and X. Liu, "Mechanical properties and microstructure of lightweight aggregate concrete with and without fibers," *Construction and Building Materials*, vol. 199, pp. 526–539, 2019.

[23] C. Jiang, K. Fan, F. Wu, and D. Chen, "Experimental study on the mechanical properties and microstructure of chopped basalt fibre reinforced concrete," *Materials & Design*, vol. 58, pp. 187–193, 2014.

[24] CEB, *Functional Classification of Lightweight Concrete, Recommendations LC2*, RILEM Publications SARL, Stuttgart, Germany, 2nd edition, 1978.

[25] A. Hanif, Z. Lu, Y. Cheng, S. Diao, and Z. Li, "Effects of different lightweight functional fillers for use in cementitious composites," *International Journal of Concrete Structures and Materials*, vol. 11, no. 1, pp. 99–113, 2017.

[26] F. Blanco, P. Garćia, P. Mateos, and J. Ayala, "Characteristics and properties of lightweight concrete manufactured with cenospheres," *Cement and Concrete Research*, vol. 30, no. 11, pp. 1715–1722, 2000.

[27] H. Li, C. Xu, B. Dong, Q. Chen, L. Gu, and X. Yang, "Enhanced performances of cement and powder silane based waterproof mortar modified by nucleation C-S-H seed," *Construction and Building Materials*, vol. 246, Article ID 118511, 2020.

[28] F. Tittarelli and G. Moriconi, "The effect of silane-based hydrophobic admixture on corrosion of reinforcing steel in concrete," *Cement and Concrete Research*, vol. 38, no. 11, pp. 1354–1357, 2008.

[29] J. Shen and Q. Xu, "Effect of moisture content and porosity on compressive strength of concrete during drying at 105 °C," *Construction and Building Materials*, vol. 195, pp. 19–27, 2019.

[30] T.-C. Ling, K. H. Mo, L. Qu, J. Yang, and L. Guo, "Mechanical strength and durability performance of autoclaved lime-saline soil brick," *Construction and Building Materials*, vol. 146, pp. 403–409, 2017.

[31] H. Toutanji, B. Xu, J. Gilbert, and T. Lavin, "Properties of poly(vinyl alcohol) fiber reinforced high-performance organic aggregate cementitious material: converting brittle to plastic," *Construction and Building Materials*, vol. 24, no. 1, pp. 1–10, 2010.

[32] F. Wu, C. Liu, Z. Diao et al., "Improvement of mechanical properties in polypropylene- and glass-fibre-reinforced peach shell lightweight concrete," *Annals of Materials Science & Engineering*, vol. 2018, p. 11, 2018.

[33] S. Muzenski, I. Flores-Vivian, and K. Sobolev, "Hydrophobic engineered cementitious composites for highway applications," *Cement and Concrete Composites*, vol. 57, pp. 68–74, 2015.

[34] L. Yao and J. He, "Recent progress in antireflection and self-cleaning technology - from surface engineering to functional surfaces," *Progress in Materials Science*, vol. 61, pp. 94–143, 2014.

[35] S. Karthick, D.-J. Park, Y. S. Lee et al., "Development of water-repellent cement mortar using silane enriched with nano-materials," *Progress in Organic Coatings*, vol. 125, pp. 48–60, 2018.

[36] I. Flores Vivian, V. Hejazi, M. Kozhukhova, M. Nosonovsky, and K. Sobolev, "Self-assembling particle-siloxane coatings for superhydrophobic concrete," *ACS Applied Materials and Interfaces*, vol. 5, 2013.

Research Article

New Anticracking Glass-Fiber-Reinforced Cement Material and Integrated Composite Technology with Lightweight Concrete Panels

Dong Chen,[1] **Junjie Deng,**[1] **Baoquan Cheng** (iD)**,**[2] **Qiong Wang,**[3] **and Baojun Zhao**[3]

[1]*BIM Engineering Center of Anhui Province, Anhui Jianzhu University, Hefei, Anhui 230601, China*
[2]*School of Civil Engineering, Central South University, Changsha, Hunan 410083, China*
[3]*Shenzhen Hailong Construction Technology Company Limited, Shenzhen, Guangdong 518000, China*

Correspondence should be addressed to Baoquan Cheng; curtis_ch@163.com

Glass-fiber-reinforced cement (GRC) is a widely used decorative material for wall facades. Conventional GRC products have poor crack resistance, low construction efficiency, poor integration, and few environmental benefits, hence failing to meet the requirements of building industrialization. To realize an integrated composite wall made from GRC and precast lightweight concrete (PLC) with a lasting anticrack effect, the anticracking properties of GRC material as well as the connection mode of GRC and PLC layers were studied. Through long-term shrinkage test, the influence of fiber content, rubber powder content, and expansion agent content on the crack resistance of GRC material was systematically analyzed. At the same time, the influence of connection mode on the crack resistance of the GRC layer after compositing with precast lightweight concrete (PLC) was analyzed. The results showed that adding fiber can effectively improve the flexural strength of the GRC and reduce drying shrinkage, whereas adding rubber powder can effectively improve its toughness and crack resistance. The addition of U-type expansion agent (UEA) can impart the cement mortar with a certain degree of microexpansion performance and help improve the drying shrinkage of the GRC. Compared with other compounding methods, the smooth connection of the GRC and PLC can effectively reduce the shrinkage of the GRC surface layer and improve its crack resistance. So, the new GRC material has good crack resistance performance and facade effect. These research studies provide an experimental basis for the large-scale application of the panel, and it has great advantages in improving the efficiency of prefabricated building construction.

1. Introduction

Most external walls of modern buildings use external insulation and lacquer material. The exterior walls typically deteriorate in approximately five years, bringing security risks [1]. Glass-fiber-reinforced cement (GRC) is a type of composite material composed of a cement mortar as the base material and alkali-resistant glass fiber as an additional component. It is considered a green building material and has characteristics such as energy savings and environmental protection. At the same time, greenhouse gas emissions from building construction can be reduced [2]. Precast lightweight concrete (PLC) is a kind of precast lightweight aggregate concrete. It is made of light plastic particles, ordinary

sand, cement, and water. The PLC strength grade in this paper was LC15 (i.e.15 MPa) [3]. A GRC-PLC-integrated composite panel (Figure 1) can effectively ensure wall insulation and reduce the generation of waste, waste gas, and wastewater in buildings. The type of fiber used has a significant influence on the plastic shrinkage and cracking of concrete. Experimental results have shown that glass fiber imparts better mechanical properties and economy when added to concrete products [4–7]. El-Dieb and Reda Taha [8] reported an improvement in the self-compacting performance of concrete when incorporated with glass fibers, thereby reducing cracks and increasing its strength. Li et al. [9] studied the effect of glass fibers of different dimensions on the flexural performance of GRC and experimentally
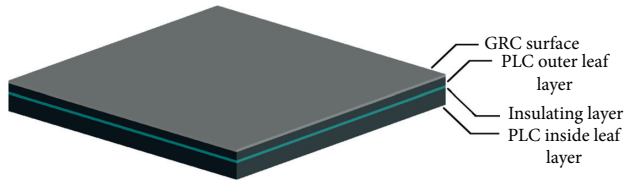
Figure 1: Three-dimensional model of a GRC-PLC-integrated panel.

showed that the higher the dimensions of the glass fiber, the better the strength and toughness of the GRC material. Because of the alkalinity of cementitious materials, the GRC becomes brittle, and the material strength is reduced. The use of additives can prevent GRC embrittlement [10–13]. The results of cracking and shrinkage experiments conducted on GRC materials and the analysis of fracture characteristics have shown that the addition of fly ash, rubber powder, expansion agent, and other materials can help effectively reduce the cracking and shrinkage of GRC [12–18]. Wu et al. [19] studied the shrinkage performance of GRC-based materials and showed that GRC materials made from different types of cement exhibit drying and autogenous shrinkage to varying degrees. When using GRC, the durability and strength of the material are important factors. By predicting the strength, durability, and aging degree of GRC materials, various strength and durability models have been proposed, assuming excessive loss of strength, to perform accelerated aging tests. The aging degree of GRC materials can be analyzed through nondestructive testing [20–23]. The cracking and deformation of GRC materials are significantly affected by the temperature. Correia et al. [24, 25] found that a GRC panel cracks and deforms excessively because of the thermal effect, GRC thickness, and dry humidity. Therefore, the effects of temperature and GRC thickness should be considered when monitoring the shrinkage strain of GRC panels.

In summary, current research on the physical and mechanical properties of GRC, such as the crack resistance, has mainly focused on a single GRC precast component, while studies on composite precast components made of GRC and PLC are lacking. But GRC and PLC are two different building materials, with different shrinkage properties. The shrinkage of PLC is smaller than that of GRC. After the composite, the PLC layer will hinder the shrinkage deformation of the GRC layer, thus tensile stress will be generated in the GRC layer. When the stress exceeds the tensile strength of the GRC, the GRC layer will produce cracks, which affects the overall facade effect of the decorative, integrated precast concrete component. So, it was studied from three aspects: reducing GRC material shrinkage, improving the tensile strength of GRC materials, and determining the most effective connection method for the GRC and PLC layers.

The research ideas of this paper are as follows. First of all, an anticrack GRC formula was developed. Considering the temperature and humidity, the effects of fiber content, rubber powder content, expansion agent content on the crack resistance of the GRC surface layer were systematically studied. And the flexural strength and dry shrinkage of the material were measured. Second, according to the different connection methods of GRC layer and PLC layer, seven panels of 1 m × 1 m were prepared, and the shrinkage experiment was carried out for 365 days in environments with different temperature and humidity. Among them, the crack resistance of GRC layer was the core of the test. Finally, according to experimental results, the anticrack GRC formula and reasonable connection method between GRC layer and PLC layer were determined. Findings from this research contribute to the application of GRC-PLC composite panels and promotion of prefabrication.

2. Materials and Methods

2.1. Materials

2.1.1. Raw Materials. The main materials used in the experiment were GRC cement mortar and precast lightweight concrete. The GRC material was made on the experimental site, and raw materials of GRC were cement (for use as PW 52.5 grade white silicate cement); sand (for use as river sand, the fineness modulus is 1.4); water-reducing admixture (for use as PCA-1 polycarboxylate superplasticizer); fiber (shortcut alkali-resistant glass, the density is $2.68 \, \text{g/cm}^3$, the elastic modulus is 72 GPa, the tensile strength is 1700 MPa, and the diameter is $14 \, \mu\text{m}$); rubber powder (for use as redispersible emulsion powder), and U-type expansion agent (mainly composed of aluminum sulfate, aluminum oxide, aluminum potassium sulfate, and other expansive sources, which can improve the crack resistance of materials). PLC was used in the form of a ready-mix concrete provided by commercial concrete company. After the composite wall panel was poured, the surface of the wall panel was covered with plastic film for curing. The curing method was three times of watering in the morning, middle, and night, lasting three days, and the targeted strength of PLC was 15 MPa.

2.1.2. GRC Mix Proportion Design. In the preparation process of GRC materials, some experimental studies have shown that their fluidity and shrinkage are affected by the contents of glass fiber, rubber powder, and expansion agent [26–31]. Adding glass fiber can help reduce the generation and expansion of cracks; however, too high or too low a glass fiber content will produce different degrees of cracking in GRC materials [26–28]. Adding rubber powder into a GRC material can reduce internal voids, improve the hydrophilicity of cement, and improve the flexibility and fluidity of the GRC material. The addition of an expansion agent into concrete can help reduce the bonding cracks between the hydration products and aggregates and reduce the cracks due to drying shrinkage of materials [26, 29, 31].

The materials used in the new GRC anticrack formulation research include cement, sand, fly ash, metakaolin, water-reducing admixture, glass fiber, rubber powder, and expansion agent. The fly ash and metakaolin used can replace a part of the cement, reduce the amount of cement, decrease the hydration rate, and reduce the cracking and

shrinkage of GRC materials. The emulsified rubber powder has the effect of bonding polymerization and improves the bonding strength between the cement, aggregate, and fiber. The crack resistance of a GRC material can be improved by adding glass fiber and U-type expansion agent. Table 1 lists the foundation mix proportion of the mortar. Table 2 lists the designed values of the fiber, rubber powder, and expansion agent. The contents of fly ash, metakaolin, water-reducing admixture, rubber powder, and expansion agent are a percentage of the total cementitious materials, whereas the fiber content is the percentage of the total mass of the sample. The content of fly ash and metakaolin was fixed at 10%, and the water reducer is content was fixed at 2%. In this study, the water-to-cement ratio of the mortar was designed as 0.28. It is proposed to reduce shrinkage and improve the tensile strength of cement-based materials, and the effects of fiber, rubber powder, and expansion agent on the mechanical properties and crack resistance of GRC were systematically studied: (1) the effects of 1%, 1.5%, and 2% fiber incorporation on the flexural strength and drying shrinkage properties of mortar were studied; (2) the effects of 1.5%, 2.5%, and 3.5% rubber powder on the flexural strength and drying shrinkage properties of the mortar were analyzed; and (3) on the basis of 1% fiber content, the effect of adding a certain amount of expansion agent on the drying shrinkage properties of the GRC was studied.

2.2. Experimental Equipment.

In the experiment, concrete mixer was used to stir the GRC materials. The mixer has advantages of convenient operation, high mixing efficiency, and convenient cleaning. It is an ideal concrete mixing equipment for laboratory use. The flexural tester was used to measure the flexural strength of the specimen. The maximum test force was 1 kN when the single lever was used, and the maximum test force was 5 kN when the double lever was used. The accuracy was in the range of 0.4–1.0 N. The comparator, depending on the requirements, can help determine the GRC specimens at each age of the shrinkage rate. The static strain tester was used to connect the surface strain gauge and embedded strain gauge to monitor the shrinkage strain of the composite panel over a long duration. Figure 2 shows the experimental equipment.

2.3. Specimen Preparation

2.3.1. Preparation of Specimen for Flexural Experiment.

In the experiment, the fiber and cement were mixed for 3 min, and it was put into concrete mixer (the capacity of the mixer was 60 L, and the rotational speed of the stirring shaft was 45 ± 2 r/min). Then water and sand were added, and the mixture was poured into a 40 mm × 40 mm × 160 mm mold after mixing. After molding, the specimens were cured in a standard environment for 24 h (temperature $20°C \pm 2°C$, relative humidity above 95% RH). When the standard curing specimen was removed from the mold, it was placed in an adjustable temperature and humidity box, and different relative humidity (RH = 40% and RH = 70%) values were set. Table 3 presents the number of specimens. The fiber contents were 1%, 1.5%, and

2%. The rubber powder contents were 1.5%, 2.5%, and 3.5%. Under RH = 40% and RH = 70%, specimens of different material contents were prepared, and three specimens of each content were made. The specimens were cured to the specified age, and the corresponding specimen was removed from the adjustable temperature and humidity box. The flexural experiment was carried out using a flexural testing machine. The flexural strength at different specified ages was tested in accordance with ISO 679:2009 [32]. Thus, the flexural strength of GRC materials was measured under different RH values.

2.3.2. Preparation of Specimen for Drying Shrinkage Experiment.

The molding and curing processes employed for the drying shrinkage specimens were the same as those employed for the flexural specimens. A 25 mm × 25 mm × 280 mm triple mold was used, and nail heads were placed at both ends of the triple mold to make dry shrinkage test specimens. After molding, the specimens were cured in a standard environment for 24 h (temperature $20°C \pm 2°C$, relative humidity above 95% RH). After removing the mold, the specimens were placed in the adjustable temperature and humidity box for curing, $20 \pm 2°C$, and different relative humidity (RH = 40% and RH = 70%) values were set. Curing to different ages, dry shrinkage experiment was carried out to prepare the specimens, as shown in Figure 3. Table 4 lists the number of specimens. The fiber contents were 1%, 1.5%, and 2%. The rubber powder contents were 0%, 1.5%, 2.5%, and 3.5%. UEA content was 8%. Under RH = 40% and RH = 70%, specimens of different material contents were prepared, and three specimens of each content were made. A comparator was used to measure the specimen length at different curing ages. So, the drying shrinkage of GRC materials was measured under different RH values. The calculation formula for the drying shrinkage rate of the cement mortar at different ages is as follows:

$$P_t = \frac{L_t - L_0}{250} \times 100\%, \tag{1}$$

where P_t is the drying shrinkage rate on day t (mm); the effective length of the mortar specimen is 250 mm; L_t is the measured length of the mortar specimen on day t (mm); and L_0 is the initial length of the mortar specimen (mm).

2.3.3. Specimens Prepared Using Different Connection Methods.

A total of seven composite panels were used in the experiment. Table 5 lists their dimensions and parameters, where T0 was a pure GRC panel without fiber, T1 was a pure lightweight concrete panel with a thickness of 60 mm, and T2 was a pure GRC panel with a thickness of 15 mm. These two types of panels were used as the basis for the experiment.

T3–T6 were GRC-PLC composite panels made according to Figure 1, which ignored the concrete structure layer and the insulation layer, as shown in Figure 4. The T3 and T4 panels have different GRC material thicknesses. It was used to study the effect of different GRC material thickness on the shrinkage performance of composite panel.

Based on the actual application of the composite panel, the common connection modes for composite panels include smooth connection, rough connection, and laying steel mesh

TABLE 1: Mortar mix proportion.

Type	Cement (kg/m^3)	Sand (kg/m^3)	Water (kg/m^3)	Fly ash (kg/m^3)	Metakaolin (kg/m^3)	Water-reducing admixture (kg/m^3)
Content	888	1248	322	56	166	31

TABLE 2: Values of fiber, rubber powder, and expansion agent contents.

Number	Fiber content (%)	Rubber powder content (%)	U-type expansion agent content (%)
1	1	0	0
2	1.5	0	0
3	2	0	0
4	2	1.5	0
5	2	2.5	0
6	2	3.5	0
7	1	0	8
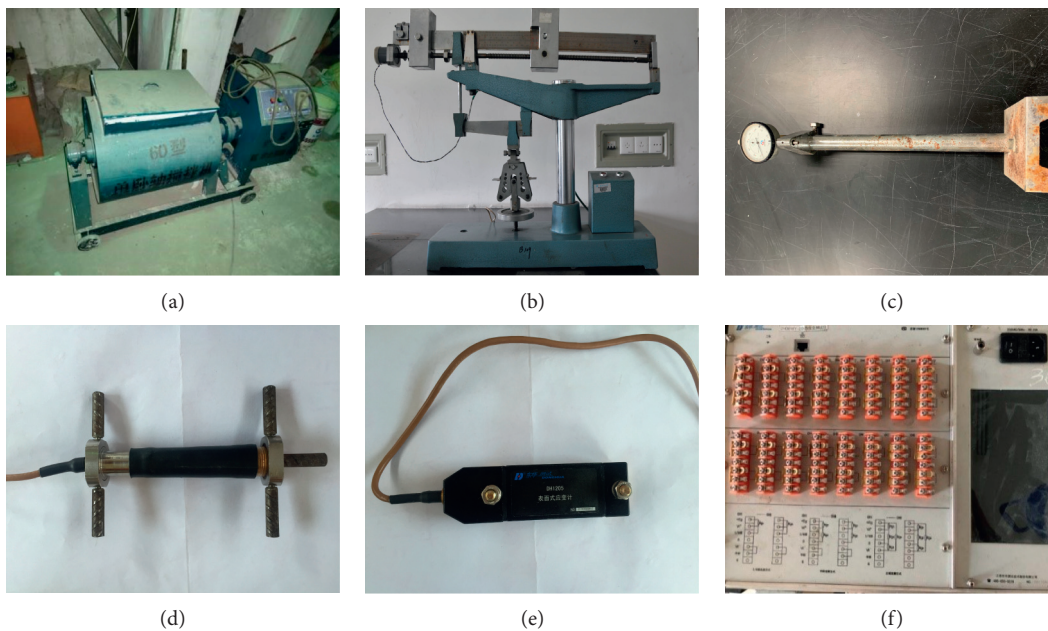
FIGURE 2: Experimental equipment. (a) Concrete mixer. (b) Flexural testing machine. (c) Comparator. (d) Embedded strain gauge. (e) Surface strain gauge. (f) Strain tester.

TABLE 3: Number of specimens.

RH (%)	Materials (content)	Number (pcs)	Remarks
40	Fiber (1%, 1.5%, 2%)	9	Three specimens were prepared for each content
	Rubber powder (1.5%, 2.5%, 3.5%)	9	Three specimens were prepared for each content
70	Fiber (1%, 1.5%, 2%)	9	Three specimens were prepared for each content
	Rubber powder (1.5%, 2.5%, 3.5%)	9	Three specimens were prepared for each content

connection. T4–T6 differed in terms of the connection method of the composite interface, with T4 having a smooth connection, T5 having a rough connection, and T6 having a steel mesh connection. The influence of the connection methods on the shrinkage performance of the composite panels was studied.

The design ideas of these panels were as follows: T0 was a panel without fiber, which was mainly used to observe the development trend of cracks, so as to determine the location of the strain gauge. T3–T6 took the GRC thickness and the

connection methods as variables to determine the suitable structure type of GRC-PLC composite panel. The shrinkage experiment was carried out for 12 months to monitor the change of shrinkage strain in GRC and PLC with different temperature and humidity.

Before the experiment, the wood formwork was checked and cleaned. The ready-mix lightweight concrete was poured to a specified height while minimizing bubbles using hand-held vibrating rods. To weigh the required GRC anticracking

FIGURE 3: Preparation of drying shrinkage test specimen.

TABLE 4: Number of specimens.

RH (%)	Materials (content)	Number	Remarks
40	Fiber (1%, 1.5%, 2%)	9	Three specimens were prepared for each content
	Rubber powder (0%, 1.5%, 2.5%, 3.5%)	12	Three specimens were prepared for each content
	1% fiber + 8% UEA	3	—
70	Fiber (1%, 1.5%, 2%)	9	Three specimens were prepared for each content
	Rubber powder (0%, 1.5%, 2.5%, 3.5%)	12	Three specimens were prepared for each content

TABLE 5: Parameters of a new GRC-PLC composite panel.

Specimen number	Specimen size (length × width × height) (mm³)	PLC material thickness (mm)	GRC material thickness (mm)	Interface connection method
T0	1000 × 1000 × 15	—	15	—
T1	1000 × 1000 × 60	60	—	—
T2	1000 × 1000 × 15	—	15	—
T3	1000 × 1000 × (60 + 10)	60	10	Smooth
T4	1000 × 1000 × (60 + 15)	60	15	Smooth
T5	1000 × 1000 × (60 + 15)	60	15	Rough
T6	1000 × 1000 × (60 + 15)	60	15	Laying steel mesh
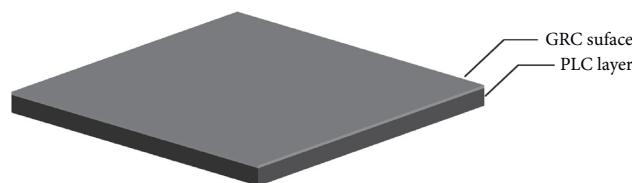
FIGURE 4: GRC-PLC composite panel.

material based on the design mix proportion, a concrete mixer was used for mixing; subsequently, water and the water-reducing agent are added in a sequence every 8 min. After the GRC material was stirred, it was poured on the surface of the lightweight concrete, and the surface was levelled using a roller brush while ensuring a bubble-free surface. Thus, the effects of GRC layer thickness and type of composite method used for the composite interfaces (smooth, rough, and laying steel mesh) on the shrinkage properties of the GRC-PLC composite panels were studied. When pouring T5 and T6 composite panels, the composite interface was processed using rough and laying steel meshes. The strain gauge was placed in the pouring material at the same time. When pouring PLC, the embedded strain gauge was placed inside it. When pouring the GRC, the surface strain gauge was prevented from sinking and contacting the PLC given the softness of the GRC material. It was placed using a wooden stick on the template, and a string was used for fixing. Figure 5 shows the placement of the strain gauges and the experimental process. The two strain gauges were connected to the static strain tester, and the panel surface was covered using a fresh-keeping film. Water was sprayed onto the panel surface for seven days in the morning, midday, and evening. The

(a)

(b)
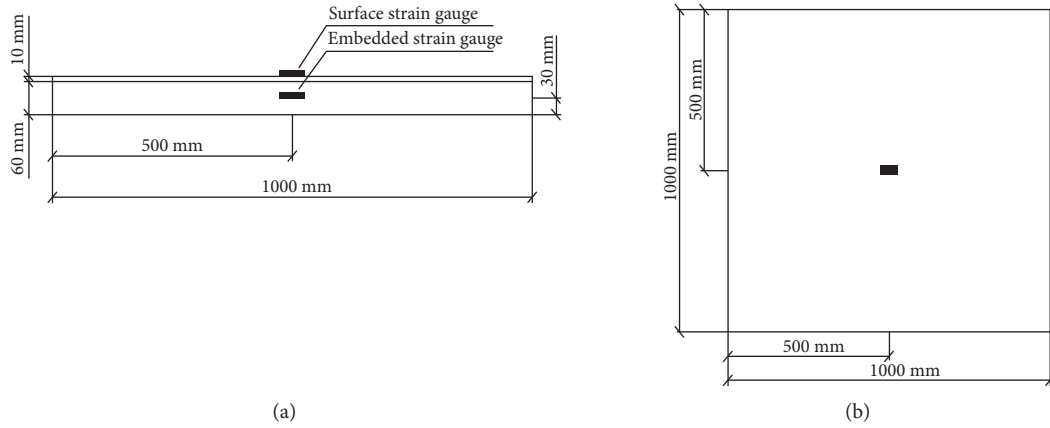
(c)
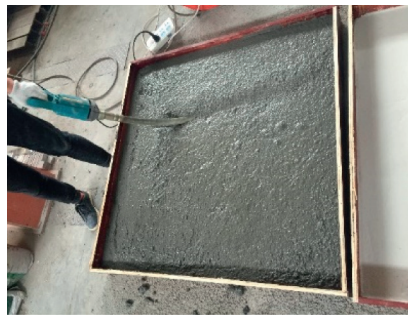
(d)
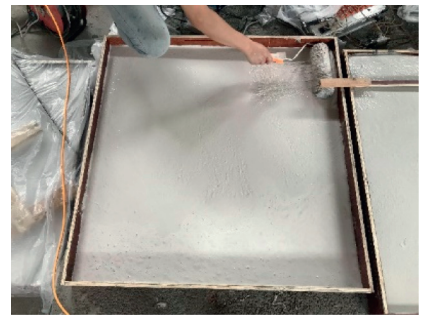
(e)

(f)

(g)

(h)
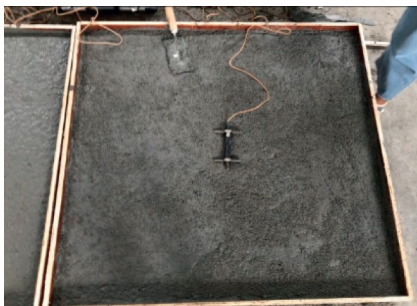
(i)

(j)

(k)

FIGURE 5: Composite panel production process. (a) Location of surface strain gauge. (b) Location of embedded strain gauge. (c) Mixing GRC. (d) Vibration rod vibration. (e) Roller brushing. (f) Smooth connection. (g) Rough connection. (h) Laying steel mesh connection. (i) Embedded strain gauge. (j) Surface strain gauge. (k) Fixed surface strain gauge.

shrinkage strain value of the GRC-PLC composite board was continuously monitored, and the temperature and humidity were recorded every morning, midday, and evening.

3. Results and Discussion

3.1. Effect of Material Compositions on Flexural Strength and Drying Shrinkage Properties of GRC

3.1.1. Effects of Fiber and Rubber Powder Contents on Flexural Strength of GRC. Figure 6 shows the flexural strength histogram of mortars with different fibers and rubber powder contents under a relative humidity of 40%. Figure 6(a) shows that when the fiber contents are 1%, 1.5%, and 2%, the flexural strengths of the mortar cured for 28 days are 11.9, 13.5, and 15.6 MPa, respectively. This shows that the flexural strength of the mortar can be improved with the increase in the fiber content. The main reason is that the glass fiber can improve the tensile strength and deformation ability of the mortar, and it can prevent the expansion of the original microcracks in the mortar and delay the generation of new cracks [33]. Based on a 2% fiber content, after adding 1.5%, 2.5%, and 3.5% rubber powder, the flexural strengths of the mortar on the 28th day were 16.1, 16.7, and 15.2 MPa, respectively, as shown in Figure 6(b). The flexural strength of the mortar can be continuously and effectively improved when the rubber powder content is <2.5%. The main reason is that the flexural strength of the mortar is improved when adding an appropriate amount of rubber powder. The emulsified rubber powder has the effect of bonding polymerization and helps improve the bonding strength between the cement, aggregate, and fiber. However, when the rubber powder content is >2.5%, the flexural strength of the mortar begins to decrease. With the increase in the rubber powder content, too many voids are introduced [34], which increases the overall porosity of the mortar and reduces the bonding degree between the fiber and the mortar, thereby reducing the flexural strength of the mortar. Therefore, when the rubber powder content is <2.5%, the flexural strength can be continuously and effectively improved.

Figure 7 shows the flexural strength of the mortar with different fiber and rubber powder contents under a relative humidity of 70%. As shown in Figure 7(a), when the fiber contents are 1%, 1.5%, and 2%, the flexural strengths of the mortar cured for 28 days are 12.1, 15.8, and 17.9 MPa, respectively. Compared with the mortar cured under a relative humidity of 40%, the flexural strength of the mortar cured for 28 days with different fiber contents is higher. The main reason is that the hydration of cement under 70% relative humidity is more sufficient, the hydration strength increases, and the bonding force between the fiber and the cement-based material is further enhanced [35]. Figure 7(b) shows that with the incorporation of the rubber powder, the flexural strength of the mortar is consistent with that of the mortar prepared under 40% relative humidity. When the amount of rubber powder is >2.5%, the flexural strength of the mortar decreases. With the increase in the amount of rubber powder, the flexural strength increases first but then decreases on the 28th day.

### 3.1.2. Effects of Fiber, Rubber Powder, and Expansion Agent Contents on Drying Shrinkage Properties of GRC. The experiment of drying shrinkage was based on "Standard test methods for drying shrinkage and cracking possibility of cement mortar and concrete" (GB/T 29417-2012) [36] in this paper. This standard code has explained how to carry out the drying shrinkage experiment. However, the standard code did not specify the limit of drying shrinkage. Therefore, our drying shrinkage experiments were based on this specification.

(1) Effect of Fiber Content on Drying Shrinkage Performance of GRC. Figures 8(a) and 8(b) show the drying shrinkage rate of mortar specimens with different fiber contents prepared under 40% and 70% relative humidity, respectively. As shown, an increase in the fiber content from 1% to 2% has little effect on the drying shrinkage performance of the mortar. This is because the fiber can reduce the water loss area of the mortar, and the water transfer path is prolonged [37]. Moreover, the disorderly distribution of the fiber blocks the connectivity of the capillary in the mortar and reduces the capillary tension generated by the capillary water loss and contraction. Therefore, it is can reduce the dry shrinkage of the mortar. Therefore, in terms of the drying shrinkage characteristics, the fiber content should be no more than 1% to effectively inhibit the increase in the drying shrinkage rate. When the relative humidity increases from 40% to 70%, the shrinkage rate on the 28th day can be reduced by approximately 40%, which is evidently beneficial for reducing the shrinkage rate of the mortar specimens. Increasing the curing humidity during the curing process can significantly reduce the drying shrinkage of GRC materials.

(2) Effect of Rubber Powder Content on Drying Shrinkage of GRC. Figure 9 shows the shrinkage of mortar specimens with different amounts of rubber powder prepared at 40% and 70% relative humidity. The two line graphs show a rapid increase in the shrinkage rate within 0–7 days, indicating that the incorporation of rubber powder led to an increase in the shrinkage rate of the GRC and that the shrinkage rate increases gradually after seven days. Compared with the mortar without rubber powder, the dry shrinkage of the mortar is evidently increased with the increase in the amount of rubber powder. The main reason is that the addition of rubber powder increases the number of microholes in the mortar, thereby increasing the capillary tension and causing shrinkage. The drying shrinkage curves under 70% RH and 40% RH exhibit the same trend; however, the GRC drying shrinkage under 70% RH is relatively low. This shows that the drying shrinkage of the mortar can be effectively inhibited by increasing the curing humidity.

(3) Effect of U-Type Expansion Agent (UEA) Content on Drying Shrinkage Performance of GRC. Figure 10 shows the effect of the expansion agent on the shrinkage performance of the GRC under different humidity environments. As shown, when the humidity is 40%, the drying shrinkage rate of the GRC is significantly higher than that of the GRC

(a)

(b)
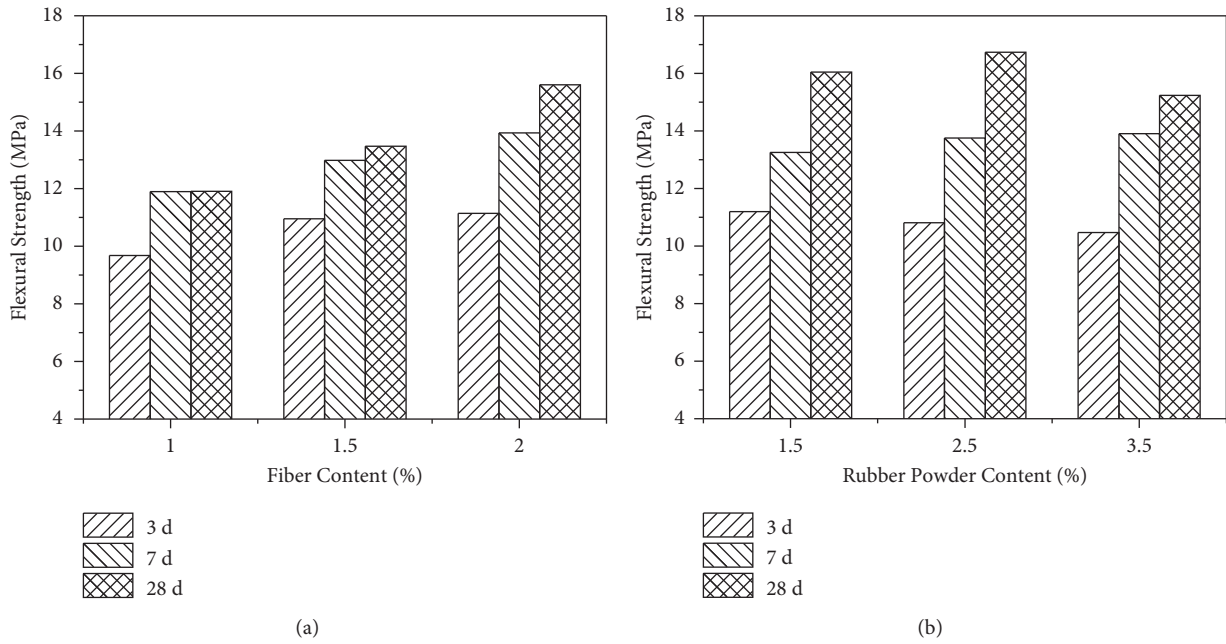
FIGURE 6: Flexural strength of mortar with different fiber and rubber powder contents when RH = 40%. (a) Fiber content. (b) Rubber powder content.

(a)

(b)
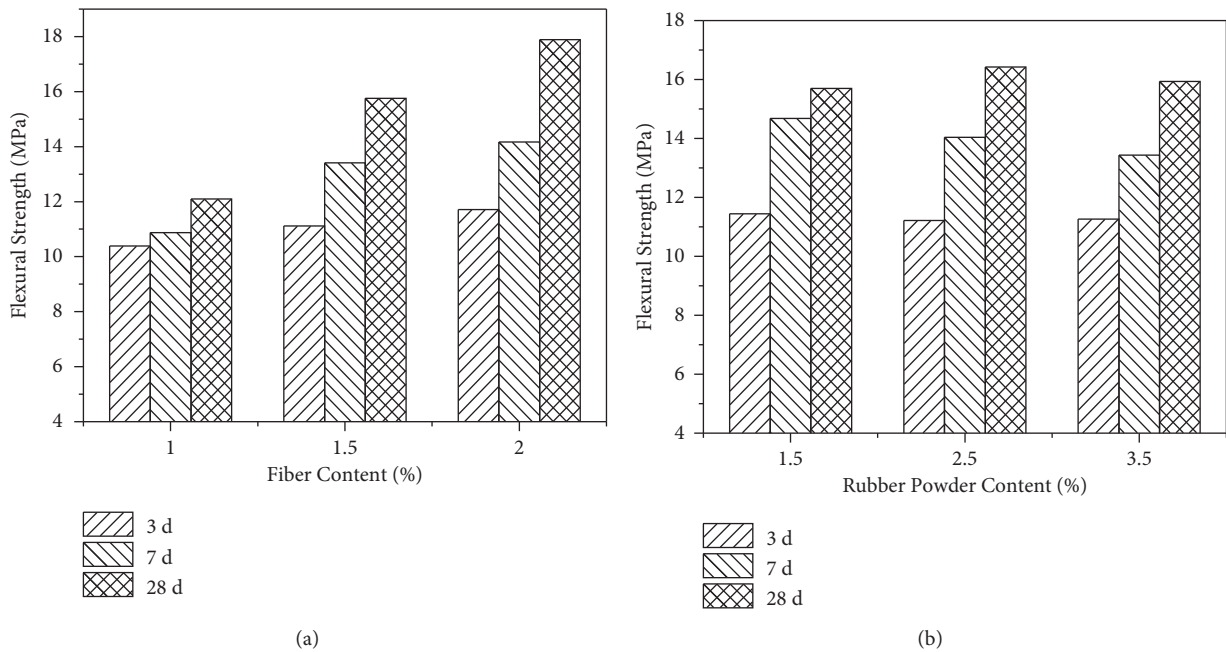
FIGURE 7: Flexural strength of mortars with different fiber and rubber powder contents when RH = 70%. (a) Fiber content. (b) Rubber powder content.

prepared at 70% humidity, indicating that the humidity can improve the drying shrinkage performance of the GRC. At 40% relative humidity, the drying shrinkage rate of the GRC with the expansion agent is significantly lower than that of the GRC without the expansion agent. After 15 days, the drying shrinkage rate of the GRC with the expansion agent is lower than that of the GRC cured at 70% humidity. The components have a certain hydration and expansion

capacity in the U-type expansion agent. Adding the expansion agent can prevent the early-age shrinkage strain and reduce the risk of early-age cracks [38]. At the same time, the drying shrinkage of the mortar can be inhibited by increasing the curing humidity.

In summary, (1) the incorporation of 3 mm alkali-resistant glass fibers can help reduce the drying shrinkage of the mortar to a certain extent and significantly increase its

(a)

(b)
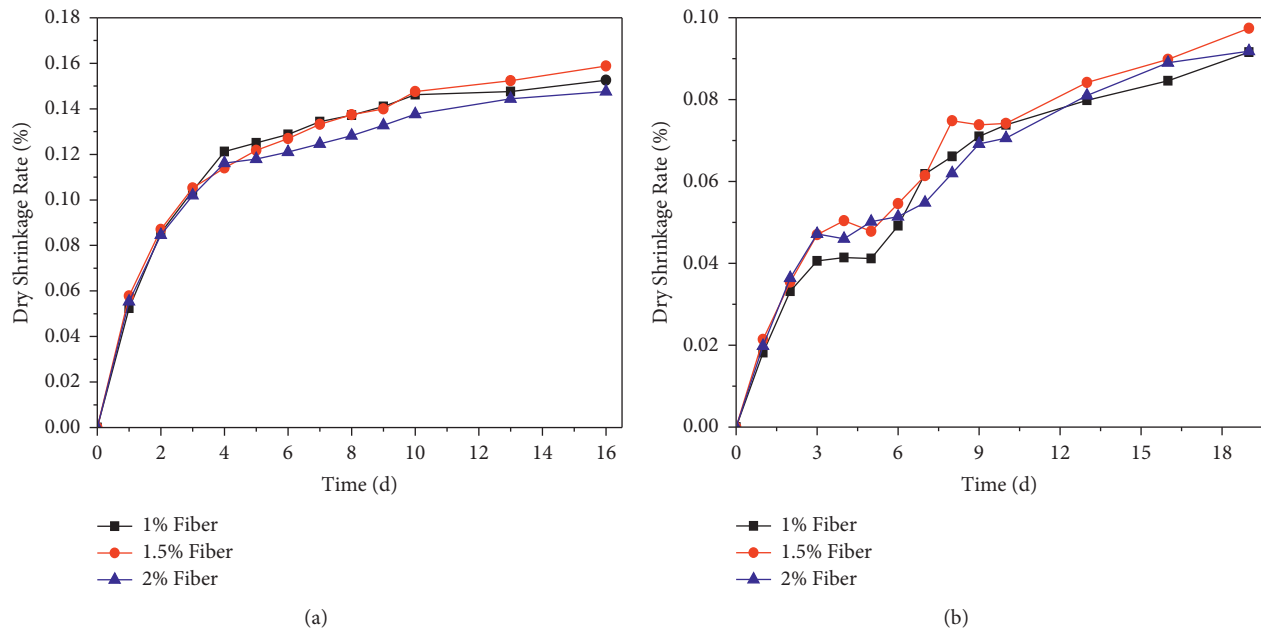
Figure 8: Drying shrinkage rate of mortar with different fiber contents under (a) RH = 40% and (b) RH = 70%.

flexural strength, thereby improving the crack resistance of the matrix. The greater the amount of fiber, the more evident the effect. (2) In the blending amount range of 0–3.5% dispersible rubber powder, with the blending of the dispersible rubber powder, the flexural strength of the mortar first increases and then decreases. It can improve its crack resistance. However, the incorporation of the rubber powder will reduce the flexural strength and increase the capillary tension because of the introduction of more pores, which aggravate the drying shrinkage of the mortar. (3) UEA can prevent harmful cracks in the concrete due to shrinkage stress and improve the compactness and impermeability. The results showed that cement mortar with 8% UEA can exhibit a certain degree of microexpansion performance.

3.2. Drying Shrinkage Performance of GRC-PLC Composite Panels.

The shrinkage of a GRC-PLC composite panel includes temperature shrinkage, drying shrinkage, plastic shrinkage, carbonization shrinkage, and autogenous shrinkage. Faez Sayahi et al. [39] believe that cement shrinkage and deformation is the main cause of cracking. Therefore, the composite panel cracks can be reflected by monitoring the shrinkage strain of the panel.

T0 was a GRC panel without fiber, which was completed on June 1, 2019. T0 was not composite with other materials, so it can shrinkage freely. However, after three months of T0, there were cracks in the middle of the plate (Figure 11(a)). This phenomenon shows that the different position of the panel has different shrinkage strain, resulting in different shrinkage stress. At the same time, according to the distribution of cracks in the panel, the middle of the panel was free to shrinkage and deform, resulting in the shrinkage stress exceeded the ultimate tensile strength of GRC materials, and producing cracks

finally. Therefore, it was reasonable to place the strain gauge in the middle of the panels (Figure 11(b)). And T1–T6 were not found cracks in the monitoring period, which can indicate that the new GRC-PLC composite panel met the resistance requirements.

The temperature and humidity changes affect the shrinkage of the composite panel, and these changes were recorded during the test monitoring period. Figure 12 shows that in the first three months, the temperature drops from summer to winter, and the temperature in winter stabilizes at approximately 5°C for the next two months and then shows a rising trend toward spring and summer. For an entire year, the indoor temperature and humidity were recorded in the morning, noon, and evening, and the average value was used to draw the temperature and humidity curve charts. Due to the change of the actual application environment of the panels, the monitoring time of the panels was set as one year to improve the integrity of the experiment.

3.2.1. Dry Shrinkage Properties of Pure GRC and Pure PLC Specimens.

Table 6 lists the maximum shrinkage strains of the six specimens based on monitoring data obtained experimentally.

T1 and T2 represent pure PLC and pure GRC specimens, respectively, which can be used as the test basis for comparison. The shrinkage strains of the other specimens can be referred from the analysis of the basis specimen. Figure 13 shows the shrinkage strain curves of the T1 and T2 specimens with time. The figure shows that the hydration reaction is intense at the beginning of the test and that the strain of the T1 specimen gradually increases with time. At this time, the lightweight concrete is stretched because of expansion. Later, as the
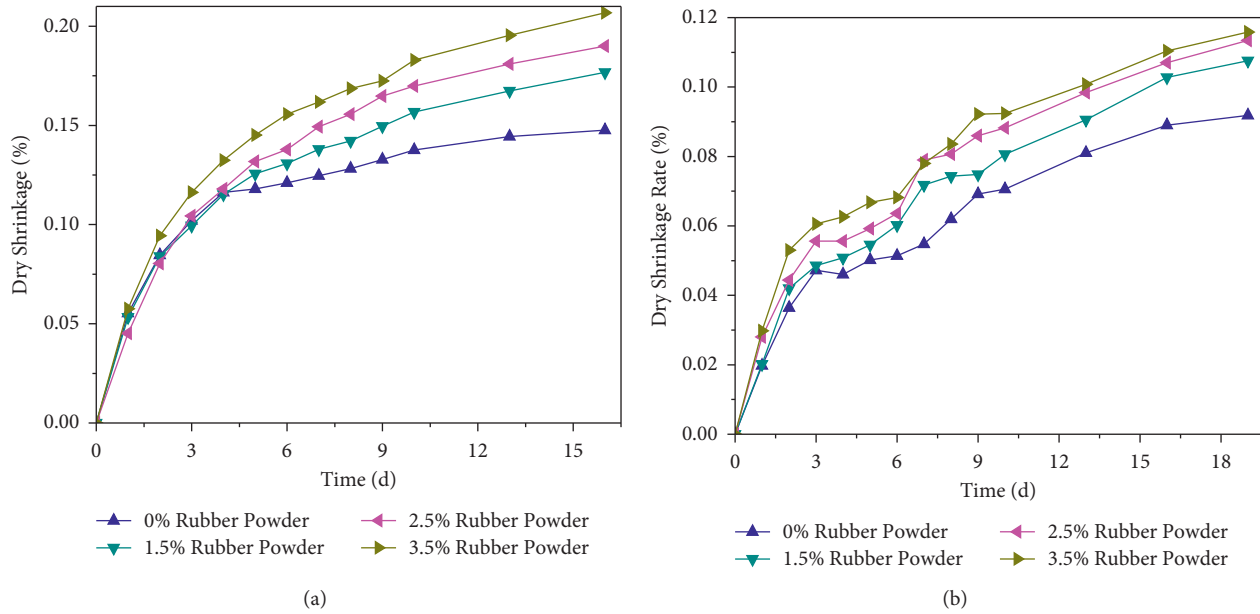
FIGURE 9: Drying shrinkage rates of mortar with different rubber powder contents under (a) RH = 40% and (b) RH = 70%.
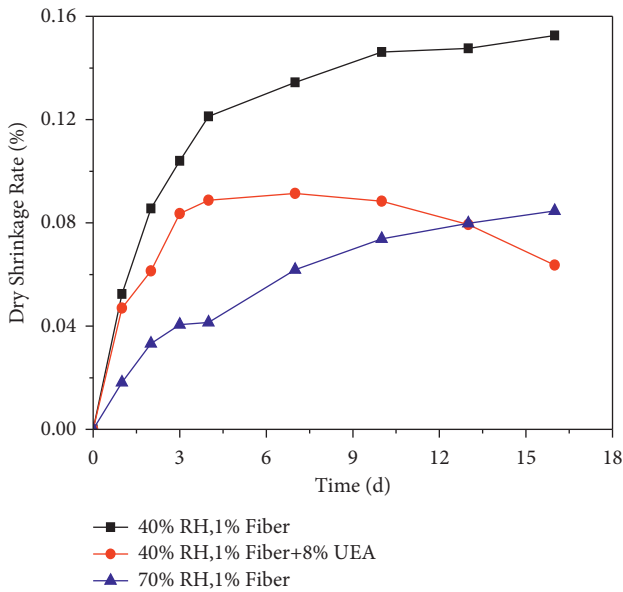
FIGURE 10: Effect of expansion agent content on drying shrinkage performance of GRC prepared under different humidity environments.

hydration reaction gradually weakens and the temperature changes, the strain of the T1 specimen changes from positive to negative, indicating that it is in a state of contraction. In the early stage of the experiment, the hydration reaction of the T2 specimen is intense, which stretched the T2 specimen because of expansion. The strain in the T2 specimen shows a wave-type fluctuation with time because of the influences of temperature and humidity in the later period. Compared with that shown in Figure 12, the drying shrinkage of GRC material is significantly affected by the temperature and humidity, resulting in a fluctuation in the strain of the T2 specimen.

These two panels were used as the basic comparison panel for the experiment. Rafał Stanisław and Barbara [40] believe that the shrinkage of lightweight concrete was not greater than that calculated for normal weight concrete of a similar strength class. At the same time, it can be seen from Figure 13 that PLC and GRC have different shrinkage performances. The shrinkage strain of PLC is smaller than that of GRC. After the composite, there was a strain difference between the two materials. Therefore, the influence of different connection modes of PLC and GRC on shrinkage performance was studied.

3.2.2. Surface and Internal Dry Shrinkage Performance of T3–T6 Composite Panels. Figure 14 shows the variation curves of the surface and internal shrinkage strains with the time of specimens T3–T6. At an early age, hydration of cement leads to a reduction in volume that induces autogenous shrinkage. Because autogenous shrinkage occurs in cement mortar, the performance of thermal expansion was different between cement motor and aggregates. The internal shrinkage stress was incompatible, and it cannot reach the self-equilibrated state of stress [41]. By comparison, the shrinkage strain of these specimens shows an increasing trend over time because of the hydration reaction; the specimens begin to expand in tension, and the strain gradually increases at the beginning of the experiment. Later, as the hydration reaction gradually weakens, the GRC materials and PLC begin to shrink, and the strain on the surface and inside of the specimen changes from positive to negative. In addition, as shown in Figure 14, the shrinkage deformation trend of GRC layer and PLC layer is basically the same, suggesting that the shrinkage deformation between GRC

(a)   (b)
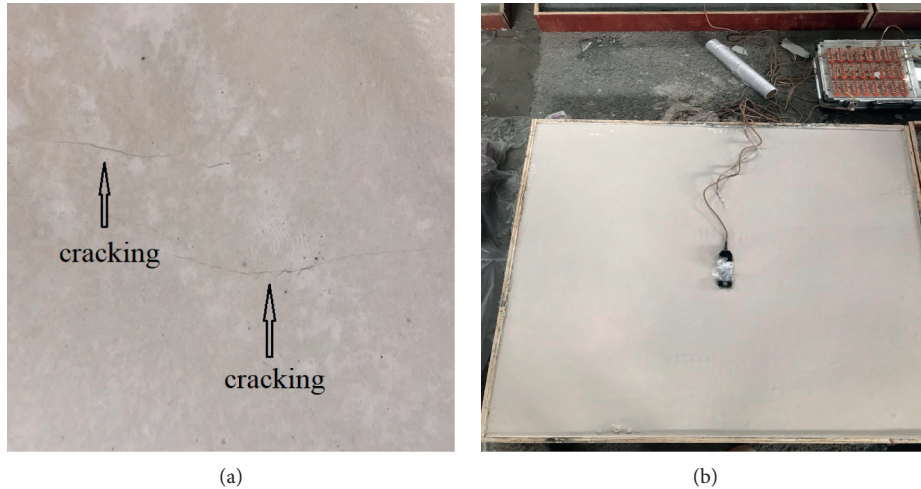
FIGURE 11: Difference of panels. (a) T0. (b) T2.

(a)

(b)
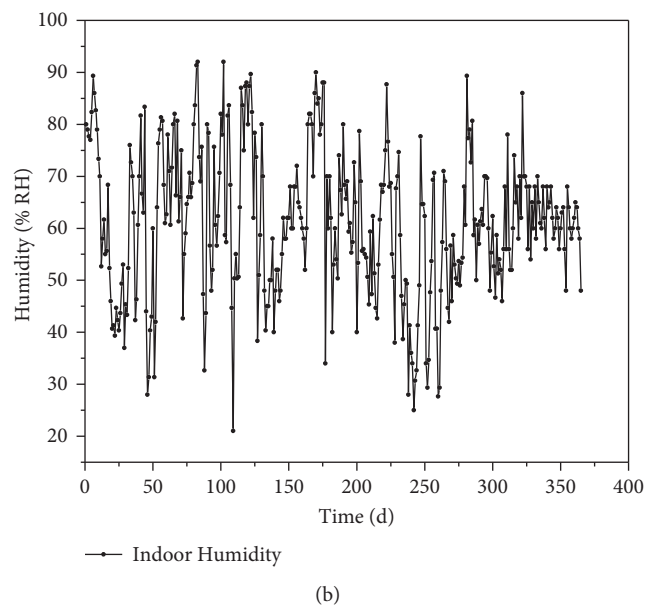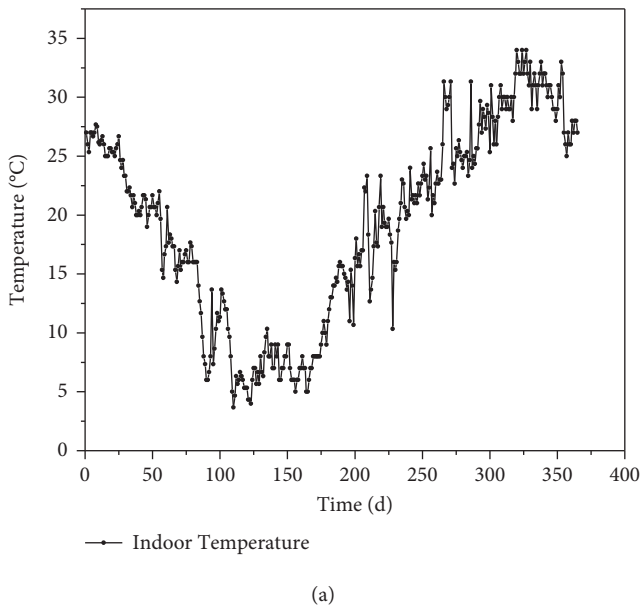
FIGURE 12: (a) Indoor temperature and (b) indoor humidity change curves with time.

layer and PLC layer is coordinated. Compared with T3 and T5, the deformation coordination of T4 and T6 is better, which is beneficial to the overall crack resistance of GRC-PLC composite panel.

3.2.3. Influence of GRC Material Thickness on Shrinkage Performance of Composite Panel. To explore the influence of GRC thickness on the shrinkage performance of the composite panels, GRC specimens with two different thicknesses were designed for the experiment: 10 mm (T3) and 15 mm (T4). Torres et al. [42] believe that the amount of cement used affects the aggregate coating thickness, which has an effect on the porosity and other mechanical properties of the concrete. Because the thermal expansion performance of GRC and PLC materials was different. Therefore, GRC

thickness will affect the shrinkage performance of composite wall panel.

Figure 15 shows a comparison between the pure GRC material and GRC composite panel of different thicknesses in terms of their surface shrinkage performance. At the beginning of the test, the shrinkage strains of the specimens T2, T3, and T4 increase because of the hydration reaction. At this time, the specimen is in a state of expansion and tension. Later, the hydration reaction weakens, the specimen is in a compression state, and the shrinkage strain tends to stabilize. The strain value of the T2 specimen shows a wave-like fluctuation after 28 days, and the change trends in the T3 and T4 specimens are different, indicating that the GRC material thickness has a certain degree of influence on the surface shrinkage properties of the composite panels. From the data listed in Table 6, the maximum shrinkage strain of the T3

TABLE 6: Maximum shrinkage strain values of various specimens.

Category	Surface shrinkage strain value (GRC)	Internal shrinkage strain value (PLC)
T1	—	908.64×10^{-6}
T2	1594.30×10^{-6}	—
T3	703.91×10^{-6}	914.76×10^{-6}
T4	731.48×10^{-6}	897.20×10^{-6}
T5	791.74×10^{-6}	684.33×10^{-6}
T6	780.23×10^{-6}	773.57×10^{-6}
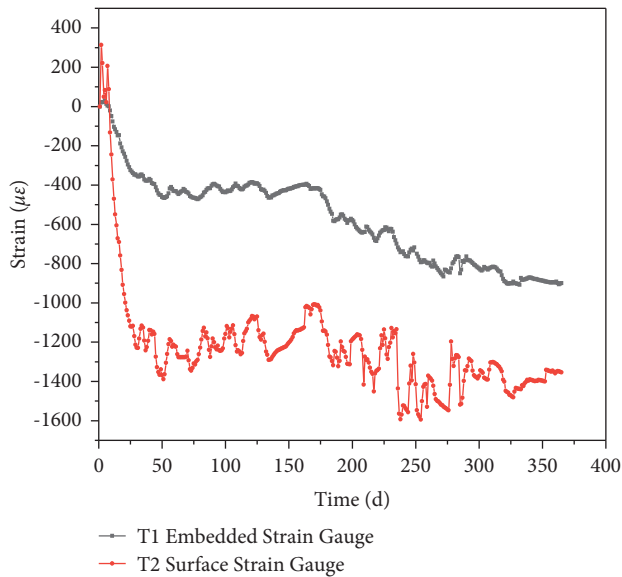
FIGURE 13: Strain curves of T1 and T2 specimens with time.

specimen is reduced by 56% compared with that of the T2 specimen, and the maximum shrinkage strain of the T4 specimen is reduced by 54% compared with that of the T2 specimen.

Figure 16 shows a comparison diagram of the internal shrinkage performance of pure lightweight concrete materials and GRC composite panels of different thicknesses. At the beginning of the test, because of the hydration reaction, the specimen is in the state of expansion and tension, and the hydration reaction is weakened in the later stage; the specimen is in a state of compression, and the shrinkage strain tends to be stable. The figure shows that the internal shrinkage strains of specimens T1, T3, and T4 exhibit a downward trend in the later stage, and the shrinkage strain of the T4 specimen is lower than those of specimens T1 and T3. From the data listed in Table 6, the maximum shrinkage strain of the T3 specimen is increased by 0.7% compared with that of the T1 specimen, and the maximum shrinkage strain of the T4 specimen is reduced by 1.3% compared with that of the T1 specimen.

Compared with simple GRC panel, the shrinkage deformation of the composite GRC layer was obviously small (as shown in Figure 15). This phenomenon shows that the PLC layer obstructs the shrinkage of GRC layer, thus generating tensile stress in the GRC layer. And until the end of the experiment, the tensile stress always existed, but the GRC layer did not crack. This indicates that the shrinkage stress of the GRC layer is less than the tensile strength.

In the early stage of the experiment, the shrinkage deformation of the composite PLC layer was smaller than that of the simple PLC board. However, near the end of the experiment, the deformation is basically the same (Figure 16). This indicates that in the early stage of the experiment, there was a shrinkage stress in the PLC layer, but with the passage of time, the shrinkage stress was gradually reduced. To sum up, after GRC and PLC are compounded, the crack resistance demand of GRC layer is higher.

In addition, the shrinkage deformation curves of GRC layers with different thicknesses are basically the same (as shown in Figure 15). In terms of the production process, the GRC layer of 15 mm thickness is easier to ensure that the forming quality is that of 10 mm thickness.

3.2.4. Influence of Connection Method of Composite Interface on Shrinkage Performance of Composite Panel. Three types of composite interface connection methods (smooth, rough, and laying steel mesh) were set up in the experiment. By studying the different connection methods of the composite panels, the best connection methods for the two materials were selected. Figure 17 shows the surface shrinkage strain curves with time of the T2, T4, T5, and T6 specimens. The time–strain curves of the T4, T5, and T6 specimens show linear changes in the late experimental period, though the variation ranges of the surface shrinkage strain differ. The surface shrinkage strain of the T5 specimen is lower than those of the T4 and T6 specimens, indicating that the different connection modes of the composite interface have a significant effect on the surface shrinkage performance of the composite panel. From Table 6, it can found that the maximum surface shrinkage strains of the T2, T4, T5, and T6 specimens are 1594.30×10^{-6}, 731.48×10^{-6}, 791.74×10^{-6}, and 780.23×10^{-6}, respectively. The maximum shrinkage strains of the T4, T5, and T6 specimens decrease by more than 50% compared with that of the T2 specimen. Among them, the surface shrinkage strain of the T5 specimen decreases the most, reaching 62%. Compared with that of T5, the time–strain curves of T4 and T6 specimens fit the curve of the T1 specimen more closely. Chen et al. [43] studied the effect of different interface connection modes on the drying shrinkage of GRC and concrete composite materials. It can be concluded that different interface connection modes have different effects on GRC drying shrinkage, while smooth connection can effectively inhibit the generation of cracks.

Figure 18 shows the internal shrinkage strain curves of the T1, T4, T5, and T6 specimens with time. Clearly, the four curves exhibit the same trend, and the variation ranges of the
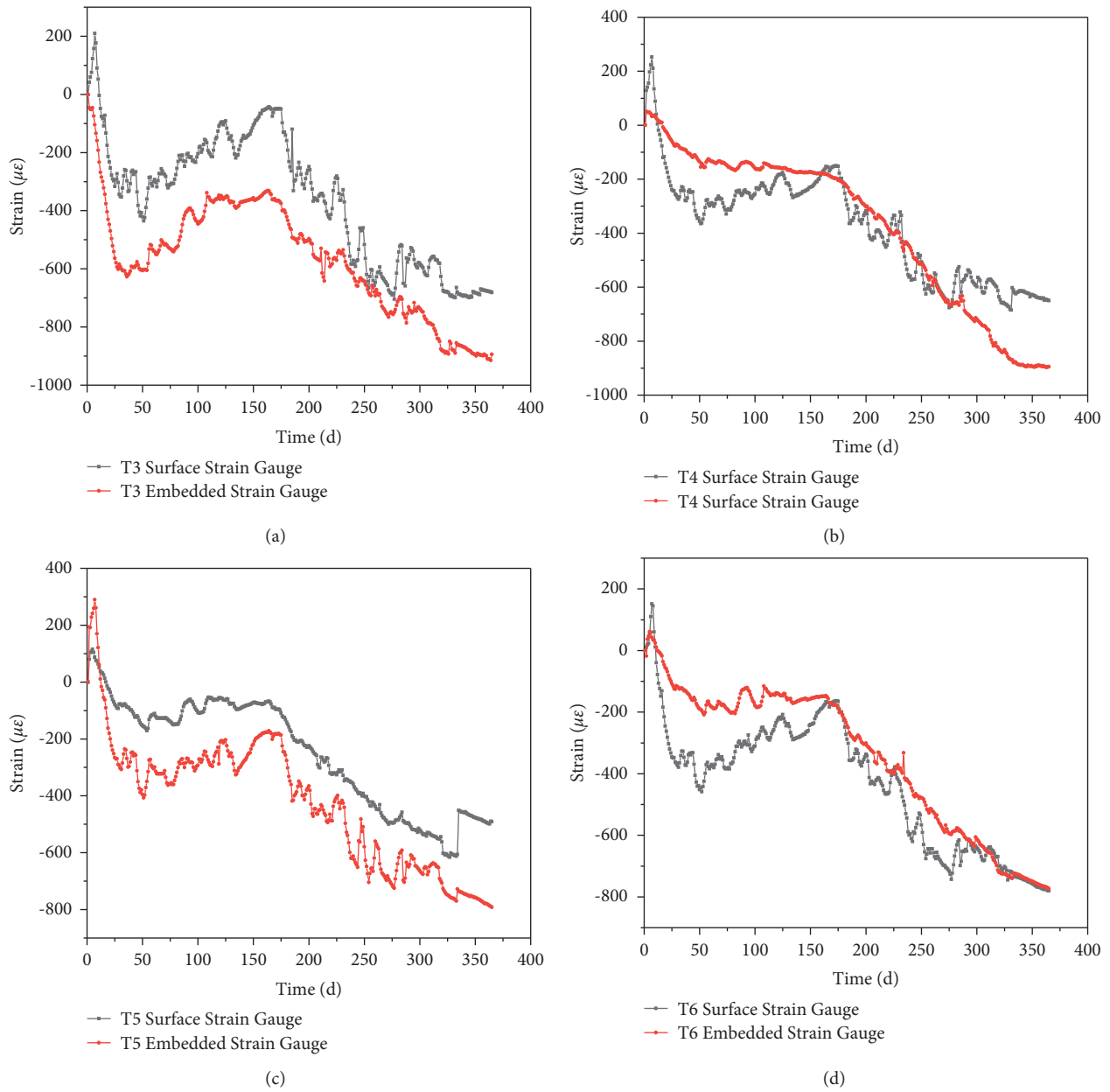
FIGURE 14: Curve of specimen shrinkage strain with time. (a) T3 specimen. (b) T4 specimen. (c) T5 specimen. (d) T6 specimen.

time–strain curves of the T4, T5, and T6 specimens are the same. The shrinkage strain values of the T4 and T6 specimens are greater than the strain value of the T5 specimen in the early stage of the experiment. This is mainly attributed to the rough connection affecting the connection between the GRC layer and the lightweight concrete layer. This shows that different connection modes of the composite interface have an impact on the internal shrinkage performance of the composite panel. From Table 6, it can found that the

maximum internal shrinkage strains of the T1, T4, T5, and T6 specimens are 908.64×10^{-6}, 897.20×10^{-6}, 684.33×10^{-6}, and 773.57×10^{-6}, respectively. The graph shows that the maximum internal shrinkage strains of the T4, T5, and T6 specimens are lower than that of the T1 specimen. Among the three curves, the time–strain curve of the T4 specimen fits the curve of the T1 specimen more closely.

Compared with simple GRC panel, the shrinkage deformation of the composite GRC layer was obviously
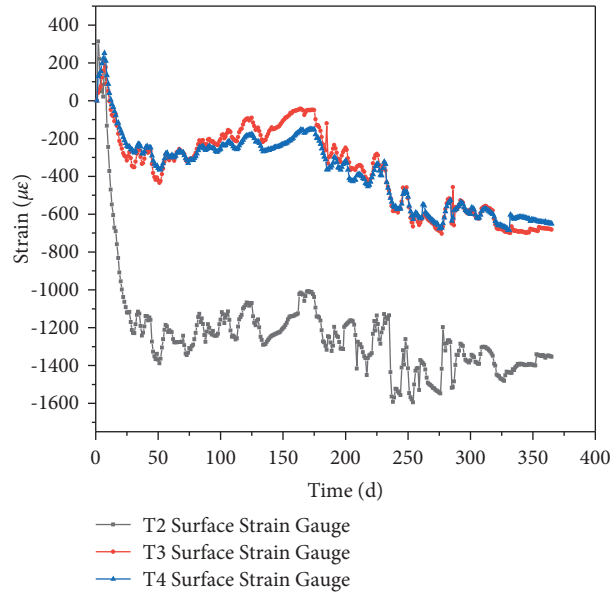
FIGURE 15: Surface shrinkage strain curves of T2, T3, and T4 specimens with time.
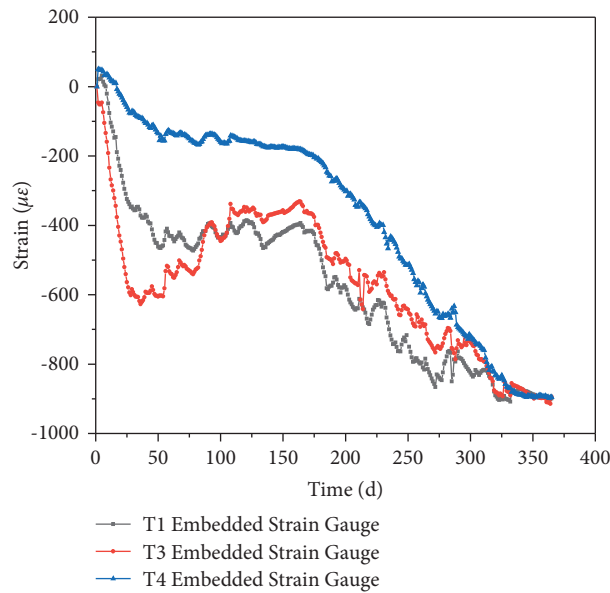
FIGURE 16: Internal shrinkage strain curves of T1, T3, and T4 specimens with time.

small, as shown in Figure 17. The shrinkage deformation of smooth connection was almost the same as that of steel mesh connection and was larger than that of rough connection. This implies that the shrinkage stress in the composite GRC layer was smaller when the smooth connection and the steel mesh connection are used compared with the rough connection. Near the end of the experiment, the shrinkage deformation of smooth connection is closer to that of T1 panel, which suggests that compared with rough connection and steel mesh connection, the shrinkage stress in PLC layer is smaller when smooth connection was used. As far as the production process is concerned, the use of smooth connection is more efficient than the use of steel mesh connection. Therefore, the use of smooth connection is more reasonable.
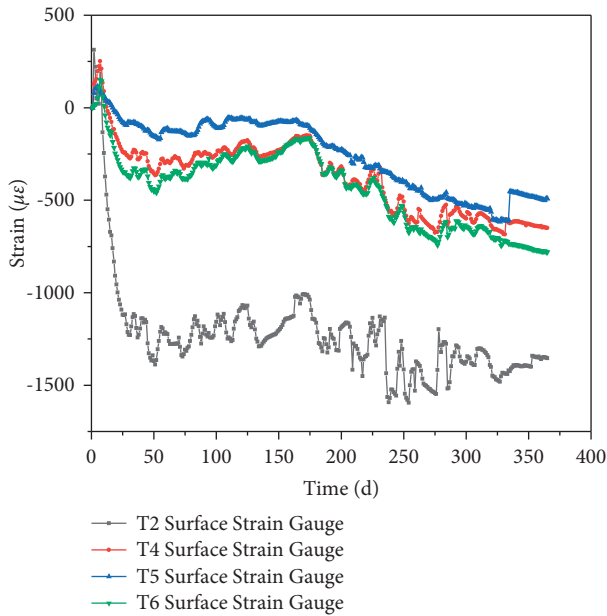
FIGURE 17: Surface shrinkage strain curves of T2, T4, T5, and T6 specimens with time.
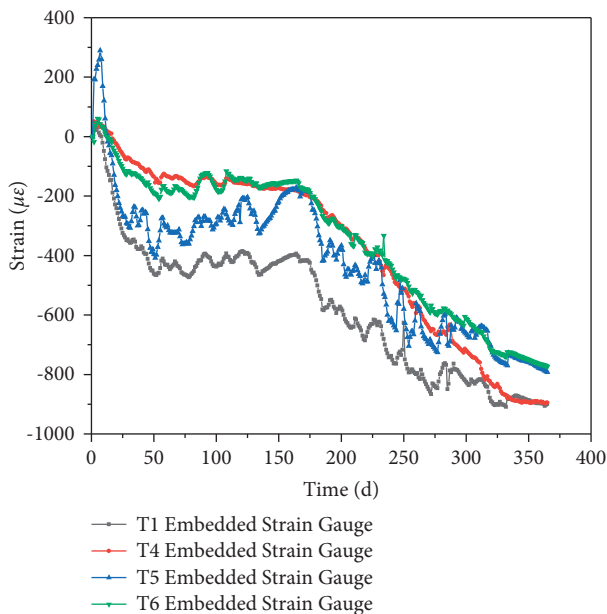
FIGURE 18: Internal shrinkage strain curves of T1, T4, T5, and T6 specimens with time.

4. Conclusions

This research investigated the crack resistance of the GRC-PLC-integrated composite panels, through reducing material shrinkage, improving the tensile strength of cement-based materials, and determining the most effective connection method. During the experiment of about one year, the composite GRC layer did not crack, and thehe following conclusions can be drawn:

(1) According to the monitoring results of T0 panel, the cracks were usually produced in the middle of the panel, where the shrinkage stress was the greatest. Therefore, cracks tend to occur in the middle of the panel.

(2) In GRC material formula, fiber, rubber powder, and expansion agent are the three main components to prevent GRC material cracking. Through the experiment of bending and shrinkage, the better anticrack formula of GRC was obtained.

(3) The shrinkage deformation of the composite GRC layer is not sensitive to the change in thickness, but it is sensitive to the connection mode of the PLC layer. In terms of crack resistance and production process, 15 mm thickness of GRC layer and smooth connection with PLC layer are more conducive to the application of GRC-PLC composite panel.

GRC-PLC-integrated composite panel is a new type of prefabricated wall that can greatly reduce pollution, shortens the construction period, and improves the construction efficiency. The researches in this paper provide an experimental basis for the large-scale application of the panel.

Data Availability

All data generated or used during the study are available within the article.

Conflicts of Interest

The authors declare no conflicts of interest.

Acknowledgments

References

[1] H. M. Liu, C. Q. Wu, Y. B. Xu, and A. D. Zhu, "Research progress of composite thermal insulation wall in hot summer and cold winter zone of China," *Advanced Materials Research*, vol. 919-921, pp. 1725–1729, 2014.

[2] B. Cheng, J. Li, V. W. Y. Tam, M. Yang, and D. Chen, "A BIM-LCA approach for estimating the greenhouse gas emissions of large-scale public buildings: a case study," *Sustainability*, vol. 12, no. 2, p. 685, 2020.

[3] Iso 22966: 2009, *Execution of concrete Structures*, International Standard Organization, Beijing, China, 2009.

[4] E. Antoine, T. W. Naaman and G. Hauser, "Influence of different fibers on plastic shrinkage cracking of concrete," *ACI Materials Journal*, vol. 102, no. 1, pp. 49–58, 2005.

[5] F. Pelisser, A. B. d. S. S. Neto, H. L. L. Rovere, and R. C. d. A. Pinto, "Effect of the addition of synthetic fibers to concrete thin slabs on plastic shrinkage cracking,"

Construction and Building Materials, vol. 24, no. 11, pp. 2171–2176, 2010.

[6] P. S. Song, S. Hwang, and B. C. Sheu, "Strength properties of nylon- and polypropylene-fiber-reinforced concretes," *Cement and Concrete Research*, vol. 35, no. 8, pp. 1546–1550, 2005.

[7] S. Kakooei, H. M. Akil, M. Jamshidi, and J. Rouhi, "The effects of polypropylene fibers on the properties of reinforced concrete structures," *Construction and Building Materials*, vol. 27, no. 1, pp. 73–77, 2012.

[8] A. S. El-Dieb and M. M. Reda Taha, "Flow characteristics and acceptance criteria of fiber-reinforced self-compacted concrete (FR-SCC)," *Construction and Building Materials*, vol. 27, no. 1, pp. 585–596, 2012.

[9] Q. H. Li, J. J. Zhao, Q. Y. Li, J. W. Gao, and Y. J. Wu, "Influence of different dimensions of glass fiber on GRC flexural performance," *Journal of Building Materials*, vol. 24, no. 3, pp. 1–10, 2020.

[10] C. Cheng, J. He, J. Zhang, and Y. Yang, "Study on the time-dependent mechanical properties of glass fiber reinforced cement (GRC) with fly ash or slag," *Construction and Building Materials*, vol. 217, pp. 128–136, 2019.

[11] J. Payá, M. Bonilla, M. V. Borrachero, J. Monzó, E. Peris-Mora, and L. F. Lalinde, "Reusing fly ash in glass fibre reinforced cement: a new generation of high-quality GRC composites," *Waste Management*, vol. 27, no. 10, pp. 1416–1421, 2007.

[12] Y. M. Wang, Y. Z. Tang, and K. W. Liu, "Effect of fiber and rubber powder on mechanics and crack resistance of cement mortar," *Bulletin of the Chinese Ceramic Society*, vol. 37, no. 9, pp. 2275–2781, 2018.

[13] V. S. Gopalaratnam and R. Gettu, "On the characterization of flexural toughness in fiber reinforced concretes," *Cement and Concrete Composites*, vol. 17, no. 3, pp. 239–254, 1995.

[14] A. Enfedaque, D. Cendón, F. Gálvez, and V. Sánchez-Gálvez, "Analysis of glass fiber reinforced cement (GRC) fracture surfaces," *Construction and Building Materials*, vol. 24, no. 7, pp. 1302–1308, 2010.

[15] A. Enfedaque, J. C. Gálvez, and F. Suárez, "Analysis of fracture tests of glass fibre reinforced cement (GRC) using digital image correlation," *Construction and Building Materials*, vol. 75, pp. 472–487, 2015.

[16] P. R. d. Matos, M. Foiato, and L. R. Prudêncio, "Ecological, fresh state and long-term mechanical properties of high-volume fly ash high-performance self-compacting concrete," *Construction and Building Materials*, vol. 203, pp. 282–293, 2019.

[17] F. A. Mirza and P. Soroushian, "Effects of alkali-resistant glass fiber reinforcement on crack and temperature resistance of lightweight concrete," *Cement and Concrete Composites*, vol. 24, no. 2, pp. 223–227, 2002.

[18] M. M. Reda Taha, A. S. El-Dieb, M. A. Abd El-Wahab, and M. E. Abdel-Hameed, "Mechanical, fracture, and micro-structural investigations of rubber concrete," *Journal of Materials in Civil Engineering*, vol. 20, no. 10, pp. 640–649, 2008.

[19] Z. T. Wu, Y. S. Zhang, and N. D. Liu, "Study on shrinkage property of glass fiber reinforced cement base material," *Bulletin of the Chinese Ceramic Society*, vol. 38, no. 8, pp. 2570–2577, 2019.

[20] P. Van Itterbeeck, P. Purnell, H. Cuypers, T. Tysmans, J. Orlowsky, and J. Wastiels, "Durability models for GRC: uncertainties on strength predictions," *Plastics, Rubber and Composites*, vol. 41, no. 2, pp. 77–87, 2012.

[21] P. V. Itterbeeck, P. Purnell, H. Cuypers, and J. Wastiels, "Study of strength durability models for GRC: theoretical overview," *Composites Part A: Applied Science and Manufacturing*, vol. 40, no. 12, pp. 2020–2030, 2009.

[22] J. N. Eiras, T. Kundu, M. Bonilla, and J. Payá, "Nondestructive monitoring of ageing of alkali resistant glass fiber reinforced cement (GRC)," *Journal of Nondestructive Evaluation*, vol. 32, no. 3, pp. 300–314, 2013.

[23] P. Purnell and J. Beddows, "Durability and simulated ageing of new matrix glass fibre reinforced concrete," *Cement and Concrete Composites*, vol. 27, no. 9–10, pp. 875–884, 2005.

[24] J. R. Correia, J. Ferreira, and F. A. Branco, "A rehabilitation study of sandwich GRC facade panels," *Construction and Building Materials*, vol. 20, no. 8, pp. 554–561, 2006.

[25] D. D. Theodorakopoulos, "Shrinkage behaviour of GRC thin sheets," *Cement and Concrete Composites*, vol. 17, no. 3, pp. 229–238, 1995.

[26] C. M. Cheng, S. L. Hong, Y. F. Zhang, and J. He, "Effect of expanded polystyrene on the flexural behavior of lightweight glass fiber reinforced cement," *Construction and Building Materials*, vol. 265, Article ID 120328, 2020.

[27] G. W. Leong, K. H. Mo, Z. P. Loh, and Z. Ibrahim, "Mechanical properties and drying shrinkage of lightweight cementitious composite incorporating perlite microspheres and polypropylene fibers," *Construction and Building Materials*, vol. 246, Article ID 118410, 2020.

[28] R. Chylík, J. Fládr, P. Bílý, T. Trtík, and L. Vráblík, "An analysis of the applicability of existing shrinkage prediction models to concretes containing steel fibres or crumb rubber," *Journal of Building Engineering*, vol. 24, Article ID 100729, 2019.

[29] J. Ji, H. X. Wang, Q. Wang, Z. Suo, and Z. K. Yuan, "Effect of modified waste rubber powder on properties of cement mortar," *Journal of Building Materials*, pp. 1–17, 2020.

[30] B. Chen, J. T. Ding, Y. B. Cai, Y. Bai, and W. X. Zhang, "Effect of internal curing and expansive agent on comprehensive crack resistance of concrete," *Bulletin of the Chinese Ceramic Society*, vol. 44, no. 2, pp. 189–195, 2016.

[31] J. J. Guo, S. W. Zhang, T. Guo, and P. Zhang, "Effects of UEA and MgO expansive agents on fracture properties of concrete," *Construction and Building Materials*, vol. 263, no. 2, Article ID 120245, 2020.

[32] Iso 679: 2009, *Cement—Test Methods—Determination of Strength*, International Standard Organization, Beijing, China, 2009.

[33] A. Ei-Kariem and S. Shoeib, "Efficiency of discrete glass fiber reinforced cement mortar in compression," *Advanced Materials Research*, vol. 255-260, pp. 3137–3141, 2011.

[34] L. G. Yu, Q. J. Yu, and F. Liu, "Research progress on application of waste rubber powder in mortar concrete," *Bulletin of the Chinese Ceramic Society*, vol. 26, no. 6, pp. 1148–1152, 2007.

[35] R. V. Ralegaonkar, P. B. Aswath, and A. Abolmaali, "Design investigations of basalt-fibre-reinforced mortar," *Proceedings of the Institution of Civil Engineers—Construction Materials*, vol. 172, no. 6, pp. 296–304, 2019.

[36] Gb/T 29417-2012, *Standard Test Methods for Drying Shrinkage and Cracking Possibility of Cement Mortar and concrete*, National Institute of Standards of the People's Republic of China, Beijing, China, 2012.

[37] L. H. Zhang, J. Z. Liu, Z. Q. Yang, D. G. Xu, and L. Li, "Influence and mechanism of PP fiber with different cross section shape on plastic cracking resistance of mortar,"

Journal of Southeast University (Natural Science Edition), vol. 46, no. 1, pp. 160–164, 2016.

[38] P. X. Wang, "Effect of the expansion agent on early-age autogenous shrinkage stress of concrete," *Advanced Materials Research*, vol. 838-841, pp. 564–568, 2013.

[39] F. Sayahi, M. Emborg, H. Hedlund, and A. Cwirzen, "Plastic shrinkage cracking of self-compacting concrete: influence of capillary pressure and dormant period," *Nordic Concrete Research*, vol. 60, no. 1, pp. 67–88, 2019.

[40] S. Rafał Stanisław and Ł. Barbara, "Experimental evaluation of shrinkage, creep and prestress losses in lightweight Aggregate concrete with sintered fly ash," *Materials*, vol. 14, no. 14, p. 3895, 2021.

[41] M. Briffaut, F. Benboudjema, C. Laborderie, and J.-M. Torrenti, "Creep consideration effect on meso-scale modeling of concrete hydration process and consequences on the mechanical behavior," *Journal of Engineering Mechanics*, vol. 139, no. 12, pp. 1808–1817, 2013.

[42] A. Torres, J. Hu, and A. Ramos, "The effect of the cementitious paste thickness on the performance of pervious concrete," *Construction and Building Materials*, vol. 95, pp. 850–859, 2015.

[43] D. Chen, P. K. Li, B. Q. Cheng, H. Chen, Q. Wang, and B. Zhao, "Crack resistance of insulated GRC-PC integrated composite wall panels under different environments: an experimental study," *Crystals*, vol. 11, no. 7, 2021.

Research Article

Initial Parameters Affecting the Multilayer Doubly Curved Concrete Shell Roof

Thi My Dung Do [iD],[1] **Thanh Quang Khai Lam** [iD],[1] **Thi Thu Nga Nguyen** [iD],[2]
Van Thuc Ngo [iD],[1] **Hoang Hung Vu,**[3] **Trong Chuc Nguyen** [iD],[4] **and Van Duan Doan**[5]

[1]*Mien Tay Construction University, 20B Pho Co Dieu Street, Vinh Long, Vietnam*
[2]*University of Transport Technology, 54 Trieu Khuc Street, Hanoi, Vietnam*
[3]*Thuy Loi University, 175 Tay Son Street, Hanoi, Vietnam*
[4]*Le Quy Don Technical University, 236 Hoang Quoc Viet Street, Hanoi, Vietnam*
[5]*Vietnam Maritime University, 484 Lach Tray Street, Hai Phong, Vietnam*

Correspondence should be addressed to Thanh Quang Khai Lam; lamthanhquangkhai@gmail.com

Received 25 May 2021; Accepted 8 August 2021; Published 26 August 2021

Academic Editor: Kim Hung Mo

Doubly curved shell roof structures have been widely studied and applied in civil buildings, because of their compressive capacity. As a spatial structure, it should increase the space, reduce the thickness of the shell, and create the architecture for the building. In particular, reinforcement is needed to repair the shell surface, forming the multilayer curved shell roof structures. In this multilayer curved shell roof, it is necessary to investigate the influence of thickness of layers, the influence of the location of the steel fibres concrete layer, and the influence of steel fibres content contained in concrete on the state of stress and strain and build relationships, load-vertical displacement and stress in the x and y directions of the shell in the investigated cases. So, this paper presents an ANSYS numerical simulation study related to the state of stress and strain in double-layer doubly curved concrete shell roof with the initial parameters being changed such as the thickness of the layers, the location of the steel fibres concrete layer in the structure (the steel fibres concrete layer that is placed above and below the normal concrete layer), and the steel fibres content contained in concrete shell with the size of 3000 × 3000 mm, which is simulated by ANSYS after being experimentally conducted on this curved shell roof; the results of experimental and simulation study are verified by each other. Research results show that the thickness of the steel fibres concrete layer is placed below the normal concrete layer, the percentage of steel fibres contained in the concrete is 2%, and the bearing capacity of the curved shell is optimal.

1. Introduction

Vlasov, who laid the groundwork in his research on shell types, proposed the shell theory, which is composed of thin shells. With this shell theory, Vlasov proved that these shells are mainly compressive or tensile, and the bending moment in the shell is very small and can be ignored in calculations. Vlasov [1] built a system of 2 equations with two stress and displacement (φ and w) functions with the load distributed over the shell surface.

Since then, plenty of shell studies have occurred, including shell analysis with the different curvature or seismic response of smart nanocomposite cylindrical shell, and using HDQ-Newmark methods in conveying fluid flow [2], cylindrical and spherical lattice shell [3, 4], the strain-stress state of concrete dome structure simulated by ANSYS [5], and doubly curved shells with square and rectangular plane was studied by the approximation method; this method is developed on the basis of finite difference method that studied and developed by Gabbasov. In the 1980s, the essence of this method was to solve general quadratic differential equations. To solve this general differential equation, Gabbasov used the meshing method and thereby established the relationship between the points; from there,

the results were converted from general differential equations to the system of linear equations for each point on the grid [6].

In addition, the shell structures have been studied by many authors by experimental method, finite element method [7, 8], by Sap2000 software [9], and by numerical simulation method, ANSYS, for umbrella shell in vibration analysis [10]; many authors have studied various parameters such as repairing and strengthening of elliptical paraboloid reinforced concrete shells [11], R-Funicularity [12], prediction of the buckling behavior of shell [13], funicular concrete shell foundation under ultimate loading [14], classical shell theory for instability analysis of concrete pipes [15], bearing capacity of the initial imperfect lattice shell [16], optimized high-performance concrete shells [17], stability of steel shell structures [18], including large scale shell [19], and investigation of the geometrically nonlinear behavior of thin-shell structures [20]. Through the analyzed studies, the studies analyzed the state of stress and strain and considered the parameters affecting the shells. However, these studies only studied single-layer shells.

According to research on curved shells, these shells are damaged during use, need to be repaired, or need to be waterproof, heat resistant, or strengthened for these shells to increase bearing capacity and increase the life of the buildings, so they are necessary to add one or more layers above or below the existing shell layer. Ambartsumyan [21] has also suggested the multilayer shell hypothesis. Many studies have been done on various types of shells such as cylindrical shells, spherical shells, doubly curved shells, and elliptical paraboloid shells using analytic methods, numerical methods, finite element methods, approximation methods, and other methods based on Ambartsumyan's laminated shell theory. Ambartsumyan assumed that layers were referred to equivalent layers according to their modulus of elasticity, such as the layerwise theory of laminated doubly curved shells [22], analysis of laminated doubly curved shells in both static and dynamic conditions [23], the bending and free vibration analysis of laminated composite shells [24], multilayer shell element for shear walls in open sees [25], stress-strain state of three-layered shallow shells [26], and mesh-reinforced Sandwich concrete shell roof [27]. Many researches have used the multilayer shell element in the finite element (FE) model nonlinear analysis to approach nonlinear studies [28]. The multilayer shell structure is also an applicability analysis on the multilayer shell structure system in construction, to test the theoretical method with multilayer structures that have been tested by the above theoretical methods [29].

In analyzing the structures of multilayer doubly curved shell roofs, many studies have used analytical methods or numerical methods to solve these curved shell problems. However, with the use of these curved shells in civil buildings, the material of the shell must be analyzed. Currently, steel fibres concrete has the ability to increase bearing capacity and reduce cracks and has good impact resistance; in addition, steel fibres concrete can also work quite well when steel fibres concrete is located in the tension region. In the studies on these steel fibres concrete materials, many

studies have used them in flexural multilayer structures such as double-layer beams or three-layer beams. The performance of normal concrete and steel fibres concrete in these laminated beams is quite suitable when repairing damaged concrete beams. These studies have conducted experiments and simulated by ANSYS these multilayer flexural beams [30, 31]. However, there are other studies on steel fibres concrete materials with nanosilica that can also be applied in this doubly curved shell experiment and simulation [32, 33].

Recently, this multilayer doubly curved shell roof is further studied when analyzing the nonlinearity of steel fibres concrete materials and the change of steel fibres content in concrete by ANSYS. The study determined the state of stress and strain in the shell and the sliding ability between two different concrete layers in the shell [34]. However, the shell material must be investigated in both the experimental analysis and ANSYS simulation for the laminated doubly curved shells. Because shell's compressive capacity and reinforcement are needed to repair the shell surface, it is necessary to investigate the influence of the thickness of layers, the influence of the location of the steel fibres concrete layer, and the influence of the steel fibres content contained in concrete on the state of stress and strain and build relationships, load-vertical displacement and stress in the x and y directions of the shell in the investigated cases. So, this paper presents an ANSYS numerical simulation study related to the state of stress and strain of double-layer doubly curved concrete shell roof with the initial parameters being changed such as the thickness of the layers, location of the steel fibres concrete layer (the steel fibres concrete layer (SFCL) above and below the normal concrete layer (NCL)), and steel fibres content contained in concrete shell with the size of 3000×3000 mm, which is simulated by ANSYS after being experimentally conducted on this curved shell roof; the results of experimental and simulation study are verified by each other.

2. Materials and Methods

2.1. Vlasov Equations in Calculating the Shell Roof Structures. Vlasov [1] built a system of 2 equations with two stress and displacement (φ and w) functions with the load distributed over the shell surface (equation (1)):

$$\left.\begin{array}{l} \dfrac{\partial^4 \phi}{\partial x^4} + 2\dfrac{\partial^4 \phi}{\partial x^2 \partial y^2} + \dfrac{\partial^4 \phi}{\partial y^4} + Eh\left(k_1 \dfrac{\partial^2 w}{\partial x^2} + k_2 \dfrac{\partial^2 w}{\partial y^2}\right) = 0 \\[4mm] k_1 \dfrac{\partial^2 \phi}{\partial x^2} + k_2 \dfrac{\partial^2 \phi}{\partial y^2} - D\left(\dfrac{\partial^4 w}{\partial x^4} + 2\dfrac{\partial^4 w}{\partial x^2 \partial y^2} + \dfrac{\partial^4 w}{\partial y^4}\right) = -q(x, y) \end{array}\right\},$$

$$(1)$$

where h is the shell thickness, E is modulus of elasticity, k_1 and k_2 are main curvature in 2 directions, and D is the flexural stiffness of the shell.

With the above assumption, for doubly curved shell with rectangular plan, Ambartsumyan [21] has introduced a system of equations to solve the problem of multilayer

doubly curved concrete shell with two functions to find for the vertical load component case z (equation (2)):

$$\begin{aligned}
&P_1\frac{\partial^8\psi}{\partial\alpha^8} + P_3\frac{\partial^8\psi}{\partial\alpha^6\partial\beta^2} + P_5\frac{\partial^8\psi}{\partial\alpha^4\partial\beta^4} + P_4\frac{\partial^8\psi}{\partial\alpha^2\partial\beta^6} + P_2\frac{\partial^8\psi}{\partial\beta^8} + O_1\frac{\partial^6\psi}{\partial\alpha^6} + \\
&+ O_3\frac{\partial^6\psi}{\partial\alpha^4\partial\beta^2} + O_4\frac{\partial^6\psi}{\partial\alpha^2\partial\beta^4} + O_2\frac{\partial^6\psi}{\partial\beta^6} + k_2^2\frac{\partial^4\psi}{\partial\alpha^4} + 2k_1k_2\frac{\partial^4\psi}{\partial\alpha^2\partial\beta^2} + \\
&+ k_1^2\frac{\partial^4\psi}{\partial\beta^4} = Z,
\end{aligned}$$

(2)

where $P_i(\alpha, \beta)$ and $O_i(\alpha, \beta)$ are parameters that depend on the geometrical size of the shell.

2.2. The Double-Layer Doubly Curved Concrete Shell Roof Was Built.

Before investigating the initial parameters affecting the state of stress and strain of the shell, this study has been conducted to build a double-layer doubly curved shell model and conduct this shell experiment. The ANSYS simulation and experimental structure design model are followed by TCVN 5574:2018 [35], which is presented in Tables 1 and 2.

The equation for the surface of the doubly curved shell is shown in equation (3):

$$z = f_1\left(\frac{x}{a}\right)^2 + f_2\left(\frac{y}{b}\right)^2,$$

(3)

where f is the height of the shell at its highest point, $f = f_1 + f_2 = 600$ mm; $f_1 = 300$ mm and $f_2 = 300$ mm are the height in both directions; a and b are half the length of the shell's rectangular plan edge.

Double-layer curved concrete shell roof with a plan size of 3000×3000 mm, fixed joint with 4 vertical curved beams, and a constant cross-sectional area of 150×200 mm are supported on 4 columns with a cross section of $300 \times 300 \times 1300$ mm, as shown in Figure 1.

2.3. Making the Double-Layer Doubly Curved Concrete Shell Roof.

The shell fabrication process consists of 3 steps: make the formwork according to the shape of the doubly curved shell (equation (3) and Figure 1(a)), the first layer of steel fibres concrete was poured, and then the normal concrete layer is poured last, as shown in Table 1 and Figure 2.

2.4. Installation of Devices and Shell Experiment.

Installation diagrams of strain gauges (tensiometers) are measured at the top and bottom surfaces and vertical displacement measuring devices (LVDTs) are measured at the bottom surface of the shell. Because of the influence of measuring devices, the number of measuring positions is arranged as shown in Figures 3(a) and 3(b).

In the condition of using this curved shell roof in the buildings in Vietnam, the load acting on the shell includes the load on the shell itself and the live load on repairing the shell, so the total effective load is 5 kN/m^2 or 45 kN of load acting on the shell surface (shell surface area: 9 m^2). The total load acting on the shell is 5 kN/m^2, and depending on the weight of the sand or small concrete blocks, it has been divided into 7 levels in this study.

Load acting on the shell consist of 7 levels: level 1 = 1.63 kN/m^2, level 2 = 2.17 kN/m^2, level 3 = 2.72 kN/m^2, level 4 = 3.26 kN/m^2, level 5 = 4.35 kN/m^2, level 6 = 5 kN/m^2, and level 7 = 5.44 kN/m^2. At the first 4 levels, the load is applied to the shell by small sand and then concrete blocks, as shown in Figure 3(c). All measuring devices at each level are linked to the computers, as shown in Figure 3(d).

In addition, in the process of pouring concrete layer by layer, it is necessary to check the thickness of the layers, and after experimenting, drilling holes are made to check the actual layers, as shown in Figure 3(e).

2.5. Finite Element Model for Double-Layer Doubly Curved Concrete Shell Roof in ANSYS

2.5.1. Elements and Models.

In numerical simulation by ANSYS, this study used solid65 element to simulate concrete; this is an 8-node element and easy to analyze material nonlinearly and can simulate steel fibres in concrete with a concrete coefficient; this concrete coefficient is applied to the concrete according to the volumetric content that the distributed steel fibres. In analyzing steel fibres in concrete, ANSYS also asked to choose a model for them. Because the steel fibres are distributed in the concrete, this study chooses smeared model in three models of ANSYS, smeared, embedded, and discrete models, as shown in Figure 4.

According to the perimeter of the shell boundary, there are steel bars (Figures 1(b) and 1(c)), so BEAM188 element was used in simulation analysis and this is an element consisting of 2 nodes.

Concrete is a brittle material, so a concrete cracking model must be selected in the analysis. There are two concrete cracking models, discrete and smeared, but the steel fibres are distributed in the concrete, so in this study, the smeared model was selected and shown in Figure 5.

Simulating with two different materials, normal concrete (NC) and steel fibres concrete (SFC), three models are used, continuous model, interface model, and thin-layer model. However, in this research, the NC is on steel fibres concrete, only in contact with each other, so the interface model was chosen, as shown in Figure 6.

2.5.2. Material Properties.

In compression result of two materials, SFC and NC, in the experiment (Figure 7), the stress-strain relationship of these two types of concrete is consistent with Kachlakev's model. Therefore, in this study, Kachlakev's model was used in the following models: Hognestad, Todeschini, Kent and Park, and Kachlakev.
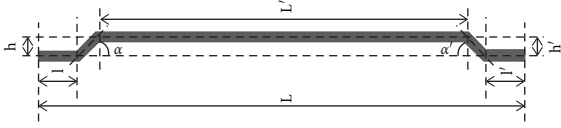
In the simulation, the failure surface model is also built, with the 2 types of concrete in this research and the selected solid65 element; the failure criteria of Willam and Warnke are appropriate, as shown in Figure 8.

Meshing: the meshing of elements in the shell and the nodes of the mesh must be together; if the mesh is too thick, the calculation time will be slow. With this thin-shell

TABLE 1: Geometric and material parameters of concrete shell.

	Concrete grade	Thickness (mm)	Modulus of elasticity (kN/m^2)	Concrete type
Layer 1 (below)	B30	20	3.25×10^7	Steel fibres, 2% (volume)
Layer 2 (above)	B20	30	2.75×10^7	Normal

TABLE 2: Parameters of Dramix steel fibres in shell.

Diameter (d)	0.5 mm $\pm$ 0.04 mm
Length (L)	30 mm $\pm$ 2 mm
Ratio (L/d)	60
Hook length (l and l')	2–4 mm
Hook depth (h and h')	1.8 mm + 0.3 mm
Bending angle (α and α')	45°
Torsion angle	$<30^0$
Number of fibres in 1 kg	17400
Tensile	>1.2 kN/mm^2

structure, the mesh shape is divided by spatial tetrahedron, and the element size is half the thickness of the thinnest shell concrete layer as shown in Figure 9(a).

Fixed link shell with vertical curved beams: the applied load is distributed on the top surface of the shell at the nodes of the tetrahedron mesh, by a compressive force P uniformly distributed over the shell surface, as shown in Figure 9(b).

3. Results and Discussion

3.1. Evaluation of Research Results. The experimental results of the shell roof are compared with ANSYS and Sap2000 software by values of vertical displacement and stresses; total effective load is 5 kN/m^2.

(i) Load and vertical displacement relationship of the shell in methods is shown in Figure 10.

Discussion of Result. The study results in Figure 10 show that ANSYS and Sap2000 are similar (here are the numeric methods), so when these numeric methods are compared to the experimental method, there is a difference near the shell boundary and at the top of the shell. There is a larger vertical displacement value near the shell boundary, but a smaller vertical displacement value at the top of the shell, and the value difference between the methods is very small (0.05 mm). As a result, the vertical displacement values of all three methods are similar.

(ii) Load and stress relationship of the shell in methods is shown in Figure 11.

Discussion of Result. In Figure 11, with the ANSYS and Sap2000 methods, the value of the stresses is similar. However, the value of the experimental method is changed at the location ($x = 1.2$ m) of the

stress σ_x and at the location ($x = 0.6$ m) of the stress σ_y, compared with ANSYS and Sap2000 methods from 15 to 20 N/cm^2. These values may be affected by measuring devices, material homogeneity, and so on; given this difference between experimental and numerical methods, further studies are needed, but this change is very small and can be accepted in this study.

The results of this experimental study show that this multilayer doubly curved shell roof from location 0.6 m to 1.2 m tends to be affected by boundary conditions, so it also needs further studies on the influence of these boundary conditions.

With the use of this shell roof under the conditions of use in Vietnam, cracks have not appeared in the shell, and it is necessary to continue research in ANSYS with larger load values.

3.2. Investigate the Effect of Thickness of Each Layer. In experimental research and simulated by ANSYS with SFCL (h_1), thickness of 2 cm, under NCL (h_2), thickness of 3 cm, and relationships load-vertical displacement and load-stress in the x and y directions have been built (Case 1). To investigate the influence of thickness of layers on the stress-strain state in the shell, this study continues with 2 investigated cases, Case 2 and Case 3, by ANSYS , as presented in Table 3.

Discussion of Result

(i) *Case 1.* With the load acting on the shell surface according to the conditions of use in Vietnam of 5 kN/m^2, the shell has no cracks. Experimentally, it is difficult to study the shell further, and ANSYS will simulate the shell at larger load levels. So, in the period when cracks appear in the concrete, $P = 14$ kN/m^2, stress 133.8 N/cm^2, and the first cracks appeared at the SFC layer and along the shell boundary with a vertical displacement at the top of the shell of 0.17 mm (Figure 12).

(ii) *Case 2.* Similarly, in the period when cracks appear in the concrete, $P = 12.5$ kN/m^2, stress 139 N/cm^2, and the first cracks appeared at the SFC layer and along the shell boundary with a vertical displacement at the top of the shell of 0.187 mm (Figure 13).

(iii) *Case 3.* Similarly, in the period when cracks appear in the concrete, $P = 17.5$ kN/m^2, stress 127.6 N/cm^2 and the first cracks appeared at the SFC layer and along the shell boundary with a vertical displacement at the top of the shell of 0.207 mm

(a)

(b)

(c)
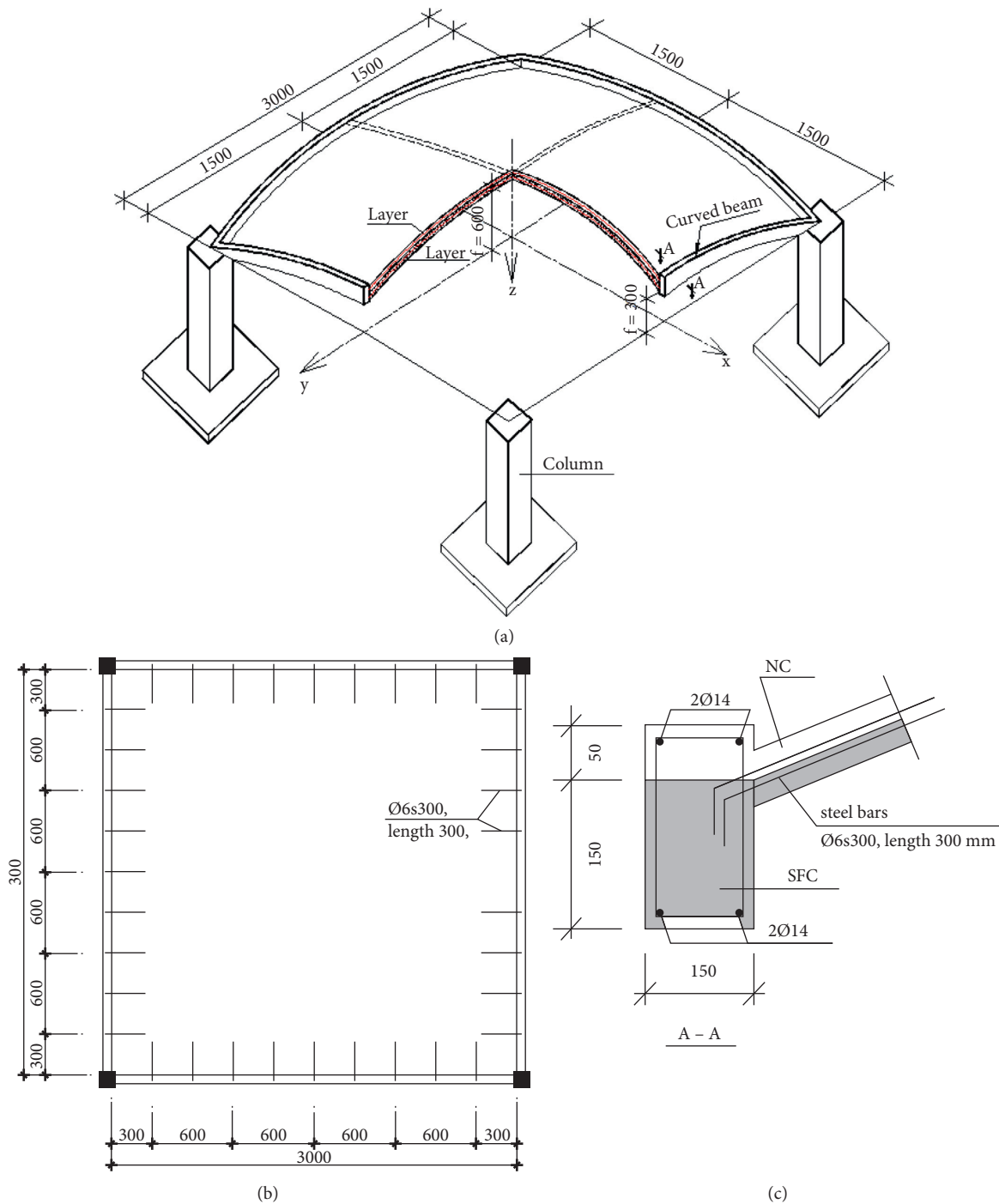
FIGURE 1: Doubly curved shell with double-layer, 3000 × 3000 mm. (a) Doubly curved shell model, (b) plan of steel bars connected between the shell and curved beams, and (c) A-A section.

The results of vertical displacements and stresses in the 3 investigated cases are shown in Figure 14.

Vertical displacement and stresses values are presented in Table 4.

Discussion of Result. In Figure 14 and Table 4,

(i) Case 1 and Case 3: the total thickness is equal but the SFCL is larger, and the vertical displacement and stresses are smaller in the 3 investigated cases. In Figure 14(a), the thickness of the SFCL is increased, and the vertical displacement is reduced; that is, the larger the thickness of the SFCL is, the better the shell works.

(ii) The stage where the concrete cracks appear: in Case 3, the underlying SFCL is thicker, so the cracks appear more slowly. In Case 2 (minimum

(a)

(b)

(c)

FIGURE 2: Making the formwork and pouring concrete layers: (a) make the formwork, (b) the first layer of steel fibres concrete was poured, and (c) the normal concrete layer is poured last.

thickness), cracks appear earlier than in other cases. That is, the underlying SFCL will resist the appearance of cracks in the shell when the load is increased.

(iii) The research results show that the cracks in the three investigated cases are in the SFCL below it. That is, at the shell boundary, the lower layer of concrete is tensile, while the upper layer of normal concrete is compressive.

3.3. Investigate the Effect of the Location of the SFCL.
The use of an SFCL under an NCL was studied. The SFCL is put on top of the NCL in other cases (such as when fixing the shell roof's surface). This study conducted two experiments to see how the location of the SFCL influences the state of stress and strain of the shell; the SFCL is located above and below the NCL, with the thickness of the layers in the shell being the same, as presented in Table 5.

The results of vertical displacements and stresses are shown in Figure 15.

Vertical displacement and stresses values are presented in Table 6.

Discussion of Result.

In Figure 15 and Table 6, the concrete begins to show cracks; in Case 4, load $P = 11.5 \, \text{kN/m}^2$, stress is $102.7 \, \text{N/cm}^2$, the first cracks appear in the shell along the boundary of the lower NCL, and the maximum vertical displacement at the top of the shell is $0.174 \, \text{mm}$, while in Case 2, it is $P = 12.5 \, \text{kN/m}^2$; this means that the SFCL below NCL will crack later than it does on top, and in both Case 2 and Case 4, the concrete layer below will be cracked first.

When the SFCL is located in the compression zone of the shell, the stress σ_x near the shell boundary is reduced by 15%, and the stress σ_y is reduced by 52%. The results of this study show that the lower layer is the tensile layer, and the upper layer is compressive. Therefore, strengthening the SFCL located in the tensile zone will be more effective when it is located above.

3.4. Investigate the Influence of the Percentage of Steel Fibres Contained in Concrete.
In Table 3, the percentage of steel

(a)

(b)

(c)

(d)

(e)
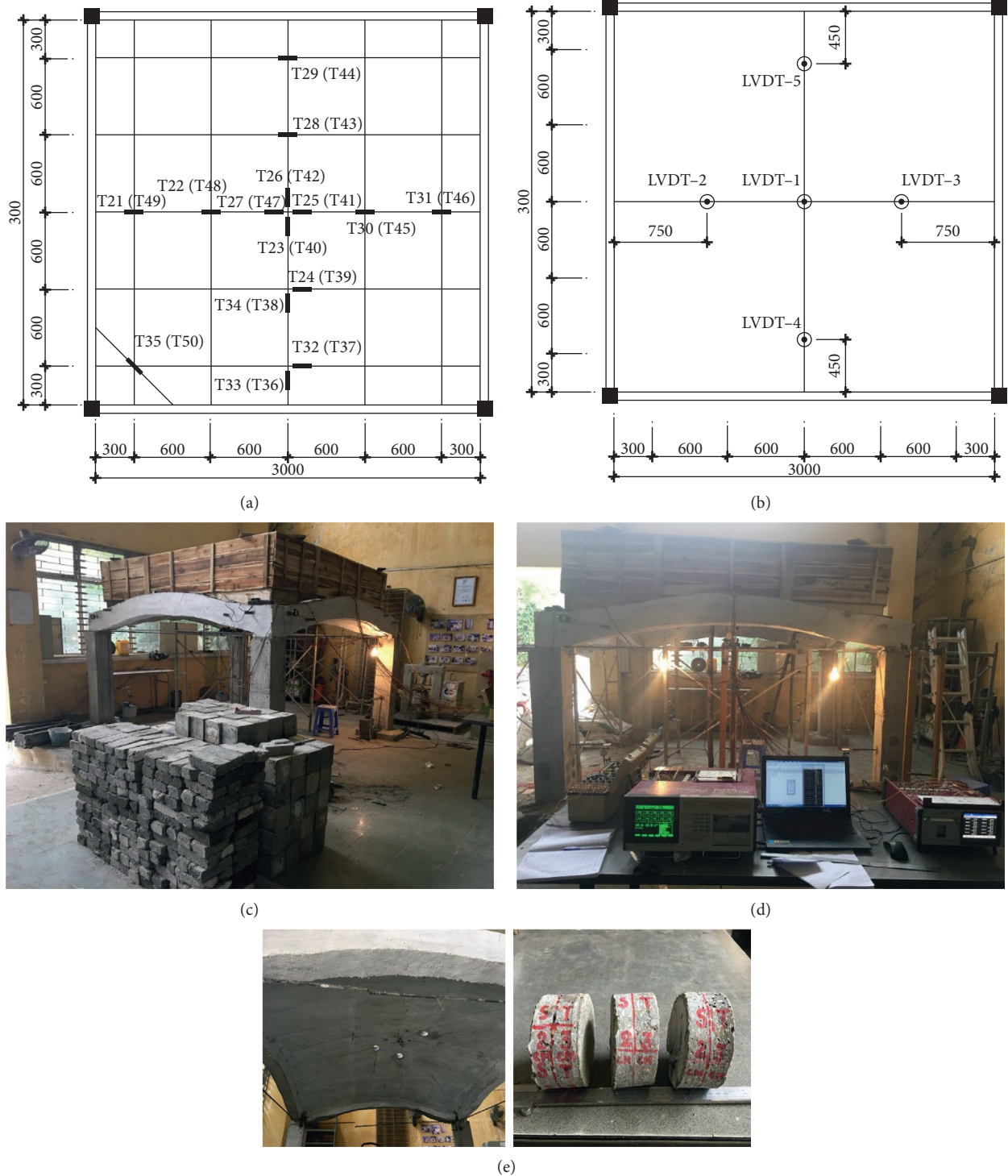
FIGURE 3: Installation of measuring equipment and loading on the shell. (a) Installation diagram of strain gauges (tensiometers). (b) Installation diagram of LVDTs. (c) Load the shell with small concrete blocks. (d) Connect the measuring equipment to the computers. (e) Check the thickness of the layers.

fibres contained in concrete is 2%, and here it is changed to 0% and 3% for all 4 investigated cases .

Case 1. This study investigates the change of the percentage of steel fibres contained in concrete, 0%, 2%, and 3%, as shown in Figure 16:

Discussion of Result.

Direction of movement of the layers in the shell: the upper layer displaces towards the center, while the lower layer is directed away from the center of the shell when the shell is under load (Figure 16(b)).

(a)

(b)

(c)
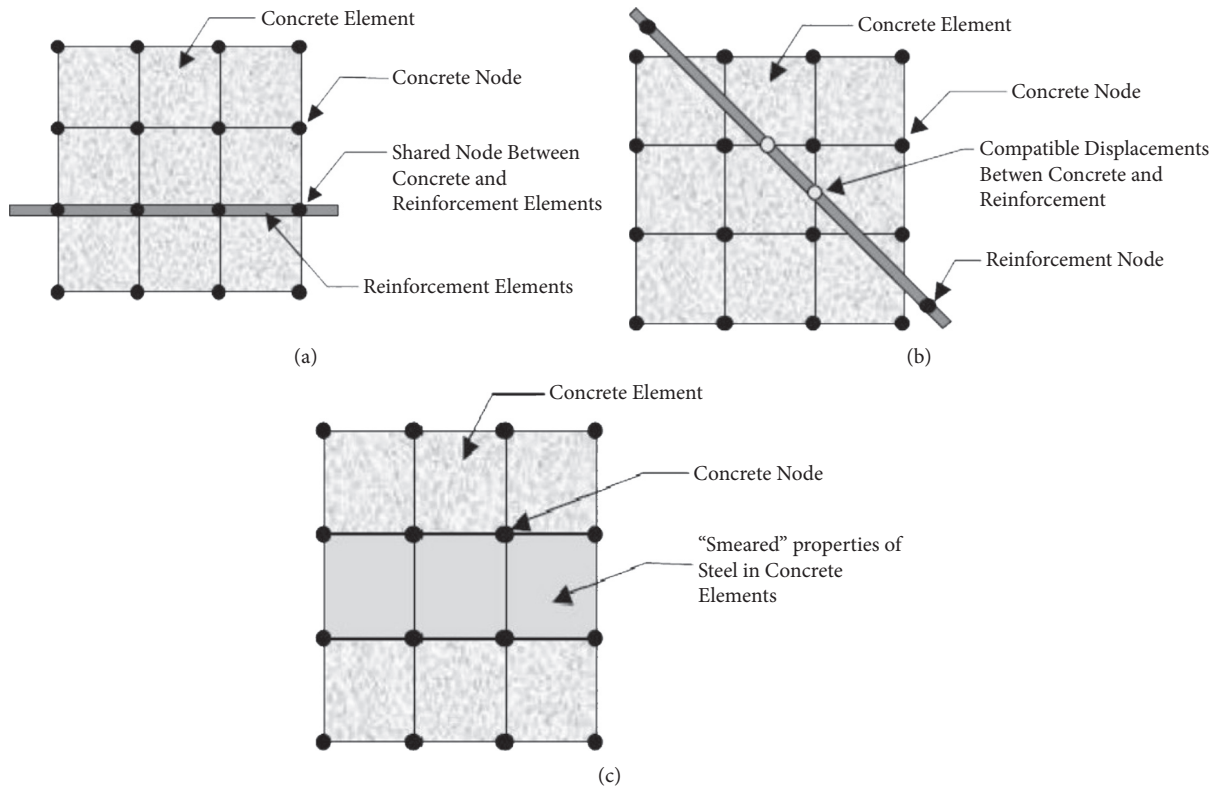
Figure 4: Steel fibres' models [31]: (a) smeared model, (b) embedded model, and (c) discrete model.

(a)   (b)
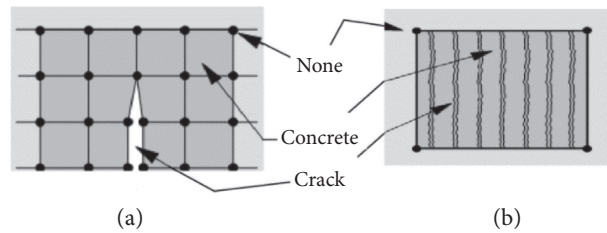
Figure 5: Concrete cracking model [31]: (a) discrete and (b) smeared.

(a)   (b)   (c)
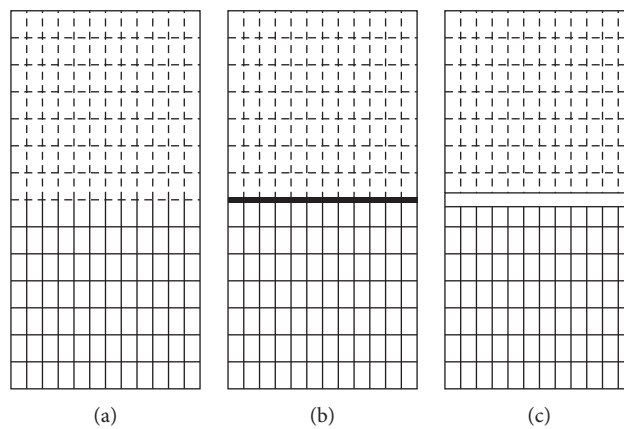
Figure 6: Three contact models: (a) continuous model, (b) interface model, and (c) thin-layer model.
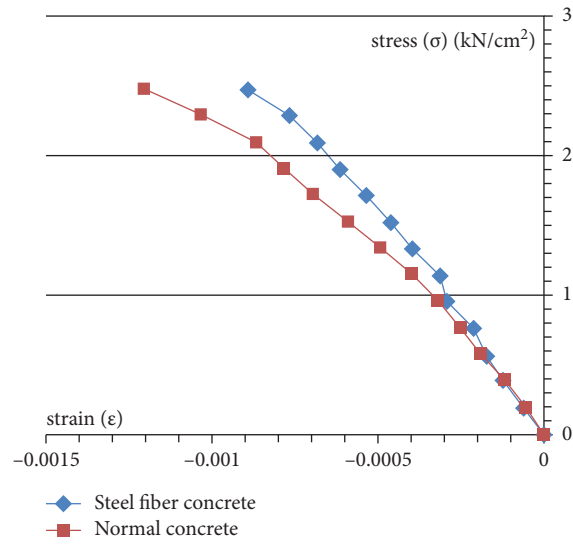
FIGURE 7: Stress-strain relationship of the two types of concrete.
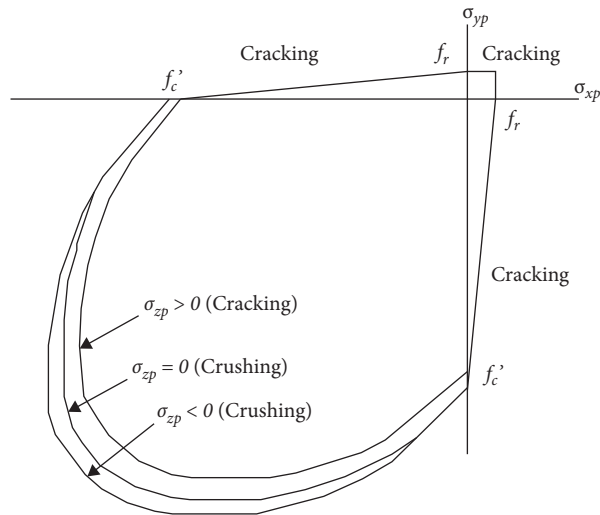
FIGURE 8: Failure Surface for concrete [31].

| (a) | (b) |
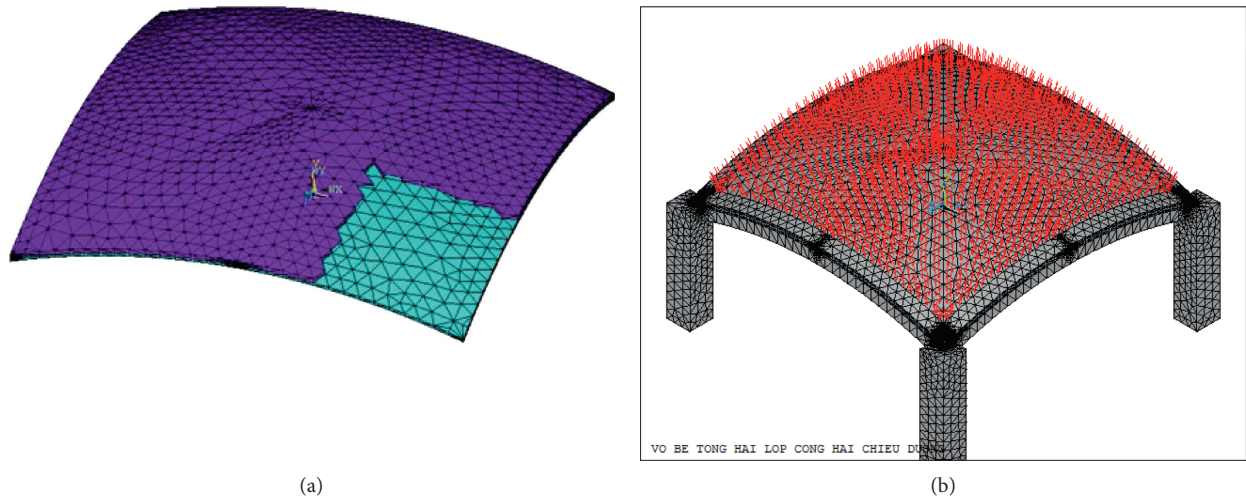
FIGURE 9: Meshing, boundary of shell, and load. (a) Meshing of elements; (b) boundary of shell and load.
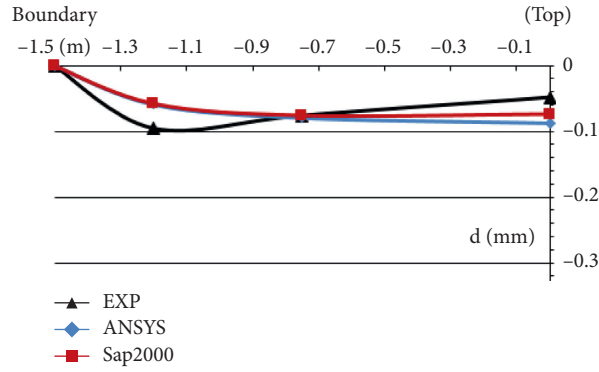
FIGURE 10: Load and vertical displacement in methods.

(a)

(b)
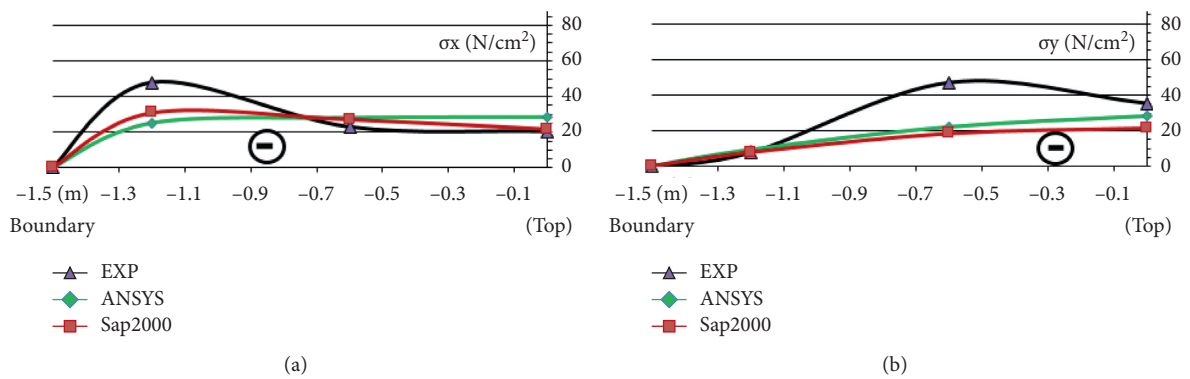
FIGURE 11: Stresses in the methods: (a) stress σ_x in the methods; (b) stress σ_y in the methods.
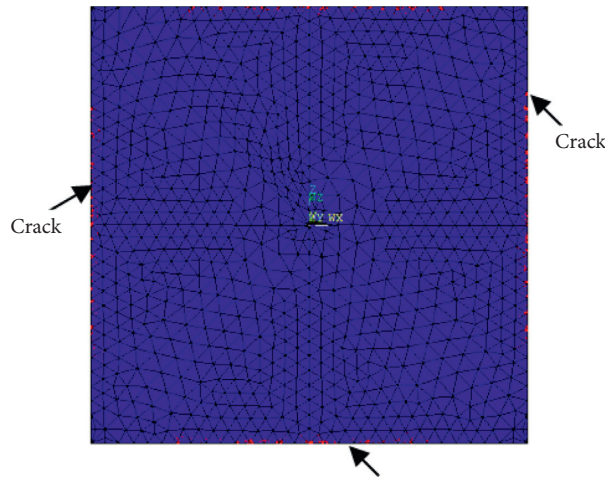
VO BE TONG HAI LOP CONG HAI CHIEU DUONG

FIGURE 12: Location of cracks in shell (Case 1).

In Figure 16(c), the change of vertical displacement value is 0.05 mm, and this value is very small and considered the same.

Stress in the x and y directions (Figures 16(d), and 16(e)): these stresses are the same for the percentage of

steel fibres in concrete 0% and 3% and vary from 9 N/cm^2 to 13 N/cm^2 when the percentage of steel fibres is 2%. Not using this percentage of steel fibres or using so much the percentage of steel fibres in concrete is inefficient and counterproductive, that is, 3% steel

VO BE TONG HAI LOP CONG HAI CHIEU DUONG

(a)

VO BE TONG HAI LOP CONG HAI CHIEU DUONG

(b)

VO BE TONG HAI LOP CONG HAI CHIEU DUONG

(c)

VO BE TONG HAI LOP CONG HAI CHIEU DUONG

(d)

VO BE TONG HAI LOP CONG HAI CHIEU DUONG

(e)
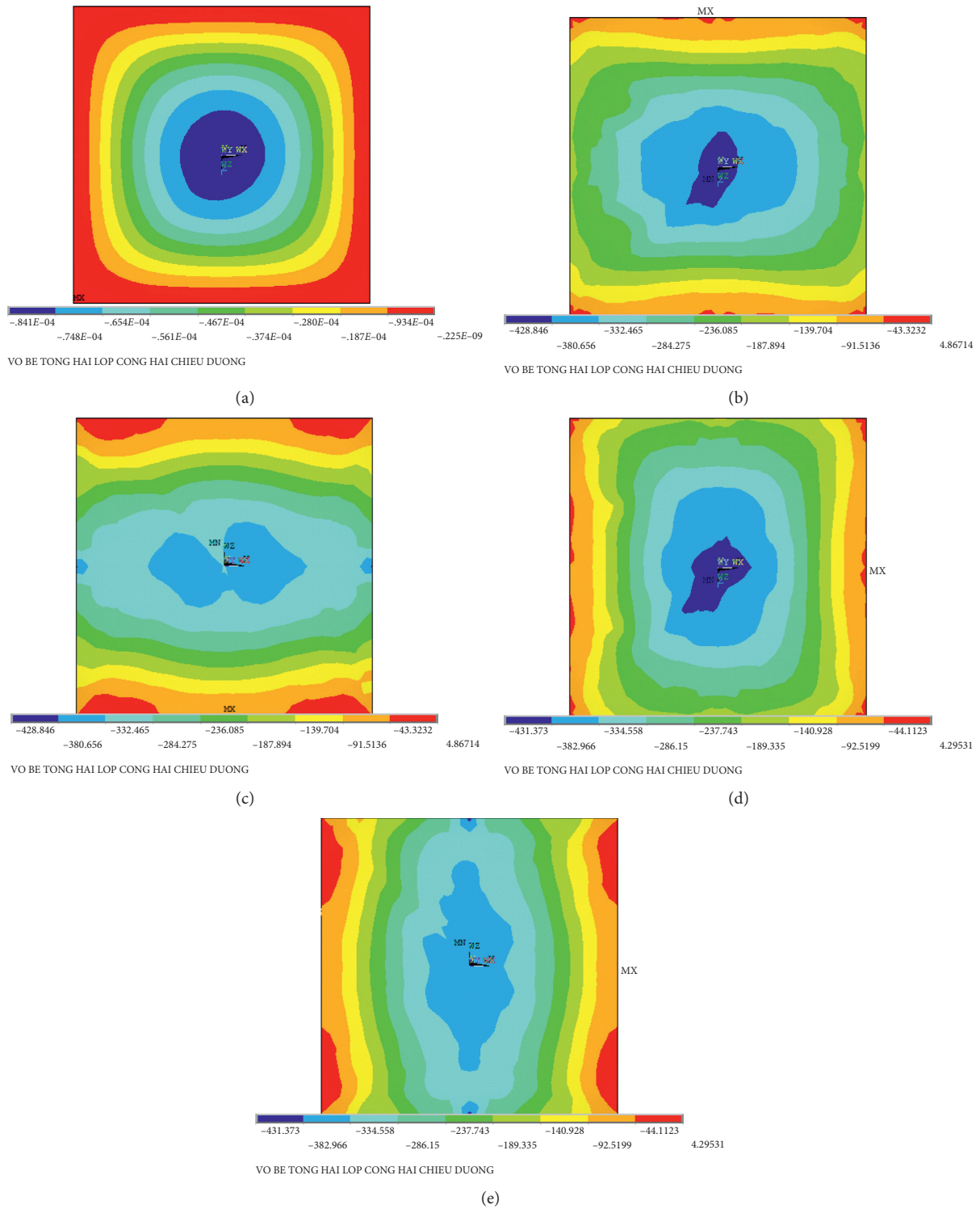
FIGURE 13: Vertical displacement and stresses (Case 2): (a) vertical displacement in shell; (b) stress σ_x of top surface in shell; (c) stress σ_x of bottom surface in shell; (d) stress σ_y of top surface in shell; (e) stress σ_y of bottom surface in shell.

TABLE 3: Thickness of layers with the following 3 cases studied.

	Case 1	Case 2	Case 3
$h_1 + h_2$ (cm)	2 + 3	2 + 2	3 + 2

(a)

(b)

(c)

FIGURE 14: Vertical displacement and stresses in 3 investigated cases: (a) vertical displacement of shell in 3 investigated cases; (b) stress σ_x of shell in 3 investigated cases; (c) stress σ_y of shell in 3 investigated cases.

TABLE 4: Vertical displacement and stresses values.

(a) Vertical displacement in 3 investigated cases

Location	Vertical displacement (mm)		
(m)	Case 1	Case 2	Case 3
0	−0.071	−0.084	−0.069
0.75	−0.063	−0.074	−0.054
1.1	−0.039	−0.047	−0.031
1.5	0	0	0

(b) Stresses in 3 investigated cases

Location	Stress σ_x (N/cm^2)			Stress σ_y (N/cm^2)		
(m)	Case 1	Case 2	Case 3	Case 1	Case 2	Case 3
0	−37.1	−42.8	−36.9	−36.6	−43.1	−36.5
0.6	−32.7	−38.1	−31.5	−32.1	−38.3	−31.1
1.2	−23.9	−28.4	−26.1	−9.4	−14	−9.3
1.5	0	0	0	0	0	0

TABLE 5: Location of the SFCL.

	Case 2 (SFCL on bottom)	Case 4 (SFCL on top)
$h_1 + h_2$ (cm)	2 + 2 (cm)	2 + 2 (cm)

fibres that has surpassed the limit of the percentage of steel fibres in concrete [35].

Case 2. This study investigates the change of the percentage of steel fibres in concrete, 0%, 2%, and 3%, as shown in Figure 17:

Discussion of Result.

In Figure 17, similar to Case 1, vertical displacement and stresses σ_x and σ_y with 2% the percentage of steel fibres are the most optimal percentage of the studied percentage of steel fibres. The vertical displacement at

(a)

(b)

(c)

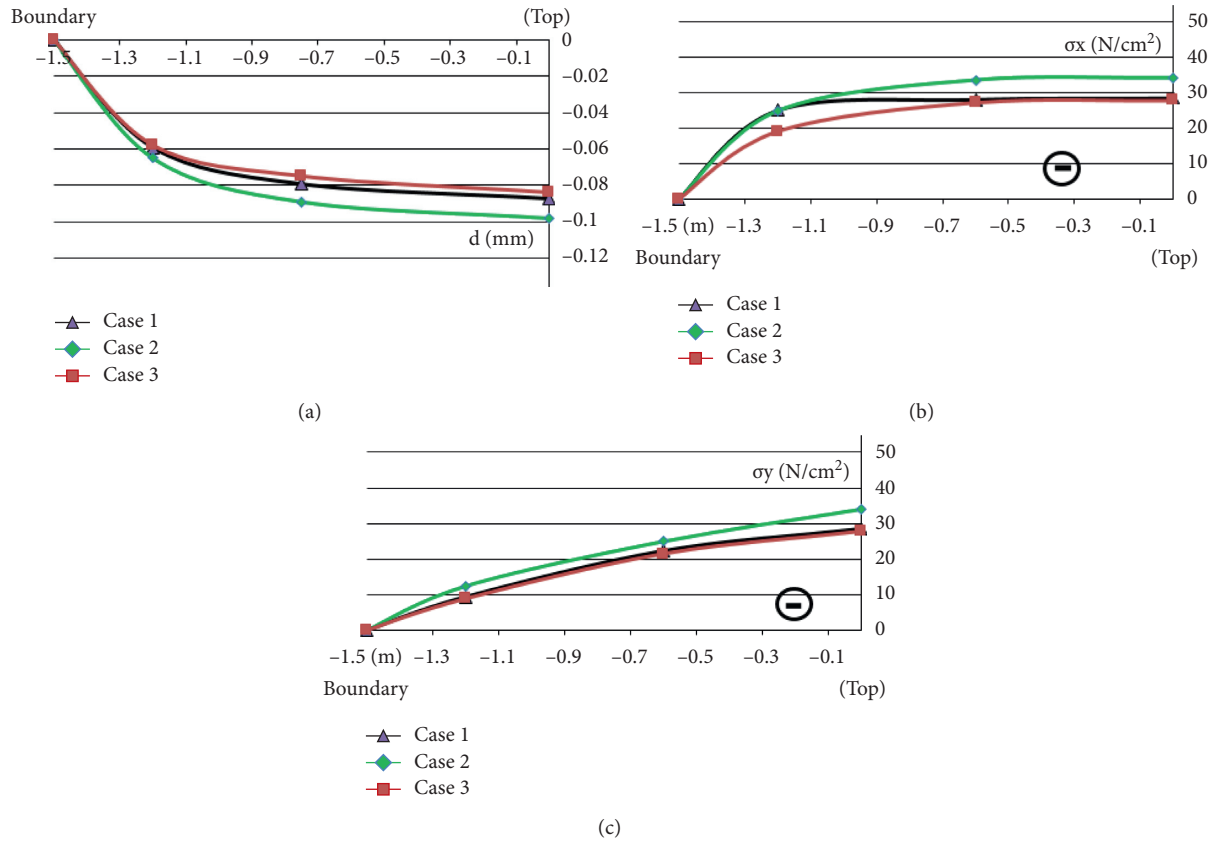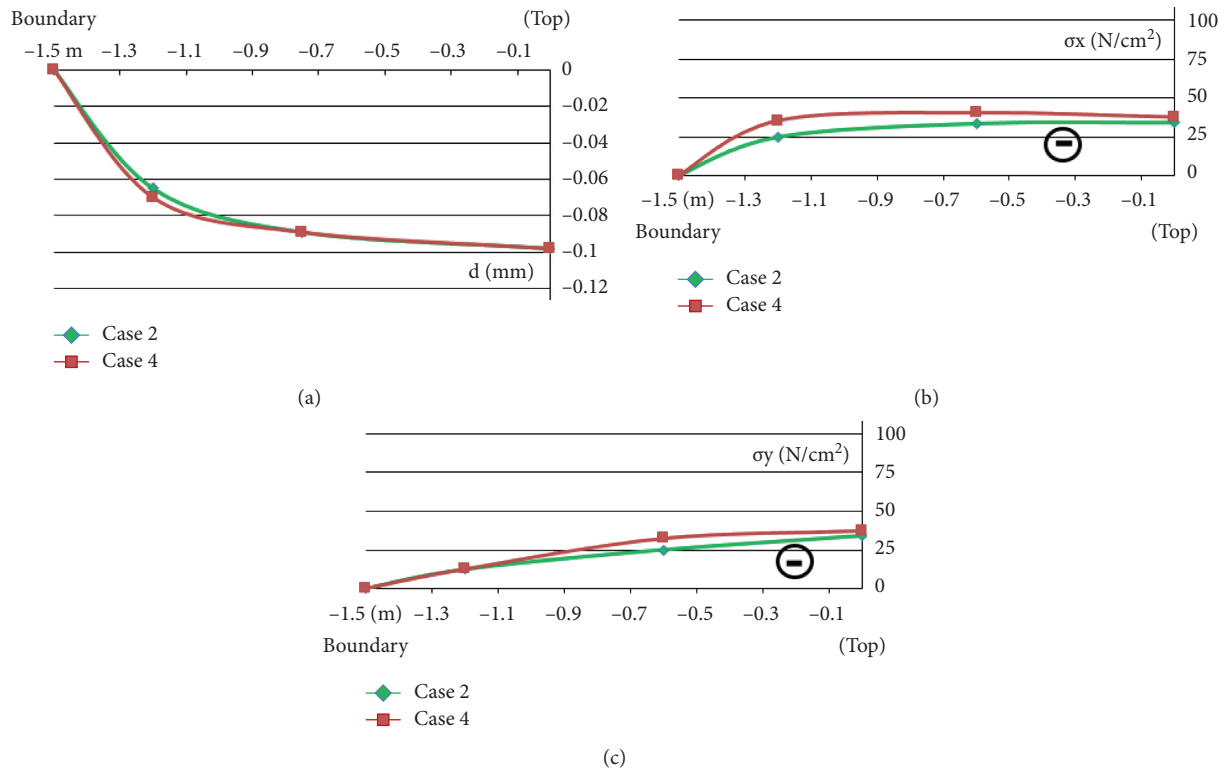FIGURE 15: Vertical displacement and stresses in Case 2 and Case 4: (a) vertical displacement of shell in Case 2 and Case 4; (b) stress σ_x of shell in Case 2 and Case 4; (c) stress σ_y of shell in Case 2 and Case 4.

TABLE 6: Vertical displacement and stresses values in cases.

(a) Vertical displacement in Case 2 and Case 4			
Location		Vertical displacement (mm)	
(m)	Case 2	Case 4	Difference (%)
0	−0.084	−0.084	0
0.75	−0.074	−0.075	1.35
1.1	−0.047	−0.048	2.13
1.5	0	0	0
(b) Stresses in Case 2 and Case 4						
Location		Stress σ_x (N/cm^2)			Stress σ_y (N/cm^2)	
(m)	Case 2	Case 4	Difference (%)	Case 2	Case 4	Difference (%)
0	−42.8	−49.7	16.12	−43.1	−49.1	13.92
0.6	−38.1	−44.1	15.75	−38.3	−43.6	13.84
1.2	−28.4	−32.8	15.49	−14.0	−21.3	52.14
1.5	0	0	0	0	0	0

the percentage of steel fibres in concrete is 2%, from 0% to 3% of 0.05 mm, which is very small and is considered unaffected. There is also the stress difference in the directions from 10 to 13 N/cm^2 at the location near the shell boundary and at the top of the shell.

The two analyzed cases (Case 1 and Case 2) showed that the locations near the boundary and at the top of the shell are the locations that will be sensitive to the load. When designing this shell, attention should be paid to these 2 locations.

Case 3. This study investigates the change of the percentage of steel fibres in concrete, 0%, 2%, and 3%, as shown in Figure 18.

Discussion of Result. In Figures 16–18, all 3 cases (Case1, Case 2, and Case 3) have the largest vertical displacement value at the top of the shell, and the difference is 0.9 mm. Stresses σ_x and σ_y are also the highest at the top of the shell and range from 29 to 39 N/cm^2. Among the percentage of steel fibres in concrete, the 2% steel fibres content is still the most

VO BE TONG HAI LOP CONG HAI CHIEU DUONG

(a)

VO BE TONG HAI LOP CONG HAI CHIEU DUONG

(b)

—▲— Case 1 – 2%
—◆— Case 1 – 3%
—■— Case 1 – 0%

(c)

—▲— Case 1 – 2%
—◆— Case 1 – 3%
—■— Case 1 – 0%

(d)

—▲— Case 1 – 2%
—◆— Case 1 – 3%
—■— Case 1 – 0%

(e)
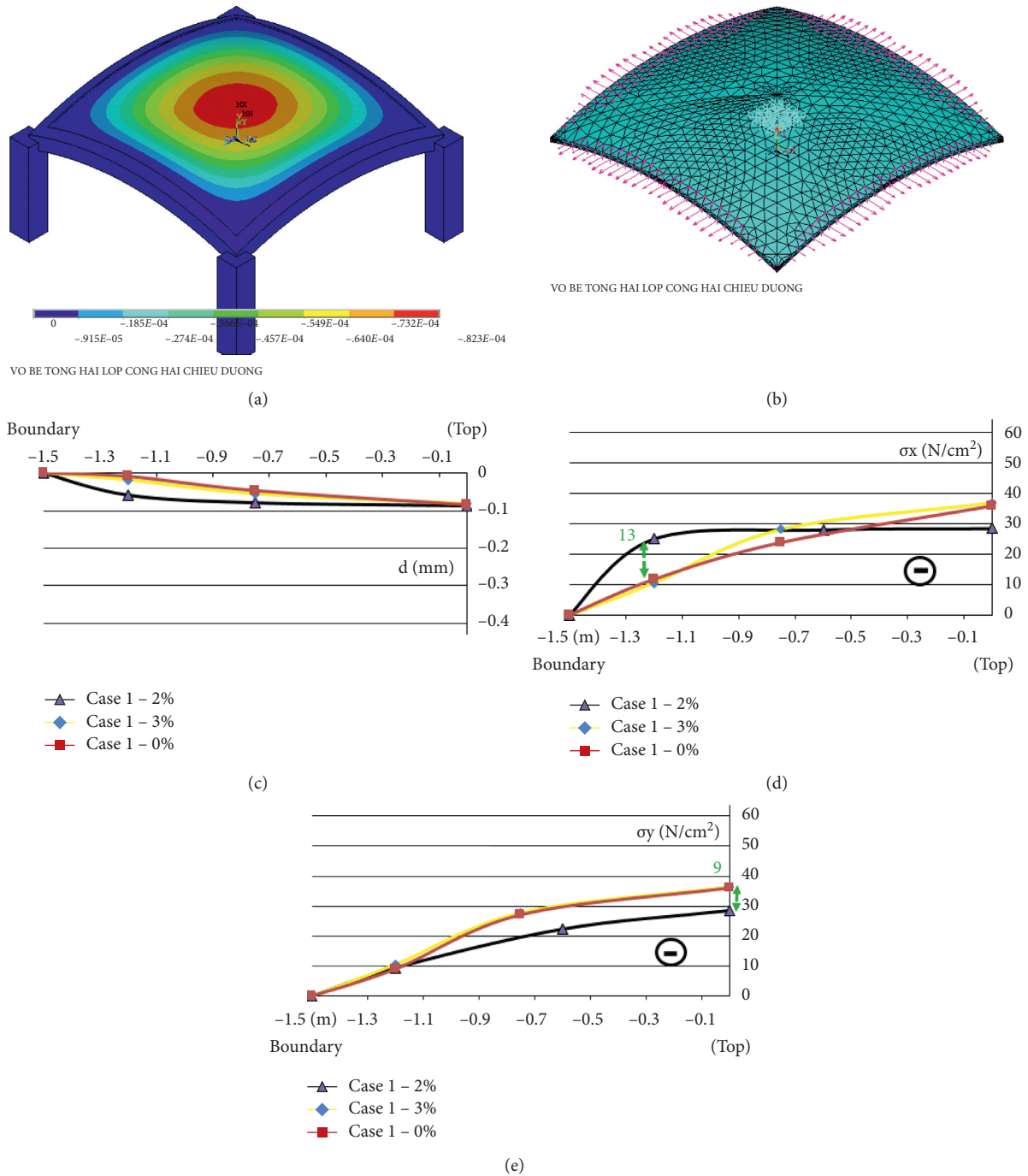
FIGURE 16: The change of percentage of steel fibres in concrete (Case 1). (a) Spectrum of vertical displacement in the shell; (b) the direction of movement of each layer; (c) vertical displacement of the shell; (d) stress σ_x of shell; (e) stress σ_y of shell.

optimal in all the investigated cases. The locations near the boundary and top of the shell are locations that are very sensitive to the load.

Case 4. This study investigates the percentage of steel fibres in concrete, 0%, 2%, and 3%, as shown in Figure 19.

Discussion of Result. In Figure 19, the vertical displacement of the shell is similar to the three cases above where the SFCL is placed on top of NCL. However, the stress values σ_x and σ_y start to change in the direction of increasing the stress value, and the stress at the top of the shell increases from 39 to 50 N/cm². The percentage

(a)

(b)

(c)
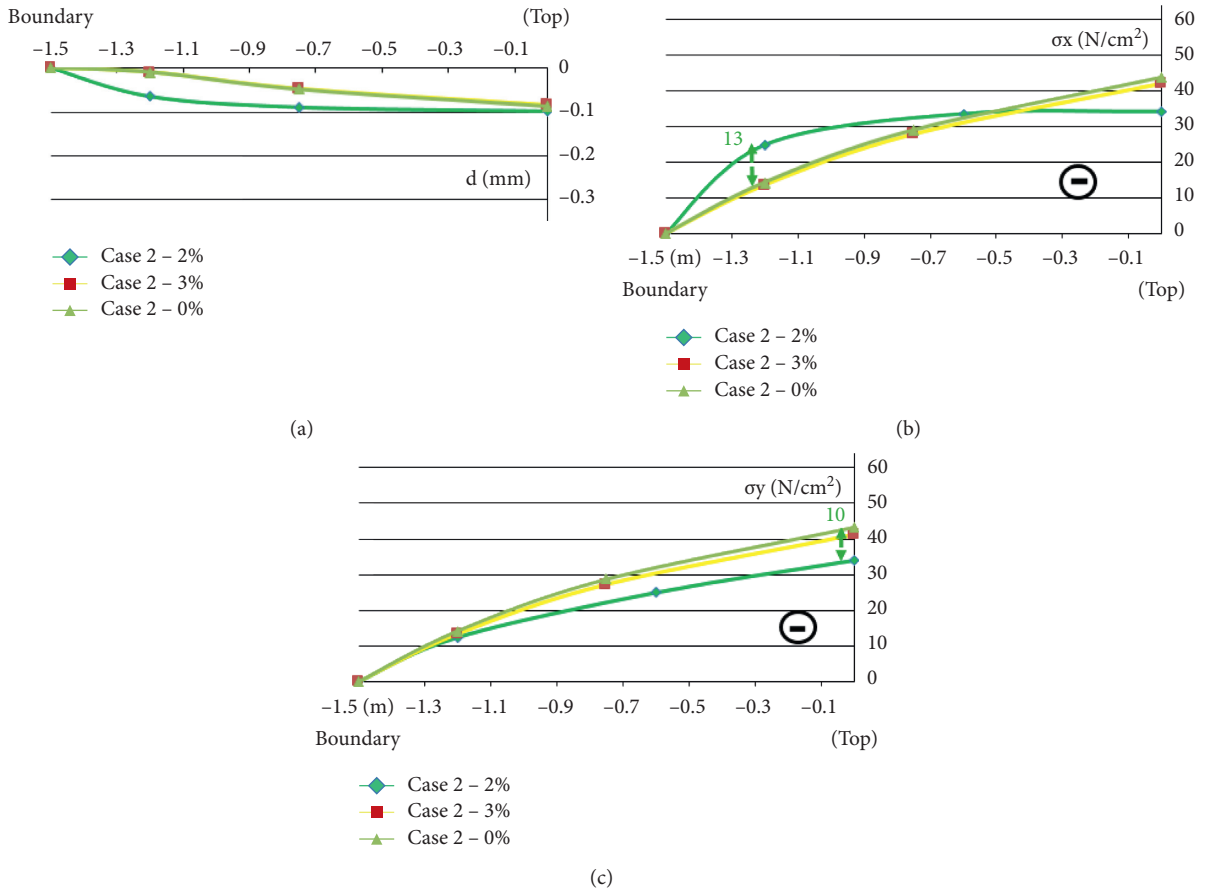
FIGURE 17: The change of percentage of steel fibres in concrete (Case 2): (a) vertical displacement of the shell; (b) stress σ_x of shell; (c) stress σ_y of shell.

(a)

(b)
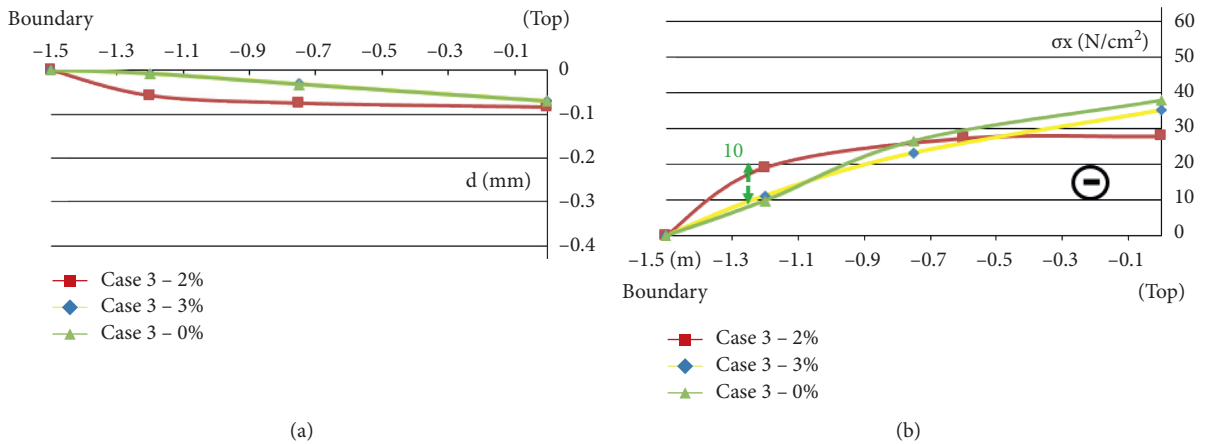
FIGURE 18: Continued.
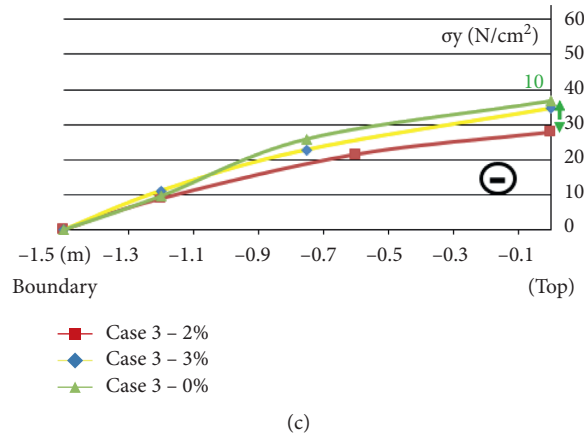
(c)

FIGURE 18: The change of percentage of steel fibres in concrete (Case 3): (a) vertical displacement of the shell; (b) stress σ_x of shell; (c) stress σ_y of shell.

(a)

(b)
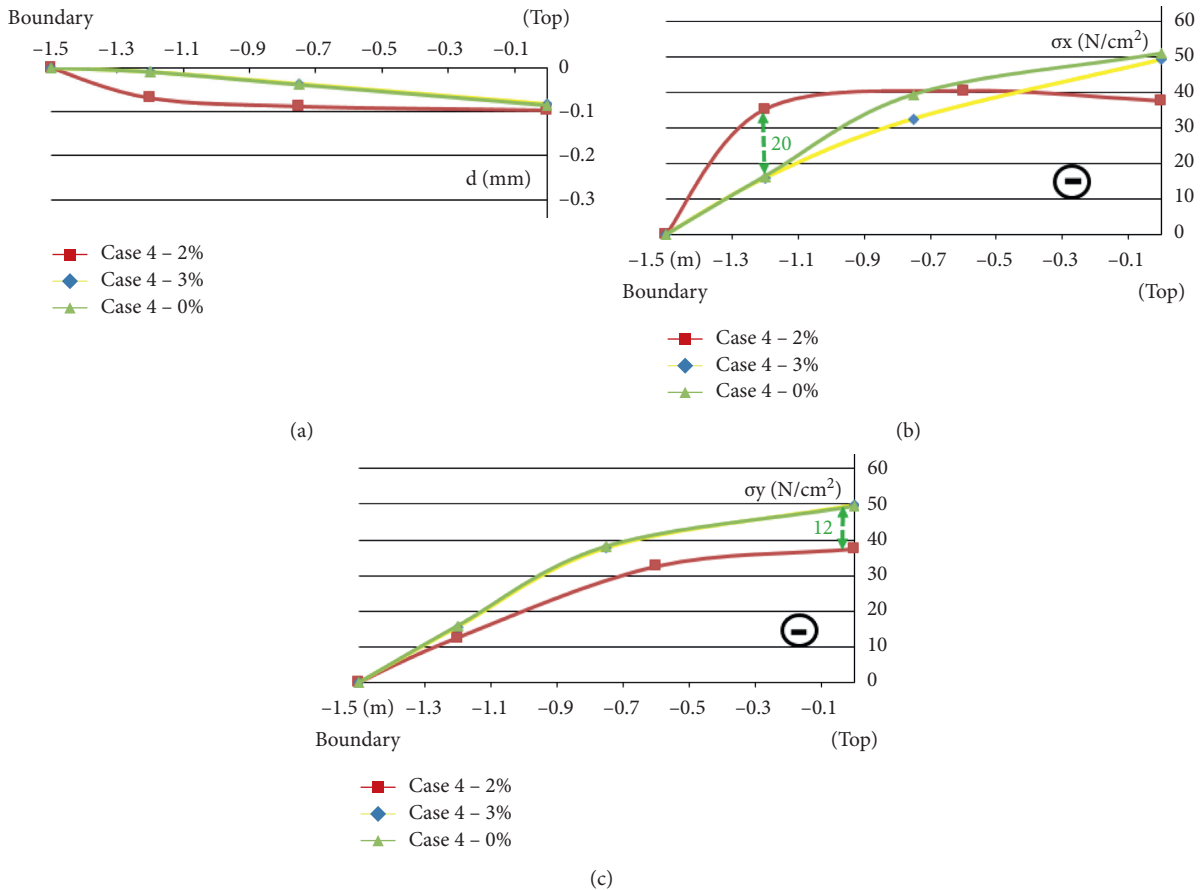
(c)

FIGURE 19: The change of percentage of steel fibres in concrete (Case 4): (a) vertical displacement of the shell; (b) stress σ_x of shell; (c) stress σ_y of shell.

of steel fibres in concrete with 2% is still the most optimal in all cases; however, the difference in stress between 2%, 0%, and 3% is 12 to 20 N/cm². The 4 cases that have been investigated show that the above SFCL will make the shell increase the stresses values in the directions.

4. Conclusion

The results of the study lead to the following conclusions:

(1) Research results of vertical displacement and stresses σ_x and σ_y in all 3 methods, experimental, ANSYS

simulation, and Sap2000 with similar shapes: however, the experimental results are affected by boundary conditions, material homogeneity, and so on, further research is needed at the location from 0.6 m to 1.2 m to clarify these difference values. However, these difference values are not large and can be accepted in this study.

(2) The influence of the thickness of the layers shows that the thickness of the SFCL is increased, and the vertical displacement is reduced; that is, the larger the thickness of the SFCL, the better the shell works. At the shell boundary, the lower layer of concrete is tensile, while the upper layer of NC is compressive.

(3) The influence of the location of the SFCL in the shell: the first cracks appear in the shell along the boundary of the lower NCL, and the SFCL below NCL will crack later than it does on top, and in both Case 2 and Case 4, the concrete layer below will be cracked first. Therefore, strengthening the SFCL located in the tensile zone will be more effective when it is located above.

(4) The influence of the percentage of steel fibres in concrete: not using this percentage of steel fibres, or using so much the percentage of steel fibres in concrete is inefficient and counterproductive. Among the percentage of steel fibres in concrete, the 2% steel fibres content is still the most optimal in all the investigated cases. The locations near the boundary and top of the shell are locations that are very sensitive to the load. The 4 cases that have been investigated show that the above SFCL will make the shell increase the stresses values in the directions.

Abbreviations

FE: Finite element
NC: Normal concrete
NCL: Normal concrete layer
SFC: Steel fibre concrete
SFCL: Steel fibre concrete layer.

Data Availability

The data used to support the findings of this study are included within the article.

Conflicts of Interest

The authors declare that there are no conflicts of interest regarding the publication of this paper.

References

[1] V. Z. Vlasov, *General Theory of Shells and its Applications in Engineering*, NASA TT F-99, Washinton DC, USA, 1964.

[2] R. K. Zamani and M. R. Bidgoli, "Seismic response of smart nanocomposite cylindrical shell conveying fluid flow using HDQ-Newmark methods," *Computers and Concrete*, vol. 20, no. 6, pp. 671–682, 2017.

[3] S. L. Dong, G. B. Bai, X. Q. Zheng, and Y. Zhao, "A spherical lattice shell composed of six-bar tetrahedral units: configuration, structural behavior, and prefabricated construction," *Advances in Structural Engineering*, vol. 19, no. 7, pp. 1–12, 2016.

[4] F. Miao, S.-L. Dong, H.-Q. Liang, X.-T. Wang, X.-L. Zhu, and C. Ding, "Manufacture and prefabrication practice on a test model of a novel six-bar tetrahedral cylindrical lattice shell," *Advances in Structural Engineering*, vol. 22, no. 2, pp. 287–296, 2018.

[5] B. Baby and L. G. Das, "Numerical study of concrete dome structure using ANSYS 17.0," *IJIRSET*, vol. 6, no. 5, pp. 8186–8193, 2017.

[6] H. D. Nguyen, "Compute the two-dimensional curved shell, the rectangular plan by the approximate method," *Building science and technology journal*, vol. 2, pp. 28–33, 2014.

[7] B. A. Harish, N. V. Ramana, and K. Manjunatha, "Finite element analysis of doubly curved thin concrete shells," *International Journal of Engineering Science and Innovative Technology*, vol. 4, no. 5, pp. 48–57, 2015.

[8] P. Sivakumar, K. Manjunatha, and B. A. Harish, "Experimental and FE analysis of funicular shells," *International journal of engineering and innovative technology*, vol. 4, no. 9, pp. 178–186, 2015.

[9] G. L. M. Danush, G. V. Sowjanya, and T. M. Siddesh, "Finite element analysis of doubly curved thin concrete shells with square and rectangular plan 15 m × 15 m and 15 m × 10 m under uniformly distributed load using Sap2000," *IRJET*, vol. 4, no. 6, pp. 560–564, 2017.

[10] S. S. Kadam, G. R. Gandhe, and D. H. Tupe, "Forced vibration analysis of invented umbrella roof shell using Ansys," *IJRPET*, vol. 3, no. 5, pp. 31–33, 2017.

[11] N. N. Meleka, M. A. Safan, A. A. Bashandy, and A. S. Abd-Elrazek, "Repairing and strengthening of elliptical paraboloid reinforced concrete shells with openings," *Archives of Civil Engineering*, vol. 59, no. 3, pp. 401–420, 2013.

[12] G. Stefano, V. Varano, G. Tomasello, and D. Alfonsi, "R-"Funicularity of form found shell structures," *Engineering Structures*, vol. 157, pp. 157–169, 2018.

[13] E. Verwimp, T. Tysmans, M. Mollaert, and M. Wozniak, "Prediction of the buckling behaviour of thin cement composite shells: parameter study," *Thin-Walled Structures*, vol. 108, pp. 20–29, 2016.

[14] T. M. Jeyashree, C. Arunkumar, and K. S. Ashok, "Experimental and analytical study on funicular concrete shell foundation under ultimate loading," *Asean journal of civil engineering*, vol. 18, no. 6, pp. 863–878, 2017.

[15] R. Keikha, A. Heidari, H. Hosseinabadi, and M. S. Haghighi, "Classical shell theory for instability analysis of concrete pipes conveying nanofluid," *Computers and Concrete*, vol. 22, no. 2, pp. 161–166, 2018.

[16] L. Qi, X. Zhang, and H. Huo, "Design bearing capacity of the initial imperfect lattice shell," *Advances in Structural Engineering*, vol. 19, no. 1, pp. 14–22, 2016.

[17] C. Kämper, P. Forman, T. Stallmann, M. A. Ahrens, P. Mark, and J. Schnell, "Optimised high-performance concrete shells for parabolic trough collectors," *Journal of the international association for shell and spatial structures*, vol. 58, no. 1, pp. 105–119, 2017.

[18] H. Schmidt, "Stability of steel shell structures," *Journal of Constructional Steel Research*, vol. 55, no. 1-3, pp. 159–181, 2000.

[19] H. C. Noh, "Ultimate strength of large scale reinforced concrete thin shell structures," *Thin-Walled Structures*, vol. 43, no. 9, pp. 1418–1443, 2005.

[20] W. Li, N. Nguyen-Thanh, and K. Zhou, "Geometrically nonlinear analysis of thin-shell structures based on an isogeometric-meshfree coupling approach," *Computer Methods in Applied Mechanics and Engineering*, vol. 336, pp. 111–134, 2018.

[21] S. A. Ambartsumyan, "Contributions to the theory of anisotropic layered shells," *Applied Mechanics Reviews*, vol. 15, pp. 245–249, 1962.

[22] A. J. M. Ferreira, E. Carrera, M. Cinefra, and C. M. C. Roque, "Analysis of laminated doubly-curved shells by a layerwise theory and radial basis functions collocation, accounting for through-the-thickness deformations," *Computational Mechanics*, vol. 48, no. 1, pp. 13–25, 2011.

[23] F. Tornabene, N. Fantuzzi, E. Viola, and J. N. Reddy, "Winkler-Pasternak foundation effect on the static and dynamic analyses of laminated doubly-curved and degenerate shells and panels," *Composites Part B: Engineering*, vol. 57, pp. 269–296, 2014.

[24] O. Allam, K. Draiche, A. A. Bousahla et al., "A generalized 4-unknown refined theory for bending and free vibration analysis of laminated composite and sandwich plates and shells," *Computers and Concrete*, vol. 26, no. 2, pp. 185–201, 2020.

[25] L. Xie, X.. Lu, X. Lu, Y. Huang, and L. Ye, "Multi-layer shell element for shear walls in open sees," *Computing in Civil and Building Engineering*, vol. 2014, pp. 1190–1197, 2014.

[26] A. S. Chepurnenko, "Stress-strain state of three-layered shallow shells under conditions of nonlinear creep," *Magazine of Civil Engineering*, vol. 8, pp. 156–168, 2017.

[27] D. Veenendaal, J. Bakker, and P. Block, "Structural design of the flexibly formed, mesh-reinforced concrete sandwich shell roof of NEST HiLo," *Journal of the international association for shell and spatial structures*, vol. 58, no. 1, pp. 23–38, 2017.

[28] Z. W. Miao, X. Z. Lu, J. J. Jiang, and L. P. Ye, "Nonlinear FE model for RC shear walls based on multi-layer shell element and micro-plane constitutive model," *Computational Methods in Engineering & Science*, p. 204, 2006.

[29] W. Chao, "The applicability study on the multi-layer shell element method in steel concrete structure of shield building," in *Proceedings of International Conference on Nuclear Engineering*, pp. 1–4, Shanghai, China, July 2017.

[30] T. M. D. Do and T. Q. K. Lam, "Design parameters of double layers steel fiber concrete beams," *Lecture Notes in Civil Engineering*, vol. 130, pp. 299–321, 2021.

[31] T. Q. K. Lam, T. M. D. Do, V. T. Ngo, T. T. N. Nguyen, and D. Q. Pham, "Concrete grade change in the layers of three-layer steel fibre reinforced concrete beams," *Journal of Achievements in Materials and Manufacturing Engineering*, vol. 1, no. 102, pp. 16–29, 2020.

[32] V. T. Ngo, T. Q. K. Lam, T. M. D. Do, and T. C. Nguyen, "Increased plasticity of nano concrete with steel fibers," *Magazine of Civil Engineering*, vol. 93, no. 1, pp. 27–34, 2020.

[33] V. T. Ngo, T. T. Bui, T. C. N. Nguyen, T. T. N. Nguyen, D. P. Nguyen, and T. Q. K. Lam, "Effect of nano-silica on fracture properties and crack extension resistance of high-performance concrete," in *Proceedings of the International Conference on Computational Methods*, pp. 137–148, Konstanz, Germany, September 2020.

[34] T. Q. K. Lam and T. M. D. Do, "Analysis of nonlinear material and steel fiber content in the double layers concrete shell," in *Proceedings of AIP Conference proceedings*, Article ID 020008, Chennai, India, December 2020.

[35] TCVN 5574:2018, *Design of Reinforced concrete Structures*", Vietnam Standard, Hanoi, Vietnam, 2018.

Research Article

Mechanical Properties and Shrinkage of Ultrahigh-Performance Concrete Containing Lithium Carbonate and Nano-Calcium Carbonate

Tingyu Wang,[1] Jianqing Gong [iD],[2] Bo Chen,[1] Xiao Gong,[1] Wanli Guo,[2] Yang Zhang,[2] and Falei Li[2]

[1]*Hunan Provincial Expressway Group Limited Company, Changsha, Hunan 410000, China*
[2]*College of Civil Engineering, Hunan University, Changsha, Hunan 410082, China*

Correspondence should be addressed to Jianqing Gong; gongjianqing@hnu.edu.cn

Early strength generation is essential for the successful application and usage of Ultrahigh-Performance Concrete (UHPC) in reinforcing concrete structures. The work contained in this paper focused on evaluating the effects of lithium carbonate (Li_2CO_3, denoted as LC) and nano-calcium carbonate (NC) on the early mechanical properties and autogenous shrinkage of UHPC under normal temperature curing conditions. In the study, scanning electron microscope (SEM) was utilized to investigate and quantify the morphology of the early hydration products. The corresponding results indicated that the 1-day comprehensive strength of the UHPC increased significantly with the addition of Li2CO3 and NC. Likewise, the addition of NC mitigated the loss of the 28-day compressive strength. For the materials evaluated, the 1-day compressive and flexural strengths reached peak values of 72.1 and 13.9 MPa, respectively, for optimum dosages of 0.075%~0.1% Li_2CO_3 and 3%~4% NC, respectively. The results also indicated that the combined LC-NC dosage had profound effects on the early autogenous shrinkage of UHPC, which could, however, be minimized by adjusting the Li_2CO_3 and NC dosages. That is, the combined dosage of the two early strength enhancers shortens the hydration induction period of cement whilst concurrently accelerating the hydration rate of the cement. The early strength agent increases the number of crystals in the hydration product and the crystal grain size becomes larger. These make the microstructure of the slurry more compact after hardening and therefore improve the overall performance of UHPC.

1. Introduction

Ultrahigh-Performance Concrete (UHPC) is a type of concrete with superior performance compared to ordinary concrete and high-performance concrete [1, 2]. It has ultrahigh strength, toughness [3, 4], and excellent durability. The water-binder ratio is typically less than 0.25 [5]. The compressive strength of UHPC is usually more than 120 MPa [6].

UHPC is widely used due to its excellent mechanical properties, durability, and overall performance. For instance, it can greatly reduce the weight of bridges and improve durability in bridge engineering [7, 8]. It can also be used in restoration projects, such as repairing bridge deck defects [9, 10], repairing bridge piers [11, 12], repairing anticollision layers [13], dams [14], and repairing tunnels [15, 16]. Nonetheless, whilst the early strength develops slowly under normal temperature curing conditions, UHPC needs a high-temperature curing condition to obtain ultrahigh performance and high early strength. This does not only increase the construction challenges and cost but also hinder the wider application of UHPC to a certain extent, especially for engineering applications with high requirements for early strength, such as road and bridge repairs. In this study, lithium carbonate (Li_2CO_3, simply denoted as LC in this paper) and nano-calcium carbonate (NC) were used as early strength enhancers to generate the high early strength of UHPC under normal temperature curing conditions.

Li_2CO_3 is a colorless monoclinic crystal or white powder, which is a type of an inorganic compound. It has been widely used in the battery industry as well as a coagulant in cement admixture. Li_2CO_3 can improve the early strength of concrete. In general, the early strength enhancement derived from Li_2CO_3 is more significant than NC; that is, there is more early strength gain with Li_2CO_3 usage than NC. The incorporation of an appropriate amount of a setting accelerator in concrete can significantly shorten the setting time of concrete. With these accelerators, the concrete can reach the initial setting (or curing) within 5 min and the final setting within 10 min. A certain degree of strength can be produced within one hour, and the strength can be increased to about twice the value after 1 day [17].

LC nanometer is a nanometer-sized type of an ultrafine material. Many scholars have explored the application and usage of these nanomaterials in UHPC. During UHPC production, nanomaterials can accelerate the hydration of cement, densify the microstructure, improve the strength, and improve the overall durability of UHPC. Therefore, nanomaterials can potentially be used as a new type of early strength enhancer. In their study, Sharma et al. found that nano-SiO_2 (NS) particles can accelerate the early hydration rate of cement and promote the formation of single-sulfur type hydrated calcium sulphoaluminate phase in the hydration products [18]. Compared to NS, NC needs a greater amount of mixing to achieve the same effects. Huang et al. found that NC promoted the compressive strength of UHPC more significantly at an optimal mixing amount of 3%–4% [19]. The crystal core effects of NC were found to be the main reason for the increase in the concrete strength [20–22].

In this study, new nanoinorganic early strength enhancers, namely, NC and Li_2CO_3, were selected for laboratory experimentation to enhance the mechanical properties and shrinkage-resistance performance of UHPC. Under warm curing conditions, the variation in the mechanical properties of UHPC at the early stages (1–28 days) and its influence on UHPC autogenous shrinkage were studied using both single and combined dosage of the two early strength enhancers, namely, NC and LC. With the aid of the scanning electron microscope (SEM), the microstructure of the hydration products and the hardened slurry was observed and analyzed to quantify the hydration and strength mechanisms.

2. Laboratory Experimentation

The materials used in the study including the mix designs and sample preparation are presented and discussed in this section. The laboratory tests including strength, shrinkage, and morphological evaluation are also discussed in this section.

2.1. Materials Used.
The cement used in this study was the P.O. 52.5 ordinary Portland cement. Its main chemical components are listed in Table 1. Grade I fly ash was used and its main chemical components are listed in Table 2. The slag powder used was S95-grade slag powder with a specific

TABLE 1: P.O. 52.5 ordinary Portland cement chemical composition.

Chemical composition	Fe$_2$O$_3$%	Al$_2$O$_3$%	SO$_3$%	CaO%	SiO$_2$%	MgO%
Content	4.51	5.76	2.02	64.5	0.23	1.4

surface area of $422\,m^2/kg$. Its main components and technical indicators are shown in Table 3 and 4, respectively.

The particle size of quartz sand was 0.45~0.9 mm (20~40 mesh) and the mass fraction of SiO_2 was more than 99%. The silica fume was gray-white, with an average particle size of 89 nm and a specific surface area of $1.85 \times 104\,m^2/kg$. The water-reducing agent was sourced from a Construction Material Limited Company in Suzhou (China), with a water-reducing rate of more than 30%. Li_2CO_3 (LC) was a white powder with a density of $2.11\,g/cm^3$ and a purity of over 99.5%. The average particle size of NC was 60 nm whilst the mass fraction of $CaCO3_3$ was more than 99%.

2.2. UHPC Mix Design.
The water-binder (W/B) ratio for the mix design was 0.18 in this study. According to the preexperiment results, the content of silica fume, fly ash, and mineral powder was 20%, 5%, and 5% of the cement quality, respectively. The sand-binder ratio was 1.1 and the water-reducing agent content was 1.0%. The specific mix design is shown in Table 5.

2.3. Specimen Preparation and Curing Conditions.
The materials required for the test were weighed according to the mix designs in Table 4 and poured into the mortar mixer. The materials were dry mixed for 2 minutes and then stirred continuously. The weighed water was then added and stirred at a slow speed for 5 minutes. After stirring was complete, the materials were stirred quickly for another 5 minutes. The mixed UHPC was first tested for fluidity and thereafter molded for strength, shrinkage, and microstructure testing. After placing the UHPC mix in the steel mold, it was then placed in an indoor temperature of $20 \pm 2°C$ and covered with plastic films for curing 28 days. At a minimum, three replicate specimens were prepared per material per mix design per test type per test condition.

2.4. Laboratory Testing.
The methods for testing the compressive and flexural strengths are discussed in the subsequent. The UHPC compressive strength and flexural strength were tested according to the Test Method for Cement Mortar Strength GB/T17671-1999 [23]. For the flexural strength test, the standard size of the specimen is $40\,mm \times 40\,mm \times 160\,mm$. First, the appearance and measurement of the specimen were checked. The specimen was then loaded continuously and uniformly at the speed of 0.08 MPa/s until failure, from which the failure load was captured and recorded. The compressive strength test was immediately carried out with the fractured cement mortar test block after the flexural test. The compressive fixture with a compression area of $40\,mm \times 40\,mm$ was used for which the load was applied uniformly at a rate of $2.4\,kN/s \pm 0.2\,kN/$

TABLE 2: Chemical composition of fly ash.

Chemical composition	SiO_2 (%)	Al_2O_3 (%)	Fe_2O_3 (%)	CaO (%)	SO_3 (%)	MgO (%)	Loss (%)
Content	52.52	31.62	9.35	4.57	1.21	0.73	3.86

TABLE 3: Chemical composition of slag powder.

Chemical composition	SiO_2 (%)	Al_2O_3 (%)	Fe_2O_3 (%)	CaO (%)	SO_3 (%)	MgO (%)	Loss (%)
Content	78.64	5.01	0.28	7.00	1.21	3.4	4.41

TABLE 4: Technical indicators of slag powder.

Variety specification	Density (g/cm^3)	Specific surface area (m^2/kg)	Liquidity ratio (%)	7 d activity (%)	28 d activity (%)
S95	2.92	422	99	77	95

TABLE 5: Basic mix design of high early strength UHPC.

Group	W/B	Cement	Silica fume	Fly ash	Mineral fines	Quartz sand	Water-reducing agent (%)	Li_2CO_3	NC
A1/B1/C0	0.18	1	0.20	0.05	0.05	1.1	1	0%	0%
A2	0.18	1	0.20	0.05	0.05	1.1	1	0.075%	0%
A3	0.18	1	0.20	0.05	0.05	1.1	1	0.1%	0%
A4	0.18	1	0.20	0.05	0.05	1.1	1	0.125%	0%
B2	0.18	1	0.20	0.05	0.05	1.1	1	0%	2%
B3	0.18	1	0.20	0.05	0.05	1.1	1	0%	3%
B4	0.18	1	0.20	0.05	0.05	1.1	1	0%	4%
B5	0.18	1	0.20	0.05	0.05	1.1	1	0%	5%
C1	0.18	1	0.20	0.05	0.05	1.1	1	0.075%	2%
C2	0.18	1	0.20	0.05	0.05	1.1	1	0.075%	3%
C3	0.18	1	0.20	0.05	0.05	1.1	1	0.075%	4%
C4	0.18	1	0.20	0.05	0.05	1.1	1	0.075%	5%
C5	0.18	1	0.20	0.05	0.05	1.1	1	0.1%	2%
C6	0.18	1	0.20	0.05	0.05	1.1	1	0.1%	3%
C7	0.18	1	0.20	0.05	0.05	1.1	1	0.1%	4%
C8	0.18	1	0.20	0.05	0.05	1.1	1	0.1%	5%
C9	0.18	1	0.20	0.05	0.05	1.1	1	0.125%	2%
C10	0.18	1	0.20	0.05	0.05	1.1	1	0.125%	3%
C11	0.18	1	0.20	0.05	0.05	1.1	1	0.125	4
C12	0.18	1	0.20	0.05	0.05	1.1	1	0.125	5

s until the specimen failed. The failure load was then measured and recorded.

The autogenous shrinkage properties were evaluated and tested using the SBT-AS early cement slurry, mortar, and concrete autogenous shrinkage strain tester. The method involved using a standard probe to sense/detect the distance between the probe and bellows clamp. Thereafter, the change in the UHPC volume was converted to the change in distance between the clamps and the probe. The inner/outer diameter of the bellows was 20 mm and 30 mm, respectively, with a length of 340 ± 5 mm. Two test specimens were prepared for each test group, and the average value of the self-contraction value of the two specimens for each group was adopted. The testing range was 0–4 mm, with a resolution of 0.5 m and an accuracy of 0.05%.

For microstructure testing, a JSM-6490LV SEM model was used. That is, the SEM was used to observe the microstructure of cement-based materials when they were hydrated for 1 day, from which the strengthening and toughening mechanisms of the early strength enhancer were characterized and analyzed.

3. Test Results, Analyses, and Synthesis

The test results of the compressive and flexural strength evaluations are presented and discussed in this section. The results also include shrinkage evaluation and microstructure characterizing of the UHPC as a function of LC and NC, respectively.

3.1. Effects of the LC and NC Additives on the UHPC's Mechanical Properties. The UHPC mechanical properties that were measured and evaluated in this study include the compressive and flexural strengths. The results for these mechanical properties, namely, compressive and flexural strength, are presented, analyzed, and synthesized in the texts below.

3.1.1. Compressive Test Results. Figure 1 shows the variational trend of the compressive strength as a function of curing age and LC-NC dosage. At one day (i.e., 1 d) old, the UHPC compressive strength initially increased and then stabilized with an increase in the LC content. When the LC content reached 0.1%, the 1 d compressive strength increased by about 44%. At 3 d, the UHPC compressive strength in Figure 1(a) initially increased and then stabilized with an increase in the LC content, which is almost similar to the 1 d response trend.

When the LC content was 0.1%, the 3 d compressive strength in Figure 1(a) reached a maximum value of 87.4 MPa. At the curing age of 7 days (i.e., 7 d), the compressive strength initially increased and then decreased with an increase in the LC content. Similarly, when the LC content reached 0.1%, the 7 d compressive strength reached a maximum value of 105.3 MPa, with an increasing rate of 9%. When the dosage of LC reached 0.125%, the matrix strength of UHPC generally degenerated for all the curing ages evaluated. At the curing age of 28 days (i.e., 28 d), LC had an adverse effect on the UHPC strength. With an increase in the LC content, the matrix strength generally exhibited a declining response trend.

As shown in Figure 1(b), the UHPC compressive strength at 1 d, 3 d, 7 d, and 28 d, respectively, was dependent on NC when NC was added. Just like LC, an increase in the NC amount yielded an initial increase in the compressive strength followed by a progressive decline, thereafter. In the case of NC, however, Figure 1(b) shows that the maximum compressive strength value occurred at 3% NC. The maximum compressive strength registered at 1 d was 62.4 MPa whilst it was 95.8 MPa at 3 d. When the curing age was 7 d and 28 d, the maximum compressive strengths recorded were 121.8 MPa and 33.7 MPa, respectively. For NC dosages higher than 3%, Figure 1(b) exhibits a downward response trend for the strength evolution.

As a result of NC single mixing, the early strength of UHPC was greatly improved. The 1 d compressive strength of UHPC for 0% NC was 42.9 MPa. After adding 3% NC, the compressive strength of UHPC reached 62.4 MPa in one day, which increased by 45% compared with the control group. This is mainly because nano-CaCO3 can play the role of a microaggregate filler between cement and other mineral powder particles to improve the density of its accumulation and reduce the porosity. Compared with LC, the 28 d compressive strength of UHPC with NC was higher than that of the control group. This is mainly because nano-$CaCO_3$ can play the role of a microaggregate filler between cement and other mineral powder particles to improve the density of its accumulation and reduce the porosity.

Based on the single additive mixing experimentation results, the two enhancers were simultaneously combined into the UHPC matrix to study the combined effects of LC and NC on the UHPC mechanical properties. The content of LC was 0.075%, 0.1%, and 0.125%, respectively, whilst that of NC was 2%, 3%, 4%, and 5%, respectively. The experimental results for the combined LC-NC dosage are shown in Figure 2.

A comparison between Figures 1 and 2 shows that as 0.1% LC and 3% NC were added, the 1 d compressive strength reached its highest peak at 72.1 MPa and thereafter declined progressively. Thus, whilst the single LC dosage significantly improved the early strength, the 28 d strength degenerated significantly and therefore was not conducive for long-term use. Single NC dosage also exhibited potential to improve the early strength, but unlike LC, nano-$CaCO_3$ greatly increased the 28 d strength of UHPC. When the two enhancers (i.e., LC and NC) were simultaneously mixed together, the 1 d compressive strength exceeded 70 MPa, and due to the LC-NC synergistic effects, a decay in the 28 d compressive strength that was noted in Figure 1 was somehow mitigated. That is, the LC-NC-combined additive increased the 1 d strength of UHPC by 68% with no adverse effects on the 28 d compressive strength of UHPC.

3.1.2. Flexural Test Results. The addition of LC and $CaCO_3$ not only affects the UHPC compressive strength but also influences the flexural strength of UHPC. The test results of the UHPC flexural strength when LC and NC were added are shown in Figure 3 as a function of curing age. Figure 3(a) shows that when LC was added as a single dosage, the UHPC flexural strength initially increased and then stabilized after 1 d, 3 d, and 7 d of aging with an increase in the LC dosage. When the LC dosage reached 0.1%, the flexural strength evolution stabilized, with the 1 d flexural strength being about 12.8 MPa. However, the incorporation of LC has an adverse effect on the 28 d flexural strength of UHPC. With an increase in the LC content, the 28 d flexural strength of UHPC decreased progressively. Although LC can greatly improve the mechanical properties of UHPC in the early curing stages, an increase in dosage will degenerate the strength in the later stages of curing.

The effects of NC optimization on the UHPC flexural strength are shown in Figure 3(b). From the figure, it is evident that optimization of NC can significantly enhance the early flexural strength of UHPC. When the curing age was 1 d, the UHPC strength varied as a function of NC dosage. The response trend shows an initial increase in the strength and then slightly degenerates to a maximum value of 12.9 MPa at 3% NC. The flexural strengths of 3 d and 7 d aging reached their maximum values (namely, 20.3 MPa and 22.1 MPa, resp.) at 3% NC content. Compared to the addition of LC in Figure 3(a), the UHPC flexural strength increased significantly with the addition of NC. The 28 d flexural strength of UHPC for 3% NC was 19.2 MPa. At the age of 28 days (i.e., 28 d), the flexural strength of UHPC for 3% NC greatly improved and reached a peak of 24.2 MPa, indicating an increase of 23%.

In the optimization of NC, when the dosage was 1%~6%, the increase in the UHPC flexural strength at 1 d aging was 11%, 21%, 28%, 25%, 21%, and 17%, respectively. From Figure 3(b), the increase in the flexural strength is most apparent at 3% NC, with the peak value also occurring at this dosage. However, the strength evolution slows down as the NC dosage increases above 3% NC. At 3% NC, the strength growth for 3 d UHPC flexural strengths was 23%, 25%, 32%, 29%, 25%, and 21%, respectively. Overall, the strengthening effect of 3 d aging was more apparent, reaching a maximum
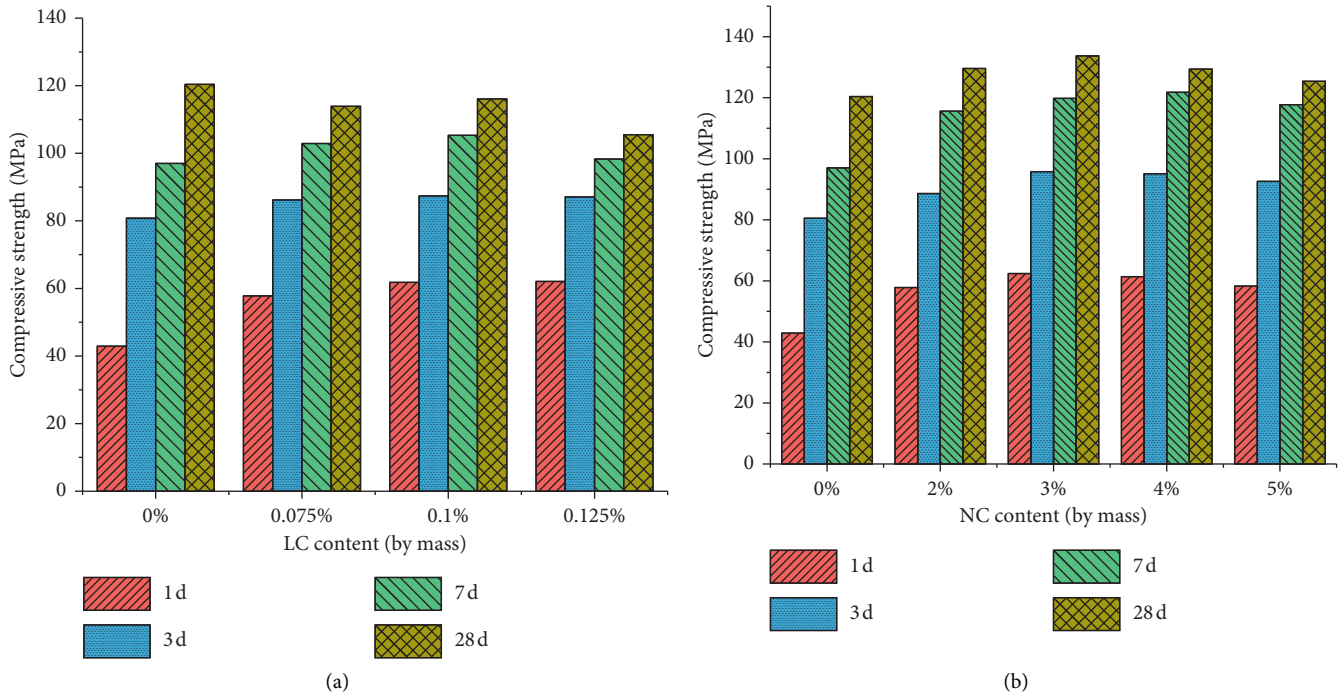
(a)

(b)

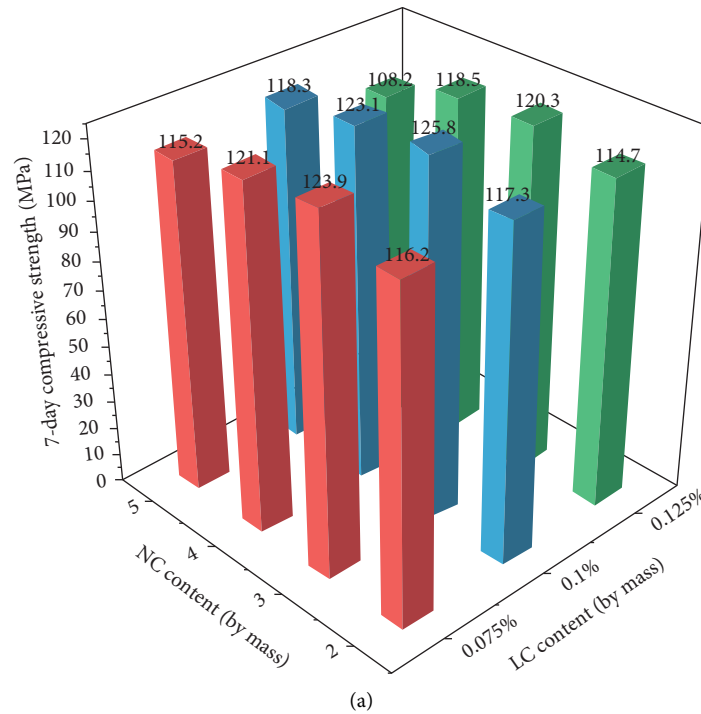Figure 1: Effects of LC and NC single-type dosage on the UHPC comprehensive strength.
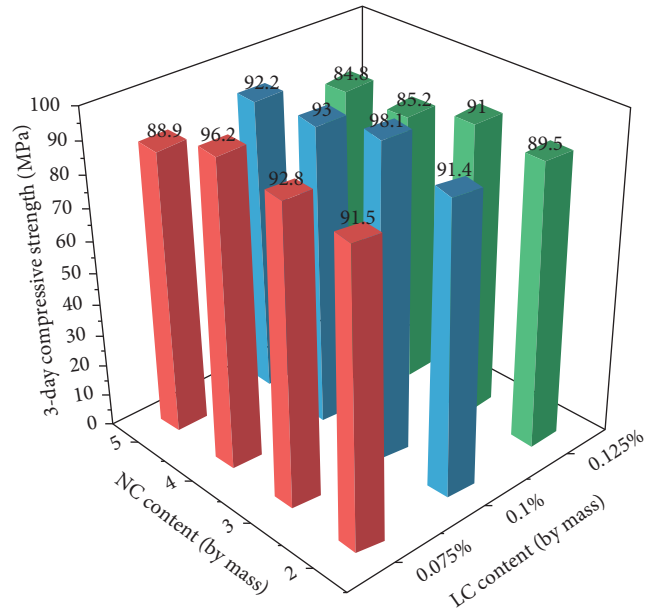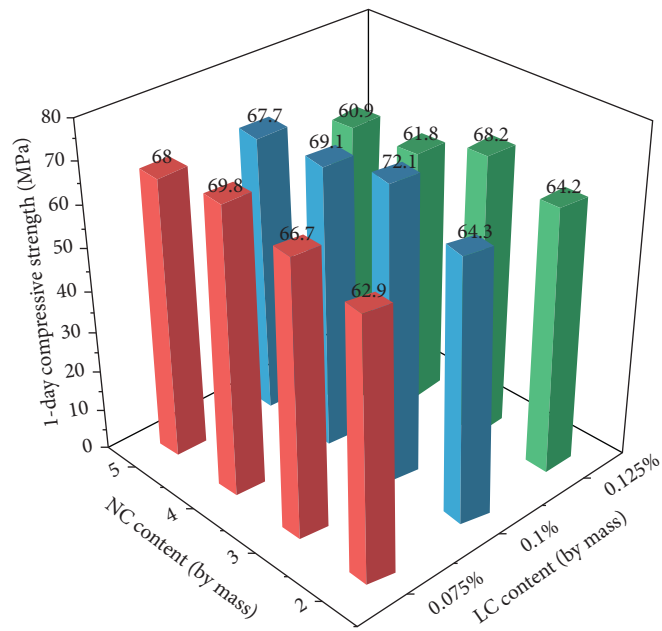

(a)

Figure 2: Continued.

(b)

(c)

Figure 2: Continued.
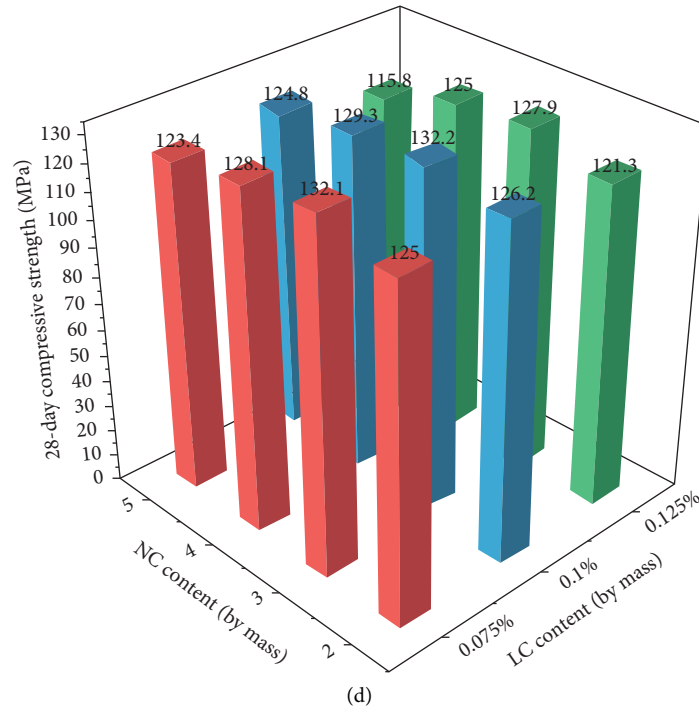
FIGURE 2: Effects of LC-NC combined additives on the UHPC compressive strength.
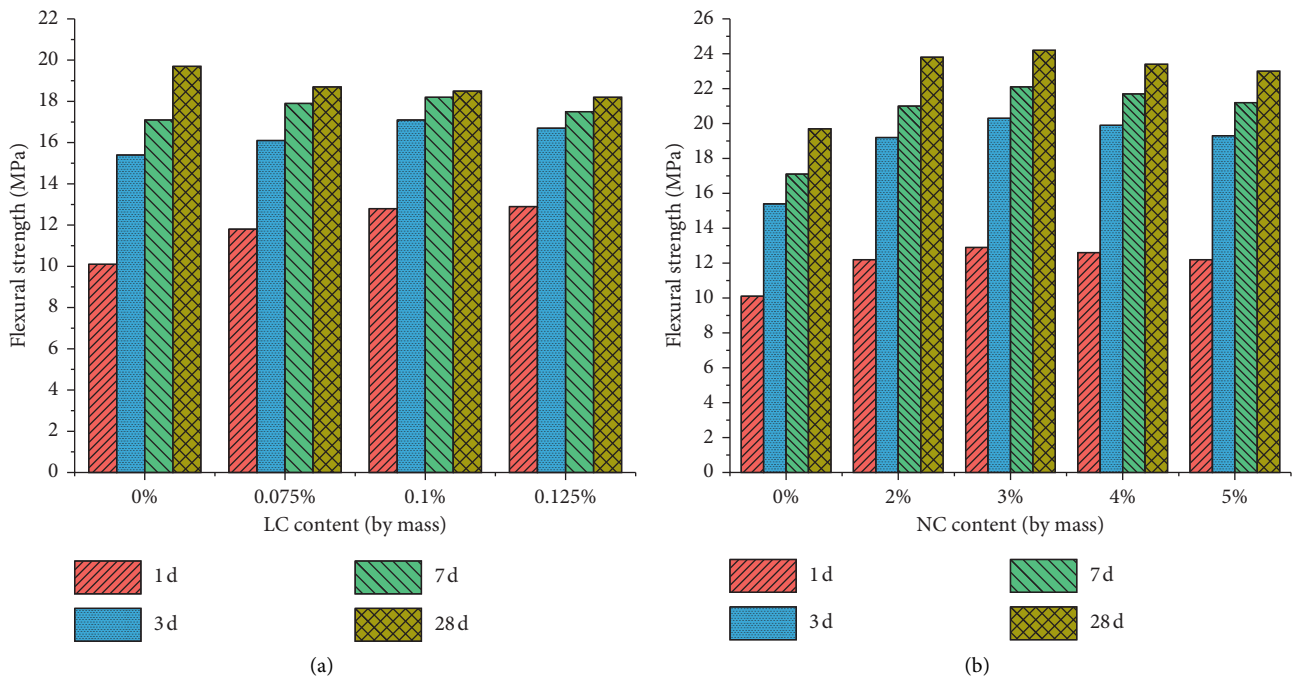
FIGURE 3: Effects of LC and NC single-type dosage on the UHPC flexural strength.

growth rate of 32% for 3% NC. For 7 d, the corresponding growth rates were 20%, 23%, 29%, 27%, 24%, and 18%, respectively, with 29% being the highest increment. These increments are hardly different for 1 d and 3 d aging for 3% nano-$CaCO_3$ dosage. From these results, it is evident that

NC has a significant enhancement effect on the early strength generation of UHPC and that the strength enhancement was most apparent for 3% NC dosage. However, a continuous increase in the NC content will significantly reduce the UHPC fluidity and decrease the strength

evolution. Therefore, 3% is recommended as the optimum NC dosage. Figure 4 shows the combined effects of LC-NC dosage on the UHPC flexural strength.

From Figure 4, it is apparent that the 1 d flexural strength was highest at 13.9 MPa for 0.1% LC and 3% NC, respectively. When comparing with Figure 3, it is evident that the single dosage of LC can significantly improve the early strength of UHPC but greatly degenerated the 28 d flexural strength. Similarly, single doped NC also significantly improved the early UHPC flexural strength. At 28 d aging, however, the UHPC flexural strength could potentially be increased by about 10%~24%. When the two LC-NC enhancers are mixed together, the UHPC flexural strength at 1 d and 28 d aging could potentially be increased by up to 38% and 24%, respectively.

3.2. Effects of the LC and NC Additives on UHPC's Autogenous Shrinkage.

Figure 5 shows the influence of LC on UHPC self-contraction under different dosages, namely, 0.075%, 0.1%, and 0.125%, respectively. It can be seen from Figure 5 that the shrinkage of the group with added LC is larger than the specimens without LC. The experimental data show that the shrinkage rate of the specimens without LC was $1147 \, mm^{-1}$ and $1332 \, mm^{-1}$ for 0.075% LC, respectively, which is 16% higher than the reference group, that is, control specimens without LC. From the figure, the self-shrinking of UHPC with 0.1% LC was found to be $1738 \, mm^{-1}$, which is about 52% higher than that of the control specimens (or reference group). For 0.125% LC, the shrinkage was 1917 mm, an increase of about 67% over the control specimens, that is, the reference group. In comparison to specimens containing LC, the contraction growth rate (slope of the response curve) of the NC modified specimens at the early stage of curing was relatively small. This behavioral response trend may be caused by LC promoting the formation of some AFt crystals whilst ettringite has an expansive effect and partially compensates for the contraction effect. After the formation of the concrete matrix, the contraction tends to be stable.

The damage of the hydration protective film on the surface of the cement particles was accelerated due to Li^+ having a small ionic radius and strong polarization effects. Additionally, the hydration induction period of cement was greatly shortened whilst the mineral component C was expanded. However, the continuous hydration of cement is considered the root cause of autogenous shrinkage. The hydration rate, degree of hydration degree, and the hydration water content of the cement minerals are some of the key factors that potentially affect autogenous shrinkage.

The effect of hydration products on the shrinkage of concrete is generally different depending on the hydration products. The hydration process of C_3A requires a large amount of water. It gives off a lot of heat. Therefore, the hydration reaction of C_3A has the greatest influence on the autogenous shrinkage of concrete. The incorporation of LC greatly promotes the hydration rate of cement due to the high content of sulfur in Portland cement.

Figure 6 shows the effects of nano-$CaCO_3$ with different NC dosages on the autogenous shrinkage performance of UHPC. In general, an excessive amount of mixing significantly impacts the UHPC fluidity, which could potentially make the slurry be very thick and difficult to be stirred/blended. For ease of use and constructability considerations, three different NC dosages, namely, 2%, 3%, and 4%, respectively, were selected to evaluate the autogenous shrinkage of UHPC; see Figure 6.

From the test results in Figure 6, the following conclusions were derived. The mix ratio can potentially show an early UHPC microexpansion effect mainly because of the cement condition and other mineral admixtures after being fully mixed with water. Calcium silicate and the active mineral admixture in the cement composition react quickly with water, thus releasing a large amount of hydration heat, with a slight swelling effect at the beginning of the reaction.

In Figure 6, the B1 group did not contain NC whilst B2, B3, and B4 had 2%, 3%, and 4% nano-$CaCO_3$, respectively. The addition of NC shows distinctive initial microexpansion effects in the cement matrix. By observing the trends and changes in the response curve, it can be seen that the shrinkage of UHPC increased significantly before 10 h, that is, 10 hours. The slope of the curve is very steep, indicating that, during this time, lots of hydration reactions took place within the UHPC, which ultimately generates a large number of hydration products whilst consuming a large amount of water. This in turn results in the continuous decrease of the overall volume with a large contraction. It can be seen from Figure 6 that, during the early stages of NC being added, the slope of the self-contraction response curve of $CaCO_3$ was larger than that of the control group without NC. This indicates that the incorporation of nano-$CaCO_3$ can accelerate the hydration reaction rate of cementitious materials and promote the secondary hydration reaction of cement and to some extent other active mineral components as well. This not only significantly improves the early strength evolution but also produces large shrinkage.

As the hydration reaction progresses, the internal "self-drying" effect becomes apparent because the water glue of UHPC is relatively low. Additionally, the hydration reaction consumes a large amount of free water, particularly nano-$CaCO_3$. At about 72 hours, the shrinkage of the control group without the enhancers (i.e., B1) was smaller than that of the group with the enhancers. The experimental data showed that no nano-$CaCO_3$ was added to B1. The shrinkage of the specimens with 2% NC was $1147 \, mm^{-1}$, which was self-shrinking to $1858 \, mm^{-1}$ and translating to about 62% higher than the reference or control group, that is, B1. The self-shrinking rate of 3% NC was $1938 \, m \cdot m^{-1}$ and represented about 69% higher than the reference group. The autogenous shrinkage of 4% NC is $1779 \, mm^{-1}$, an increase of 55% over the reference or control group, namely, B1.

From the above analysis, it can be seen that the incorporation of NC greatly improved the self-contraction of UHPC. When the cement is hydrated, a large amount of water is consumed, causing the pored liquid level to drop. This forms the minuscule surface and ultimately results in the so-called self-drying effect. As a result, the internal volume of the whole cement slurry decreases. The early strength of concrete develops rapidly and causes the early

(a)

(b)

FIGURE 4: Continued.

(c)

(d)

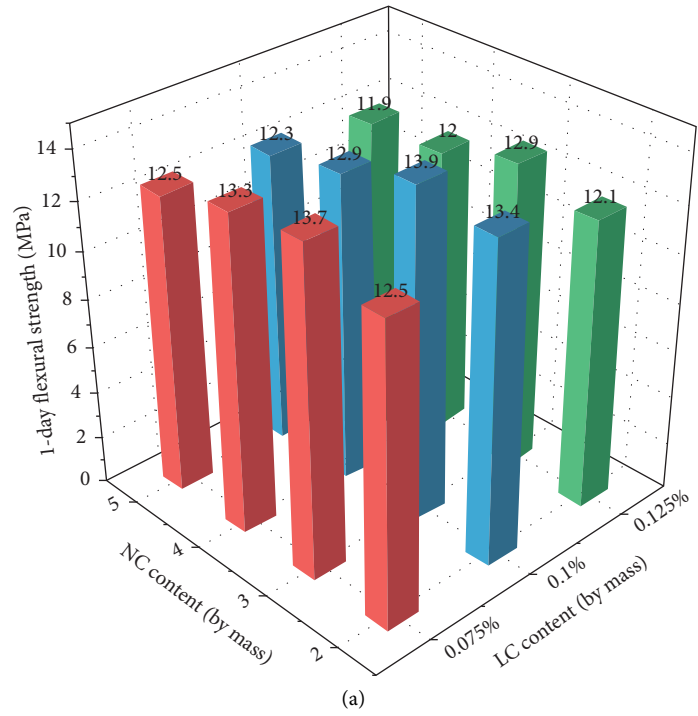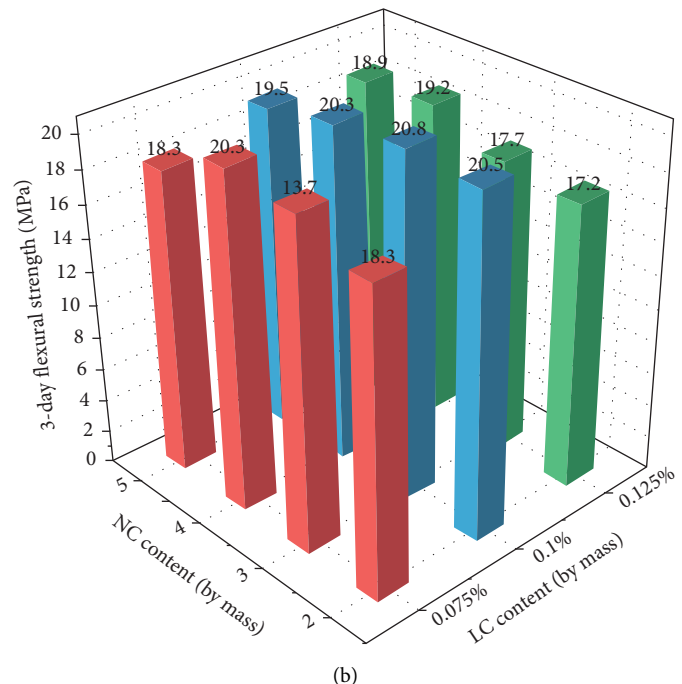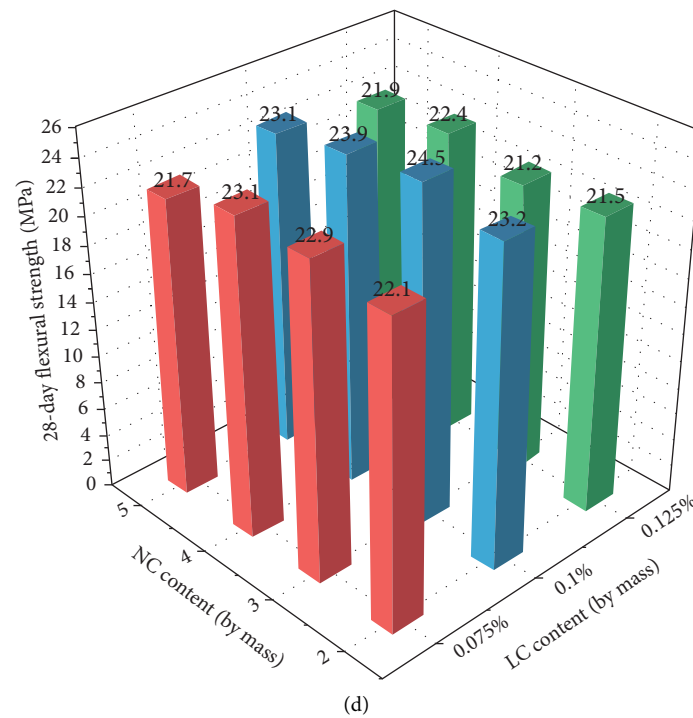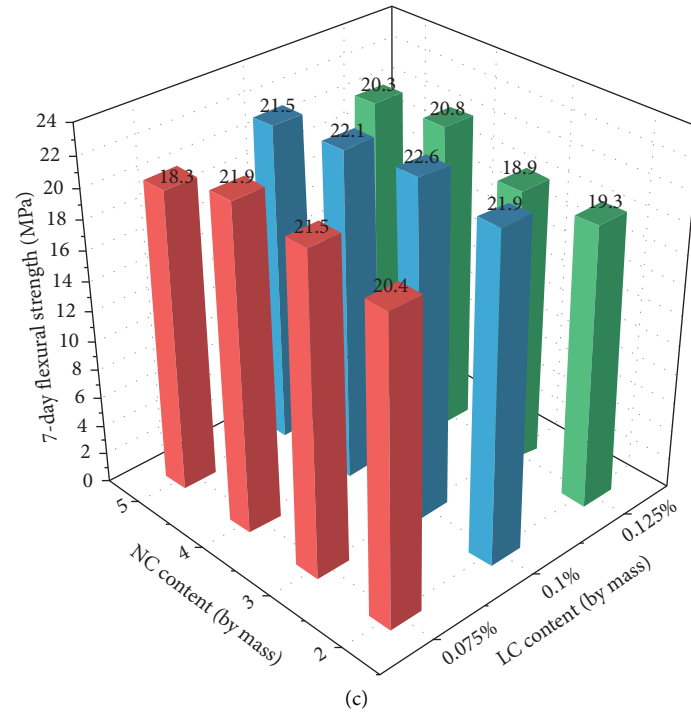Figure 4: UHPC flexural strength with LC-NC combined dosage.

formation of the concrete skeleton due to the early strength effects of NC. Therefore, as time goes by, the formation of hydration products has little impact on the macroscopic volume change of concrete. As can be seen from Figure 6, the curve gradually flattens out with no significant increase. In addition, the shrinkage was relatively smaller for the 4% dosage (i.e., B4), which may be due to the filling of many

nanometer particles partially compensating for some shrinkage. On the other hand, with an increase in the NC dosage, the water absorption would correspondingly increase, thus slowing down the hydration reaction rate to some extent.

The design mix groups were C5, C6, and C7, respectively. The LC content was maintained constant at 0.1% whilst that

FIGURE 5: Effects of LC on the autogenous shrinkage of UHPC ($A1 = 0\%$ LC; $A2 = 0.075\%$ LC; $A3 = 0.1\%$ LC; $A4 = 0.125\%$ LC; h = hour).

FIGURE 6: Effects of NC on the autogenous shrinkage of UHPC ($B1 = 0\%$ NC; $B2 = 2\%$ NC; $B3 = 3\%$ NC; $B4 = 4\%$ NC; h = hour).
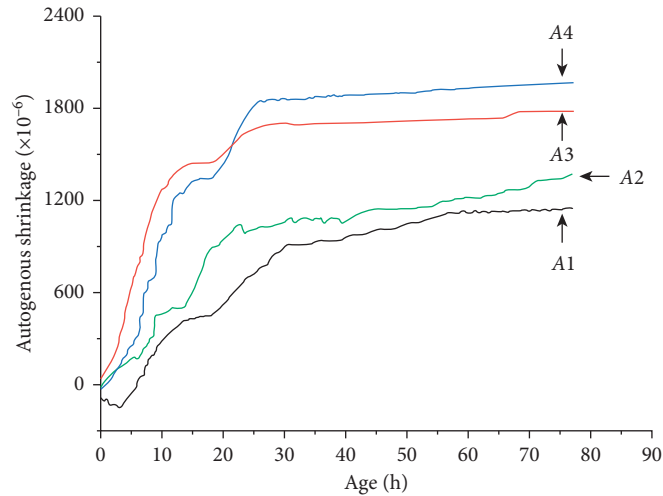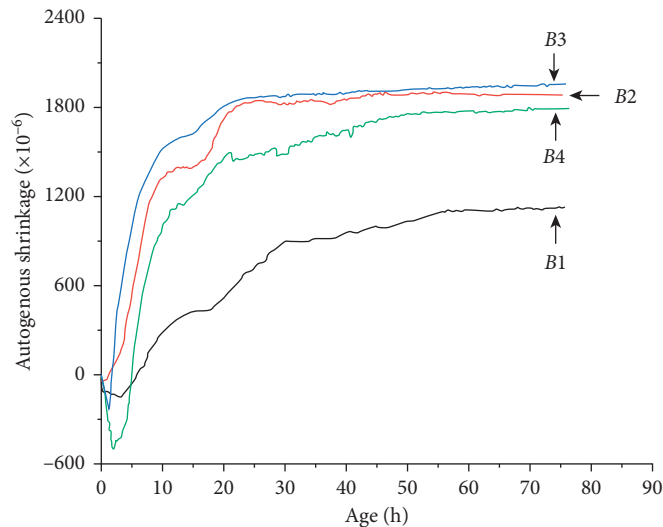
of NC was selected as 2%, 3%, and 4%, respectively. The results of the combined LC-NC dosage on the early self-contraction of UHPC are shown in Figure 7.

As shown in Figure 7, under the action of a combined LC-NC dosage, the autogenous shrinkage of UHPC at 72 h increased significantly in comparison to the single-type dosage. The experimental data indicated that when 0.1% LC and 2% NC were added, the autogenous shrinkage of UHPC at 72 h increased significantly. The shrinkage value at 72 h was 2291 mm^{-1}, which was 100% higher than the shrinkage value of the reference group, that is, $C1$. For 0.1% LC and 3% NC, the shrinkage value at 72 h was 3100 mm^{-1}, which was 170% higher than the contraction value of the reference group, namely, $C1$. At 0.1% LC and 4% NC dosages, the shrinkage value at 72 h was 2897 mm^{-1}, representing 153% higher than the contraction value of the reference group, namely, $C1$. Form these results, it is obvious that the combined incorporation of LC and NC significantly improved the early strength of UHPC and accelerated the hydration rate of UHPC in the early curing stages, thus greatly increasing the early autogenous shrinkage of UHPC. Therefore, the method to reduce the autogenous shrinkage of UHPC under the normal temperature curing conditions remains a problem warranting future exploration and research investigations.

3.3. Effects of the LC and NC Additives on the Microstructure of UHPC.

In this laboratory experimentation, the microstructure and morphology of UHPC with and without the LC-NC additives were observed under vacuum conditions using the SEM. For SEM characterization, the $A0$ (without additives) and $C6$ (fastest early strength growth) specimens at 1 d aging were selected for microstructural analysis. Figure 8 shows the $A0$ (without LC-NC additives) micromorphological results for 1 d specimens cured with film mulching at room temperature.
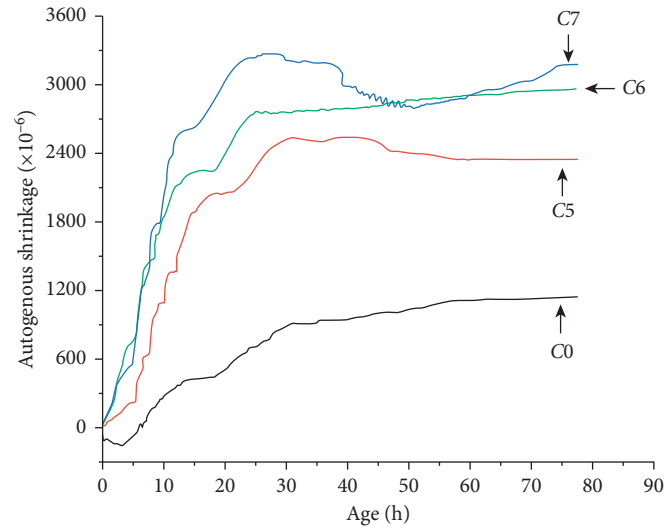
FIGURE 7: Effects of LC and NC combined additives on the autogenous shrinkage of UHPC ($C0 = 0\%$ LC and 0% NC; $C5 = 0.1\%$ LC and 2% NC; $C6 = 0.1\%$ LC and 3% NC; $C7 = 0.1\%$ LC and 4% NC; h = hour).

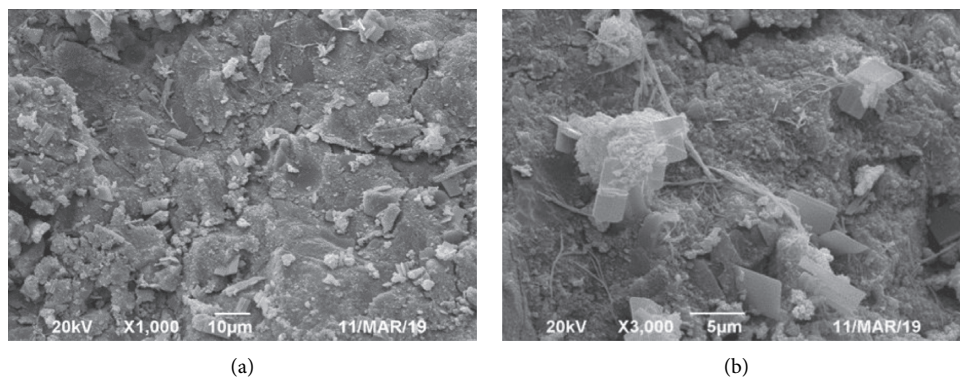(a)   (b)

FIGURE 8: Microstructure of UHPC without LC-NC additives.

It can be seen from Figure 8 that, due to the relatively low degree of hydration in the early stages of curing, some fine pores appear in the concrete matrix. Under normal temperature curing conditions, part of the hydration reaction occurs within the UHPC matrix. However, as can be seen from Figure 8, there are still numerous unhydrated particles within the UHPC matrix, causing its early strength to be relatively low. From Figure 8(b), although it is only 1 d, the internal hydration products are unevenly distributed. From the figure, it can also be seen that the quantities of Ca $(OH)_2$ crystals and C–S–H gel are relatively small.

Figure 9 shows the addition of LC and NC_3 on the micromorphology of the 1 d specimen cured with film mulching at room temperature. As can be seen in Figure 9, the combined incorporation of LC and NC sped up the rate of cement hydration. The hydration products of the reference group ($A0$) are more apparent, with the crystals significantly increasing in terms of both numerical counts and grain sizewise. Also, a large number of AFt crystals and C–S–H became close together and resulted in a more compact structure. This greatly enhances the mechanical

properties of UHPC as Li + with a smaller ionic radius induces a strong polarization effect and accelerates the hydration of cement particles to generate a surface protective film. This in turn greatly shortened the cement hydration induction period and expanded the mineral composition of C_3S/C_2 as well as the area of contact between sulfur and water-ultimately raising the C_3S/C_2 content and the hydration rate of S. On the other hand, due to the $CaCO_3$ nucleation effects when S starts to hydrate, Ca^{2+}, with a strong migration ability, is released. Based on the adsorption theory and coion effect, when Ca^{2+} is diffused in NC_3, the particle surface will be adsorbed and create C_3Ca around the S particles, thus reducing the concentration and ultimately promoting the C generation and to some extent the hydration of S.

By comparing Figures 8 and 9, it can be observed that when LC-NC is added, the structure of UHPC is more compact and is mainly attributed to nano-$CaCO_3$. The microaggregate effect of NC is that the average particle size of UHPC is about 60 nm, which can be filled in the particle gap between cement, fly ash, ore powder, and silica fume.
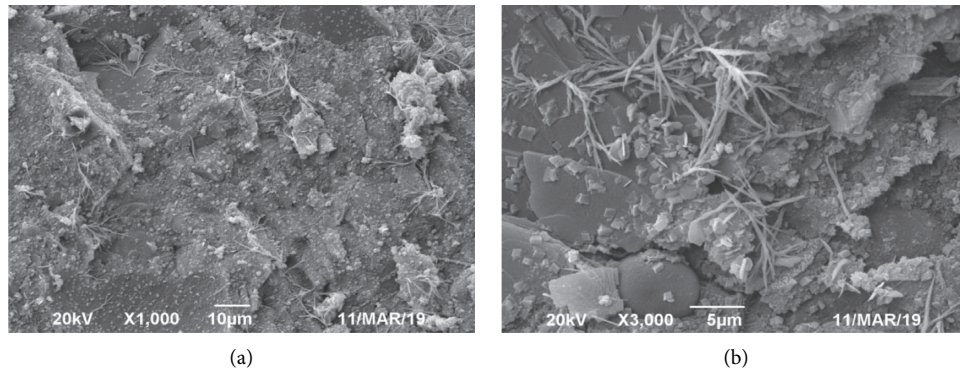
(a)   (b)

Figure 9: Microstructure of UHPC with LC-NC additives 2.

This filling effect results in compacting the structure of UHPC and reducing its internal defects, thus improving the early mechanical properties of UHPC. On the other hand, some NC gets embedded in the cement slurry, due to the "pinning" effect of NC. The existence of NC restricts the development of cracks, thus playing a role in improving the overall toughness of the UHPC matrix.

3.4. Effects of LC-NC Additives on the Strength Enhancement Mechanism of UHPC.

As can be seen from the previous test results, LC and NC were cured at room temperature. In general, the early mechanical properties of UHPC greatly improved with the addition of LC and NC, respectively. As discussed below, the mechanism of action and strength enhancement include microaggregate effects and synergistic hydration.

3.4.1. Microaggregate Effects.

The particle size of nanomaterials is on the scale of nanometer (1–100 nm). Its characteristic properties include the following: (1) the particle size is smaller than the usual powder but larger than the atomic cluster, and (2) the particle size is small but with a large specific surface area. For NC, the average particle size of $CaCO_3$ is about $60 \, nm_3$, and as a nanoscale material, it has a small size and surface effects. After it is added to the UHPC colloidal particles, the pores are initially filled to improve the pore structure with an increase in the accumulation density of the powder [24, 25]. In traditional UHPC, silica dust is usually the smallest particle and can improve the particle gradation of UHPC. For nano-$CaCO_3$, the addition of wollastonite further fills the pores inside and between the silica ash and other particles, which further increases the density of the cementing system [26, 27]. Nano-$CaCO_3$ can also produce a pinning effect on the interface of the cement particles, which not only prevents further expansion of the internal crack of cement particles to some extent but also improves the early compressive strength evolution of UHPC.

3.4.2. Synergistic Hydration.

Portland cement clinker contains a large amount of C. The content of the S mineral can reach up to 60% and its hydration reaction rate is high. The nature of hardened cement slurry is largely determined by C and the hydration of S. Firstly, lithium ions are characterized by their small radius and strong polarization. Comparatively speaking, lithium ions are more likely to pass through and/or enter the hydration film, which accelerates the destruction of the hydration protection film on the surface of the cement particles [28] and also expands the mineral component C_3S/C_2. Additionally, the contact area between S and water promotes the flow of calcium ions into the film to the outside of the film and breaks through the hydration film due to the coion effects. This promotes cement hydration, shortens the cement induction period, and accelerates the hydration reaction to improve the C in the cement. The hydration ability of S under normal temperature curing conditions generates more hydration products at the early stages, thus improving the early mechanical properties of UHPC.

3.5. Effects of the LC-NC Additives on the Shrinkage Mechanism of UHPC.

In the hydration process of concrete, a large amount of water will be consumed, resulting in a decrease of the wool stoma liquid level that is often called the "self-drying" effect [29], and causes the occurrence of menisci in the wool stoma of concrete. The strong hydration promotes the rapid advance of the capillary lemnisci in concrete, with the hardened cement particles being subjected to negative pressure. As the hydration reaction takes place, the humidity inside the concrete is reduced because the reaction process consumes a large amount of moisture, which ultimately reduces the critical radius r whilst the capillary suction ΔP (Pv-Pc) increases. Negative pressure acts on the tube wall around the capillary tube to produce compressive stress. When the relative humidity decreases to a lower level, the stress caused by the negative pressure of the capillary tube increases rapidly. This causes the cement particles to contract and induce self-contraction (shrinkage) of the whole concrete matrix.

The continuous hydration of cement is technically viewed as the root cause of autogenous shrinkage. Tazawa proposed an empirical formula to predict the autogenous shrinkage of cement slurry after its hydration for 1 d based on the experimental regression of the mineral composition of ordinary Portland cement as follows [30]:

$$\sum(t) = 0.012 \, alpha_{C3S} \, (t)PC3S \, 0.070 \, alpha._{C2S} \, (t)PC2S + 2.256 \, alpha._{C3A} \, (t)PC3A + 0.085 \, alpha._{C4AF} \, (t)PC4AF \qquad (1)$$

According to equation (1), the mineral composition of the cement clinker can affect the shrinkage of concrete. The fastest hydration rate is C_3A and has the greatest influence and its combined water content is also the highest. This is followed by C_4AF and C_3S with C_2S having the least impact. Based on the previous test results, the addition of LC and NC accelerated the early hydration rate of UHPC, thereby greatly improving its early strength evolution. The greater the degree of hydration (i.e., the more the hydration products), the greater the capillary pressure, ultimately resulting in the UHPC undergoing self-contraction.

4. Conclusions and Recommendations

This study was conducted to evaluate the effects of Li_2CO_3, denoted as LC, and NC on the early mechanical properties and autogenous shrinkage of UHPC under normal temperature curing conditions. The materials used comprised of P.O. 52.5 ordinary Portland cement, grade I fly ash, and S95-grade slag powder whilst the additives were LC and NC, respectively. In the study, SEM was utilized to investigate and quantify the morphology of the early hydration products of the UHPC. From the study results and findings, the following conclusions and recommendations were drawn:

(i) The results indicated that the 1 d comprehensive strength of UHPC increased significantly with the combined LC-NC dosage with NC effects being instrumental in mitigating the 28 d comprehensive strength loss. The 1 d comprehensive and flexural strengths reached peak values of 72.1 MPa and 13.9 MPa, respectively. Compared with the reference specimens, the 1 d comprehensive and flexural strength of the modified UHPC had strength gains of about 68% and 38%, respectively. Based on the study findings, the recommended optimum dosages are 0.075%~0.1% LC and 3%~4% NC, respectively.

(ii) For single-type dosage, both LC and NC can potentially increase the early self-contraction of UHPC, with 3% NC being the optimum additive content. With the LC-NC additives, the self-contraction ratio of UHPC was increased by 69% over the reference group. The autogenous shrinkage corresponding to 0.125% LC was 67% higher than that of the reference group without any LC-NC additives.

(iii) Under the combined action of LC-NC dosage, the early self-contraction of UHPC greatly increased due partially to the "superposition" effects of the LC-NC additives. Compared with the reference group, the increase in UHPC self-contraction after the combined dosage of the LC-NC additives ranged from 100% to 170%, which is significantly larger than the UHPC self-contraction when only one additive is used.

(iv) Under the combined action of LC-NC dosage and for 1 d curing time, the following were observed: (1) the hydration rate of the cement was accelerated; (2) the hydration products were more apparent in the reference group; (3) the number of crystals was significantly increased and coalesced into larger grain sizes; and (4) a large number of AFt crystals became closely packed with C–S–H. This resulted in the matrix structure being very compact and thus greatly improved the early mechanical properties of UHPC.

(v) The experimental test results showed that LC-NC can be used as early strength enhancers to produce high early strength UHPC under normal temperature curing conditions, with no adverse effects on the 28 d strength of UHPC. This ultimately substantiates the potential applicability of using LC and NC additives to enhance the early strength evolution and overall performance of UHPC.

Overall, this study has successfully quantified the effects of LC-NC additives on the mechanical properties and autogenous shrinkage of UHPC under normal temperature curing conditions, with the recommended optimum dosages being 0.075%~0.1% LC and 3%~4% NC, respectively. Whilst the study results were plausible, exploration of new methods for further reducing shrinkage along with the need for correlation and validation with field performance data is warranted in future studies. Nonetheless, the study beneficially contributes to enriching the literature through the provision of a reference datum for quantifying the modification and enhancement effects of LC-NC additives on UHPC.

Data Availability

The data used to support the findings of this study are available from the corresponding author upon request.

Disclosure

The content of this paper, which is neither a standard nor a design/bidding document, reflects the views of the authors who are solely responsible for the facts and accuracy of the data presented herein and does not necessarily reflect the official views or policies of any institution. Trade names were used solely for information purposes and not for product endorsement, advertisement, or certification.

Conflicts of Interest

The authors declare that they have no conflicts of interest.

Acknowledgments

References

[1] S. He, J. Qiu, J. Li, and E.-H. Yang, "Strain hardening ultra-high performance concrete (SHUHPC) incorporating CNF-coated polyethylene fibers," *Cement and Concrete Research*, vol. 98, pp. 50–60, 2017.

[2] Y. Su, C. Wu, J. Li, Z.-X. Li, and W. Li, "Development of novel ultra-high performance concrete: from material to structure," *Construction and Building Materials*, vol. 135, pp. 517–528, 2017.

[3] S. Abbas, A. M. Soliman, and M. L. Nehdi, "Exploring mechanical and durability properties of ultra-high performance concrete incorporating various steel fiber lengths and dosages," *Construction and Building Materials*, vol. 75, pp. 429–441, 2015.

[4] W. Chong, C. Yang, L. Fang et al., "Preparation of ultra-high performance concrete with common technology and materials," *Cement & Concrete Composites*, vol. 26, no. 8, pp. 538–544, 2004.

[5] S. T. Kang, J. I. Choi, K. T. Koh et al., "Hybrid Effects of Steel fiber and microfiber on the tensile behavior of ultra-high-performance Concrete," *Composite Structures*, vol. 145, pp. 3–42, 2016.

[6] K. Wille, A. E. Naaman, S. El-Tawil, and G. J. Parra-Montesinos, "Ultra-high performance concrete and fiber reinforced concrete: achieving strength and ductility without heat curing," *Materials and Structures*, vol. 45, no. 3, pp. 309–324, 2012.

[7] P. Y. Blais and M. Couture, "Precast, prestressed pedestrian bridge—world's first reactive powder concrete structure," *Pci Journal*, vol. 44, no. 5, 1999.

[8] M. Behloul and K. C. Lee, "Ductal seonyu footbridge," *Structural Concrete*, vol. 4, no. 4, pp. 195–201, 2003.

[9] E. Denarie and E. Bruhwiler, "Structural rehabilitation with ultra high performance fibre reinforced concretes," *Restoration of buildings and monuments=Bauinstandsetzen und Baudenkmalpflege*, vol. 12, no. 5, pp. 453–467, 2006.

[10] E. Denarié, *SAMARIS D22-Full Scale Application of UHPFRC for the Rehabilitation of Bridges–From the Lab to the Field*, Samaris, Brussels, Belgium, 2005.

[11] M. Bastien Masse and E. Brühwiler, "Concrete bridge deck slabs strengthened with UHPFRC," in *Proceedings of the IABSE Conference Rotterdam 2013 "Assessment, Upgrading and Refurbishment of Infrastructures"*, vol. 99, Rotterdam, Netherlands, May 2013.

[12] M. A. Sakr, A. A. Sleemah, T. M. Khalifa, and W. N. Mansour, "Shear strengthening of reinforced concrete beams using prefabricated ultra-high performance fiber reinforced concrete plates: experimental and numerical investigation," *Structural Concrete*, vol. 20, no. 3, pp. 1137–1153, 2019.

[13] O. Cornelius, E. Denarié, and E. Brühwiler, "UHPFRC protection layer on the crash barrier walls of a bridge," *Advances in Construction Materials*, vol. 3, pp. 203–210, 2007.

[14] E. Brühwiler and E. Denarié, "Rehabilitation and strengthening of concrete structures using ultra-high performance fibre reinforced concrete," *Structural Engineering International*, vol. 23, no. 4, pp. 450–457, 2013.

[15] T. Ono, "Application of ultra-high-strength fiber-reinforced concrete for irrigation channel repair works," in *Designing And Building With UHPFRC*Wiley, Hoboken, NJ, USA, 2011.

[16] L. Guingot, D. Dekhil, and P. Soulier, "Strengthening of hydraulic structures with UHPC," in *Proceedings of the RILEM-Fib-AFGC International Symposium on Ultra-high Performance Fibre-Reinforced Concrete*, pp. 137–146, Marseille, France, January 2013.

[17] Z. Huang, J. Fan, and X. Xie, "Research on the high performance and low-density aerated concrete," *Materials Review*, vol. 12, pp. 136–140, 2013.

[18] U. Sharma, L. P. Singh, B. Zhan, and C. S. Poon, "Effect of particle size of nanosilica on microstructure of C-S-H and its impact on mechanical strength," *Cement and Concrete Composites*, vol. 97, pp. 312–321, 2019.

[19] W. Li, Z. Huang, F. Cao, Z. Sun, and S. P. Shah, "Effects of nano-silica and nano-limestone on flowability and mechanical properties of ultra-high-performance concrete matrix," *Construction and Building Materials*, vol. 95, pp. 366–374, 2015.

[20] J. Camiletti, A. M. Soliman, and M. L. Nehdi, "Effects of nano- and micro-limestone addition on early-age properties of ultra-high-performance concrete," *Materials and Structures*, vol. 46, no. 6, pp. 881–898, 2013.

[21] L. R. Gurney, D. P. Bentz, T. Sato, and W. J. Weiss, "Reducing set retardation in high-volume fly ash mixtures with the use of limestone," *Transportation Research Record: Journal of the Transportation Research Board*, vol. 2290, no. 1, pp. 139–146, 2012.

[22] T. Sato and J. J. Beaudoin, "The effect of nano-sized $CaCo_3$ addition on the hydration of opc containing high volumes of ground granulated blast-furnace slag," in *Proceedings of theb2nd International RILEM Symposium on Advances in Concrete through Science and Engineering*, Quebec City, Canada, September 2006.

[23] GB/T17671-1999, *Test Method for Strength of Cement Mortar (IOS)*, Standards Press of China, Beijing, China, 1999.

[24] Z. Huang and F. Cao, "Effects of nano-materials on the performance of UHPC," *Materials Review*, vol. 18, pp. 136–141, 2012.

[25] Z. Huang and T. Zu, "Influence of nano-CaCO3 on ultra high-performance concrete," *Bulletin of the Chinese Ceramic Society*, vol. 6, pp. 1103–1109, 2013.

[26] E. Kassem, L. Walubita, T. Scullion, E. Masad, and A. Wimsatt, "Evaluation of full-depth asphalt pavement construction using X-ray computed tomography and ground penetrating radar," *Journal of Performance of Constructed Facilities*, vol. 22, no. 6, pp. 408–416, 2008.

[27] L. F. Walubita, B. Jamison, A. E. Alvarez et al., "Air void characterisation of HMA gyratory laboratory-moulded samples and field cores using X-ray computed tomography (X-ray CT)," *Journal of the South African Institution of Civil Engineering*, vol. 54, no. 1, pp. 22–30, 2012.

[28] L. Xiao and H. Zhang, "Influence of new composite early strength agent on mechanical properties of concrete (mortar) and its mechanism analysis," *Bulletin of the Chinese Ceramic Society*, vol. 37, no. 7, pp. 2115–2119, 2018.

[29] B. Persson, "Self-desiccation and its importance in concrete technology," *Materials and Structures*, vol. 30, no. 5, pp. 293–305, 1997.

[30] E.-I. Tazawa and S. Miyazawa, "Influence of cement and admixture on autogenous shrinkage of cement paste," *Cement and Concrete Research*, vol. 25, no. 2, pp. 281–287, 1995.